Università degli Studi di Torino

PhD School of Natural Sciences and Innovative Technologies

Department of Molecular Biotechnology and Health Sciences

Ph.D. Program in Pharmaceutical and Biomolecular Sciences

Cycle: **XXX**

Thesis Title:

Novel MRI/Optical imaging agents for targeted diagnosis and treatment of diseases

Candidate:

Amerigo Pagoto

Tutors:

Prof. Enzo Terreno
Prof. Silvio Aime

PhD Program Coordinator:

Prof. Gianmario Martra

Academical Years: **2014-2017**

Università degli Studi di Torino

PhD School of Natural Sciences and Innovative Technologies

Ph.D. Program in Pharmaceutical and Biomolecular Sciences (XXX Cycle)

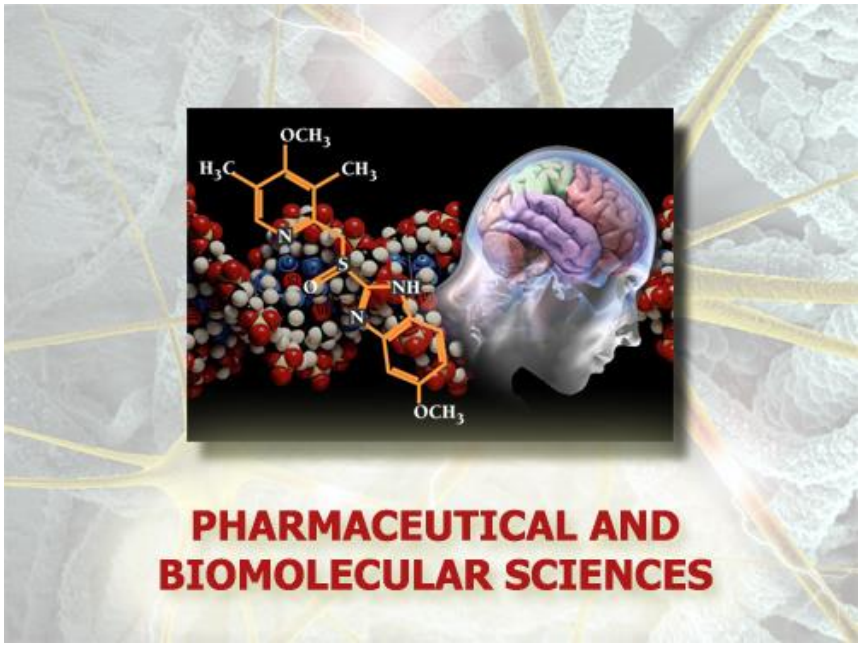

Novel MRI/Optical imaging agents for targeted diagnosis and treatment of diseases

Candidate: **Amerigo Pagoto**

Tutors: **Prof. Enzo Terreno**
Prof. Silvio Aime

A Mamma e Papá che mi hanno dato la vita
ed a tutte le persone che mi permettono di continuare a viverla

"*These creatures you call mice, you see, they are not quite as they appear. They are merely the protrusion into our dimension of vast hyperintelligent pandimensional beings. The whole business with the cheese and the squeaking is just a front."*
The old man paused, and with a sympathetic frown continued.
"They've been experimenting on you, I'm afraid."

Douglas Adams (The Hitchhiker's Guide to the Galaxy)

Contents

Chapter 1

General Introduction

1 - Targeted Imaging Agents

Since its dawn, at the beginning of XXI century, Molecular Imaging (MI) is a research field focusing on the non-invasive visualization of biological processes in living beings (**1**). From the first applications in nuclear medicine, across the years, there has been a boost to find new molecules, generically called imaging agents, able to detect in real-time biochemical processes occurring at molecular/cellular level in living tissues (**2**). Focusing on nuclear medicine, the PET tracer [^{18}F]FDG (FluoDeoxyGlucose) is certainly one of the first and most successful agent developed in this field (**3**). This particular molecule is internalized and , after phosphorylation by hexokinase II (**4**), trapped inside cells with high glucose consumption, *i.e.* with high metabolic activity (**5-8**). Since the molecule is a glucose analog, it is specific for the glucose transporters (*e.g.* GLUT-1) (**2**,**9-11**), which are also overexpressed on the surface of many tumor cells (**12-15**). Therefore, [^{18}F]FDG is the most representative example of a probe able to visualize metabolism *in vivo*. [^{18}F]FDG finely represents the general concept of a molecular imaging agent, containing a specific receptor-interacting moiety (FDG) and a signaling component (^{18}F) . The chemical features of the latter are dependent on the imaging technique of interest: CT (Computed Tomography), MRI (Magnetic Resonance Imaging), PET (Positron Emission Tomography), SPECT (Single Photon Computed Tomography), OI (Optical Imaging), US (ultrasound), and PAI (Photoacoustic Imaging) represent the mostly diffuse imaging technologies currently available. Each of them have peculiar features such as spatial resolution, penetration depth and detection sensitivity, which should be taken in account for the design of the imaging agent (**16**). Typically, an imaging probe for MI applications is composed by a portion generating the imaging signal (signaling component) linked, by a proper spacer, to a vector for the specific recognition of the biological target (targeting vector) (Figure 1): of course, this a general scheme. For example, in PET tracers, like [^{18}F]FDG, the signaling component is often a single atom (the radioisotope) and therefore the signaling component and the targeting vector are not represented by two distinct chemical moieties.

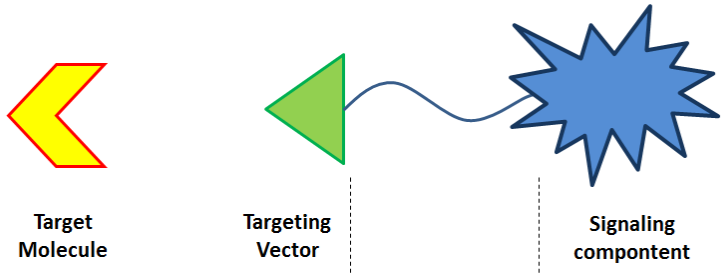

Figure 1. Schematic representation of a targeted imaging agent for MI applications.

The word target, probably derived from Old French "targe" that means "light shield", was linked to the archery just in the mid XIII: the targeting molecule is designed, like an arrow, to reach (and interact with) the target. The targeting molecules may also be called vectors, and they were proposed in different forms in the last decades, from small molecules (as peptides and antibody fragments) to macromolecules (as aptamers or monoclonal antibodies) (**17**). In this PhD thesis, my interest was mainly focused on the development of imaging agent vectorized by peptides. In the next paragraphs, the use of peptides as targeting vectors for imaging purposes will be discussed in detail.

1.1 Peptide-based Imaging Agents

A peptide is simply defined as a small sequence (generally less than 50) (**18**) of amino acids. Peptides are important in many biological processes, acting like signaling molecules (*e.g.* Glucagon) (**19**) or as antioxidant agents (*e.g.* Glutathione) (**20**). The ribosomal peptides are generically synthesized by translations of the mRNA (messenger Ribonucleotide Acid) at the endoplasmic reticulum level (**18**) or in the cytoplasm, with elongation that occurs from N- to C-terminals. The peptide biosynthesis often generates small hormones that are implicated in key biological processes such as glucose metabolism (*e.g.* Insulin) (**21**) or central nervous system responses (*e.g.* Somatostatine)(**22**).

In 1963, R.B. Merrifield (**23**) published the first paper that proposed a complete solid phase chemical synthesis of peptides, and his outstanding contribution in this field was awarded with the Nobel prize in 1984. This work paved the way to the development of a controlled synthetic strategy for the generation of small molecules: this type of process was optimized bringing to the current SPPS (Solid Phase Peptide Synthesis). The basic principles of SPPS follow few simple steps, which are mainly illustrated in Figure 2. First of all, the C-terminal amino acid of the growing sequence is anchored on a solid support. The side chains of each aminoacid are normally "chemically blocked'' by groups that are normally not affected during the peptide elongation, thus allowing a linear (C- to N-terminals) synthesis. Conversely, the α-amino group is protected by labile protecting group, which is removed after the de-protection step. The following amino acid, added in high molar excess, is then coupled to the growing sequence by using coupling agents that led to the formation of the first amide bond. These steps are repeated until the formation of the peptide is completed. Finally, the product is removed from the solid support in highly acidic conditions, with consequent release of the side-chain protecting groups. As mentioned before, in this way it is possible to synthetize a complete peptide sequence from C to N-terminal, i.e. with the opposite direction with respect to the natural synthetic process.

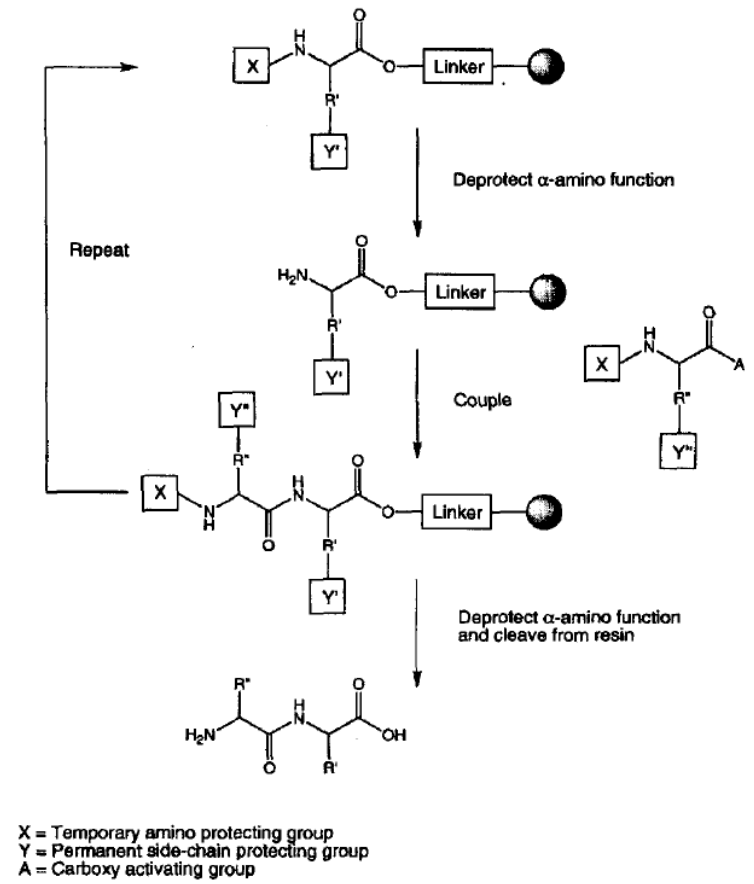

Figure 2. Scheme of Solid Phase Peptide Synthesis. (**24**)

This optimized synthesis showed enormous advantages in comparison with solution phase procedures: firstly, each step allows the formation of an intermediate product linked to the solid support that can easily be separated by the soluble reagents just by washing steps and filtration. This makes possible the use of a large excess of reagents, which accelerates the reaction kinetics and improve the reaction yield. Moreover, since the procedure is characterized by repetitive steps, all the process is highly prone to automation, and several automated peptide synthesizers are nowadays commercially available on the market. Moreover, SPPS methodology is particularly suitable for the the bioconjugation of the peptides to the signaling component of the MI probe.

However, it is necessary to remark the limitations of this approach: the more relevant is the formation of byproducts, given by incomplete or side reactions, which reduces the purity and yield of the final product (**24**). Nevertheless, by properly coupling the synthetic strategy with further purification steps (*e.g.* liquid chromatography), it is feasible to obtain fine pure products.

This method is highly compatible with the techniques that are currently used for the identification of new highly specific peptidic sequences for a given target. For instance, phage display methodology, which exploits libraries containing high amount ($10^7 – 10^9$) of different phage clones, allows the screening of billion sequences for a specific target in a fast and controlled way (**25**). The

most specific sequence could be then selected, amplified, characterized and finally sequenced, to obtain the targeting moiety.

In molecular imaging the size matters: though the applications of macromolecular vectors for imaging diseases detections are countless, the use of small peptides to guide the targeting has shown peculiar advantages such as an high vascular permeability, tissue uptake, and fast clearance (**26,27**). However, it has to be considered that the targeting peptides need to be conjugated to the signaling component of the probe, thus potentially limiting the advantages of using small-sized peptides.

Peptides are particularly suitable for designing imaging tracers for the highly sensitive (picomolar range) nuclear imaging techniques (PET and SPECT). So far, one of the most commonly used targeting peptides in MI experiments is RGD (Arg-Gly-Asp), a tripeptide developed to bind a specific class of integrin receptors. Integrin receptors are expressed on cells to facilitate the cell-extracellular matrix interaction (**28**), but some of them (*e.g.* $\alpha_v\beta_3$) are strongly associated with activated endothelial cells during tumor angiogenesis and metastasis (**29**). Several radionuclides were directly linked to this targeting vector for diagnostic use, for example ^{18}F-galacto-RGD, investigated for the detection of different malignancies like melanoma, breast or head and neck tumors (**30,31**). Recently, RGD-based tracers with different nuclides were tested on esophagus tumors (^{68}Ga-NODAGA-RGD) (**32**) or to detect bone metastasis (^{99m}Tc-3P-RGD) (**33**). Another class of targeting peptides widely studied for nuclear medicine application are the Somatostatine (SST) analogs. They physiologically act as small cyclopeptidic hormones, but their receptors were found associated with different tumors like neuroendocrine tumors or small cells lung cancer (**34**). In 1994, the ^{111}In-DTPA-octreotide (OctreoScan), based on somatostatine analogs, was the first peptide-based tracer approved by FDA for scintigraphy of neuroendocrine tumors. Subsequently, also ^{99m}Tc (^{99m}Tc-Octreotide) (**35**) and ^{68}Ga based (^{68}Ga-DOTATOC) (**36**) tracers were developed for PET imaging of neuroendocrine tumors.

Other sensitive imaging techniques, such as optical imaging, have seen a huge spread of peptide based-imaging probes. The targeting moiety, in a way similar to the ^{68}Ga, ^{111}In ot ^{99m}Tc radiolabeling design, is attached directly to a sensitive fluorophore for optical detection. Although during the years thousands of fluorescent molecules were developed for imaging purposes, the spread of Near Infrared Dyes, discussed in the following paragraphs, has recently represented a breakthrough for the application. In addition to “conventional” SST- (**37,38**) or RGD-based (**39,40,41**) fluorescent peptides, other “activatable” peptide-based optical probes have been reported. These dyes are designed to be activated after the cleavage operated by specific enzymes present at the biological

target. A typical approach is based on FRET (Fluorescence Resonance Energy Transfer) mechanisms, in which the fluorescence of a dye (called acceptor) is quenched by another dye (called donor) located in close proximity (typically within 10 nm) (**42**). If the two dyes are spatially separated following an enzymatic cleavage, the fluorescence of the acceptor switches on, thus allowing the optical visualization of the enzymatic activity. This approach has been successfully applied for detecting the *in vivo* activity of MMPs (Matrix Metallo Proteinases). This is a family of zinc-dependent endopeptidases that play key roles in several biological processes and are biomarkers of many diseases from cancer to inflammation (**43**).

However, one of the most interesting applications of optical imaging agents are in the field of Image-Guided Surgery (IGS), where the depth limitations of this imaging technology are not an issue, and their high detection sensitivity is fully exploited to offer a valuable support to surgeons during interventions. This point will be further discussed in paragraph 3.

When compared with nuclear and optical imaging modalities, Magnetic Resonance Imaging (MRI) suffers of a much lower sensitivity (3-5 order of magnitude) in the contrast detection generated by exogenous agents, and this is an important issue to be faced for the design of MRI-based MI protocols.

The contrast detection sensitivity can be improved using several strategies, among which the increase in the number of the contrastophores (*e.g.* Gd(III) or Mn(II) ions in paramagnetic T_1 agents) delivered at the biological target is likely the most used.

Though some mono-nuclear Gd(III)-based targeting agents have been reported (**45,46**), MI-MRI probes with an increased number of paramagnetic centers are very common. Following this way, it has been possible to synthesize small molecular weight multimers (**47,48,49**), or link the targeting peptide on the surface of a nanosystem, where the signaling component is not directly linked to the peptide (**50,51,52**).

In the next paragraph the basic mechanisms for contrast generation and properties of the signaling components for MRI and Near InfraRed Fluorescence (NIRF) imaging, the two imaging techniques considered in this PhD project will be introduced.

2 - Magnetic Resonance Imaging basics

MRI is an imaging technique based on NMR (Nuclear Magnetic Resonance) principles and clinically used for non-invasive diagnostic purposes. The first pioneering research in the field was mainly associated with the work carried out by Lauterbur and Mansfield (**53**), both awarded by the Nobel prize in 2003. At the beginning of 70', the first body *in vivo* ^{1}H images from water and fatty acids were reported (**54**). The hydrogen atoms, like others having odd numbers of protons/neutrons (*e.g.* ^{13}C, ^{19}F, ^{31}P), are characterized by magnetic spin moment values different from 0. This quantum mechanics property allows them, when subjected to a static external magnetic field (B_0), to experience a particular rotational motion called precession, with a rotational frequency corresponding to their proton Larmor frequency. This phenomenon brings to the formation of a net magnetic vector (called magnetization) along to the B_0 direction (generically referred as the z-axis). It is possible, applying to the system an external electromagnetic (radio) waves with the same frequency of the proton precession, to change the orientation of the net magnetic vector, which is re-oriented from its equilibrium to a less stable condition (the plane x-y). When the radiowave is switched off, the initial equilibrium is restored following a process called relaxation (Figure 3) (**55**). The NMR signal is detected on the x-y plane and, following the Fourier transformation, it allows to discriminate the spins as a function of their resonance frequency. The translation from a typical NMR proton spectrum to a proton MR image is quite complex mechanism and it requires the application of specific magnetic gradients along the sample, in order to spatiallly localize the spins on the basis of their resonance frequency. Since the MRI signal weighted on spin density is not particularly informative due to the similarity in tissue water content, the signal is typically weighted on longitudinal (T_1) or transverse (T_2/T_2*) relaxation times, as it will be discussed in the next paragraph.

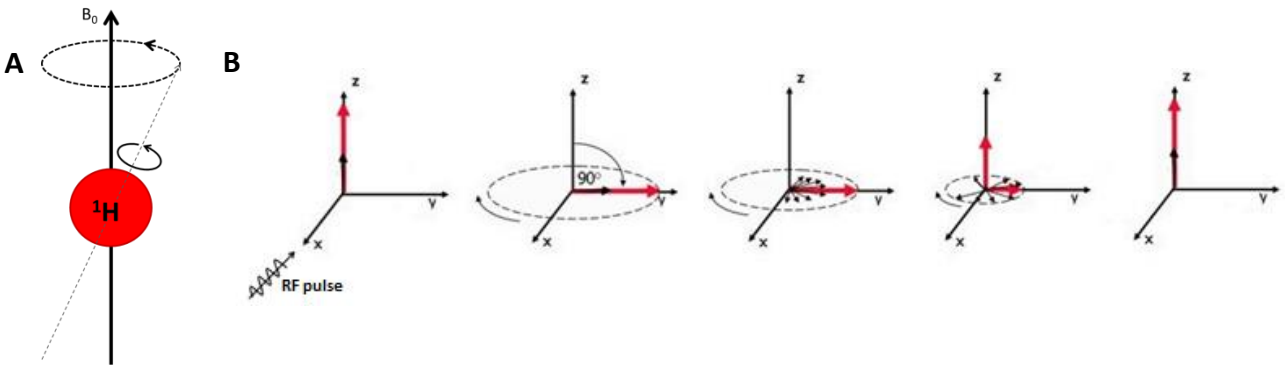

Figure 3. Schematic representation of magnetization formation and destiny after application of external radiofrequency. In the figure A it is possible to observed the typical proton precession, in the presence of external magnetic field (B_0), which contributes to the formation of the net magnetic vector. Figure B represent the evolution of the magnetization after the application of Radiofrequency

2.1 Longitudinal and Transverse Relaxation times

Longitudinal (T_1) and Transverse (T_2/T_2*) relaxation times represent two important components for the generation of MR images. These values are described as the time decay constant involved in the return of the net magnetization along z- and y-axis, respectively, after the application of the perturbing external radio frequency (**55**). The two parameters are generally described by the exponential functions reported in Figure 4.

A $M_z = M_0[1 - 2e^{(-\frac{t}{T1})}]$

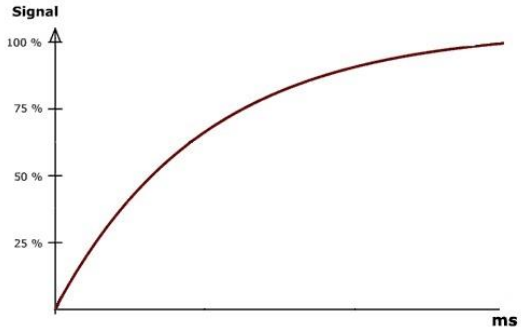

Longitudinal Magnetization Recovery (T1)

B $M_{xy} = M_0 e^{(-\frac{t}{T2})}$

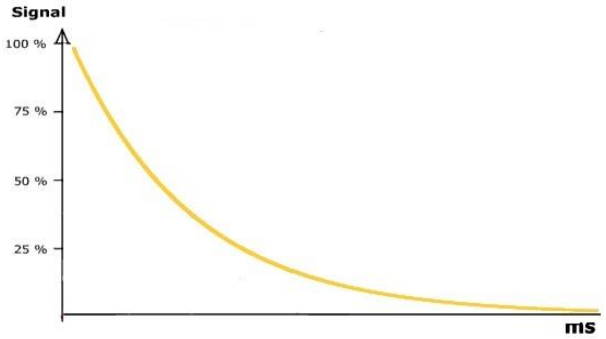

Transverse Magnetization Decay (T2)

Figure 4. Mathematical definition and graph representation of the Longitudinal Magnetization Recovery (A) and Transverse Magnetization Decay (B). After the application of the the RF, different phisical phenomena allow the formation (recovery) of the magnetizazion in the equilibrium condition, with conseguent loss (decay) of the vector from the less stable condition (plane x-y)

The human tissues normally show water protons T_1/T_2 dissimilarities, which are the main source of the MRI contrast. This structural endougenous differences can be emphasized, either by designing specific acquisition pulse sequences or with the administration of exogenous contrast agents. During this PhD project, research has been focused on the latter type of contrast modulation.

Two different types of contrast agents have been developed entered in the clinic: T_1 agents, which mainly act shortening the longitudinal relaxation rate, and the T_2 agents, which shorten the transverse relaxivity (**56**).

T_2/T_2* agents, also called superparamagnetic or negative contrast agents, are mostly represented by iron oxide particles (SPIO), containing the metal in different forms (*e.g.* Fe_3O_4 or Fe_2O_3). The Fe atoms in the particles induce a local magnetic field inhomogenity with a conseguent decrease of the transverse relaxation time. This phenomenon brings to a signal loss (negative contrast) in the tissues where the agent distributed (**57**).

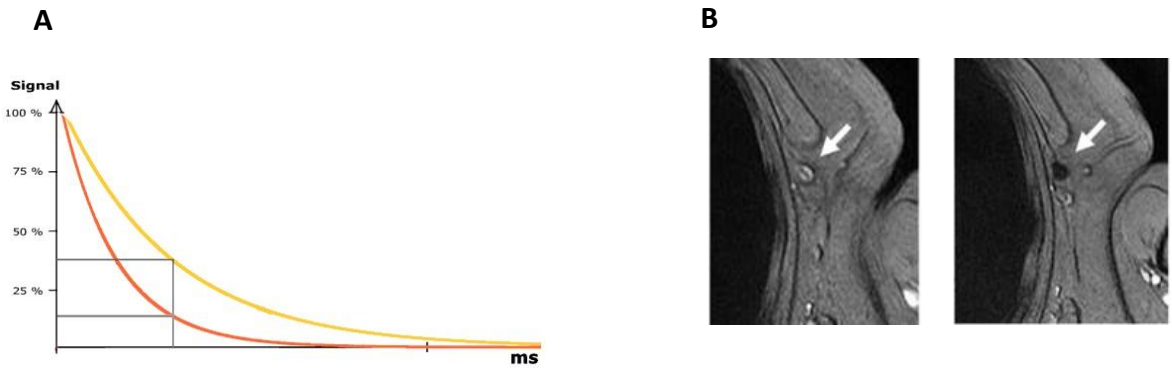

Figure 5. Decrease of the MRI signal induced after the injection of T_2 contrast agent (A). The images (B) demostrate the effect of the effect of SPIO in the detection of lymphnode on T2w axial MRI images (**58**)

T_1 agents, also known as paramagnetic or positive contrast agents, are mostly represented by compounds based on gadolinium(III) or manganese(II) ions. Due to the presence of unpaired electrons in the external orbital of the metal ions, it is possible to induce, in presence of a magnetic field, the formation of a magnetic dipole. This characteristic allows the dipole-dipole interaction with the surrounding protons (mainly belonging to water molecules), bringing to a shortening of the longitudial relaxation time (**59**). This phenomenon is responsible to the generation of a positive contrast in T_1-weighted (T_{1W}) MR image.

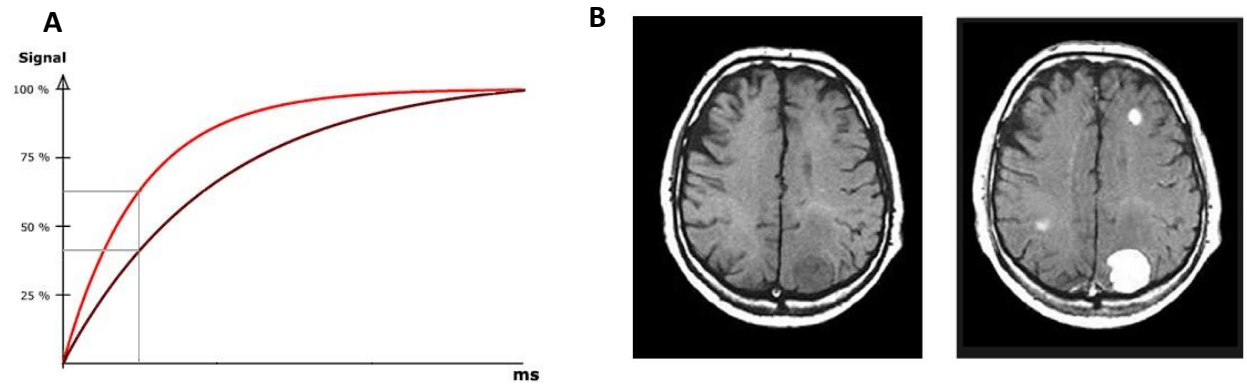

Figure 6. Increase of the MRI signal induced after the injection of T_1 contrast agent (A). The images (B) shows the effect of Gd-DTPA in the detection of brain metastasis on T1w axial images (**60**)

The mechanism for the generation of the T_1-based positive contrast will be described in the following paragraph.

2.2 T_1 contrast enhancement

Gadolinium(III), the most exploited paramagnetic metal ion able to give strong MRI T1-contrast, is quite toxic in living organisms: as matter of fact, it is claimed that it can interfere with the biological processes mediated by the divalent Ca(II) ion, due to the close similarity between the size of the two ions (Gd(III) 1.07 Å vs Ca(II) 1.14 Å) (**61**). To limit the toxicity issues and preserving the capability to generate T_1 contrast, Gd(III) ion can be entrapped in stable coordination "cages", typically represented by multidentate poly-amino-poly-carboxylate ligands, which can form metal complexes whose thermodynamic stabilitity and kinetic inertness are high enough to prevent transmetalation phenomena in presence of biological metals (*e.g.* Ca(II), Cu(II), Zn(II)).

Different ligands, starting from the reference compounds DTPA (Diethylenetriamine Pentaacetic acid) and DOTA (1,4,7,10-tetraazacyclododecane-1,4,7,10-tetraacetic acid), were developed during the years, leading to the development of a portfolio of clinically approved contrast agents (Figure 7) (**60**).

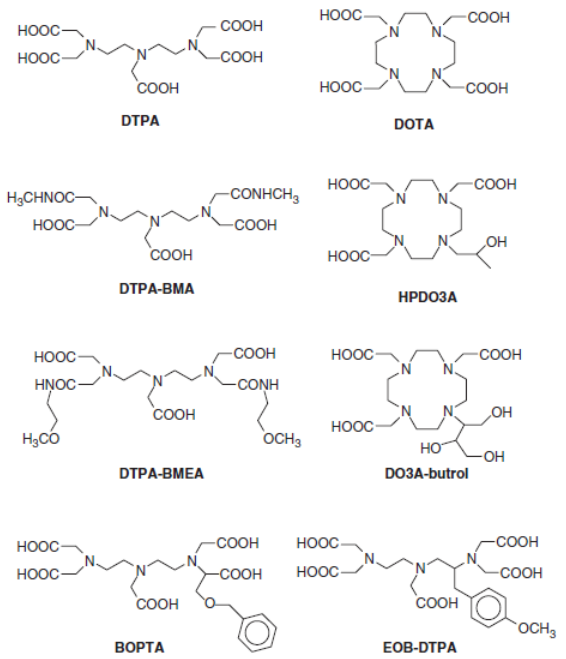

Complex	Brand name
$[GdDTPA(H_2O)]^{2-}$	Magnevist®
$[GdDOTA(H_2O)]^{-}$	Dotarem®
$[GdHPDO3A(H_2O)]$	ProHance®
$[GdDO3A\text{-}butrol(H_2O)]$	Gadovist®
$[GdDTPA\text{-}BMA(H_2O)]$	Omniscan®
$[GdDTPA\text{-}BMEA(H_2O)]$	OptiMARK®
$[GdBOPTA(H_2O)]^{2-}$	MultiHance®
$[GdEOB\text{-}DTPA(H_2O)]^{2-}$	Eovist®

Figure 7. List of the clinically approved Gd(III) chelating agent with the corresponding brand name and vendors.

The efficiency of a Gd-based agent to generate the MRI contrast is typically expressed in terms of its relaxivity, which corresponds to the increase of the longitudinal ($R_1 = 1/T_1$) relaxation rate normalized to one millimolar concentration of the paramagnetic metal complex:

[1] $$R_i = [CA]r_i + R_{iw} \quad i = 1$$

where R_{1w} is, in principle, the longitudinal or transverse relaxation rate of the bulk water protons measured in a solution containing a diamagnetic analog (e.g. based on La(III), Lu(III) or Y(III)) of the Gd-complex. However, the diamagnetic contribution can be sufficiently approximated by the value measured in a solution without the paramagnetic complex.

As previously mentioned, the relaxivity of a paramagnetic complex is a measure of the dipolar coupling between the magnetic moment of the unpaired electrons of the metal and the solvent water protons. This interaction is defined mainly by some contributions that reflect different solute-solvent interactions: Inner Sphere (IS), Outer Sphere (OS), and Second Sphere (SS). The first arises from the the exchanging water protons of H_2O molecule(s) directly bound to the paramagnetic metal, the second refers to the water molecules that diffuse close to the complex, and the latter identifies water protons interacting through hydrogen-bond, with specific moieties of the metal complex (e.g. polar groups).

Therefore, the overall relaxivity is the sum of these contributions:

[2] $$r_i = r_{ip}^{IS} + r_{ip}^{OS} + r_{ip}^{SS} \qquad i = 1$$

In small-sized complexes, IS and OS almost equally contribute to the relaxivity, whereas SS contribution becomes important in complexes containing polar moieties in their structure (*e.g.* phosphate or free carboxylic groups).

The IS contribution to the relaxivity is expressed by the following expression:

[3] $$r_{1p}^{IS} = \frac{[CA]q}{55.6} \frac{1}{T_{1M} + \tau_M}$$

where q indicates the number of water molecules bound to the metal center, τ_m is the resident life time of their protons, and T_{1M} represents their longitudinal relaxation time at the metal site. The latter parameter is described by the Solomon-Bloembergen-Morgan (SBM) equations. Briefly, it is

related to three main factors: i) the reorientational correlation time (τ_r), the residence lifetime of the bound water protons (τ_m), and the electron paramagnetic relaxation times (T_{ie}, i = 1,2).

[4] $$\frac{1}{\tau_{Ci}} = \frac{1}{\tau_R} + \frac{1}{\tau_M} + \frac{1}{T_{ie}} \qquad (i = 1, 2)$$

The modulation of the parameters describing the IS contribution (q, τ_R, and τ_M) is the typical approach to improve the efficiency of a Gd-based agent.

Clinically approved agents show q=1, but several attempts have been carried out to increase the hydration state of the metal ion from 1 to 2, without compromising thermodynamic stability and kinetic inertness.

The heptadentate ligand AAZTA (6-amino-6-methylperhydro-1,4-diazepinetetraacetic acid) is one of the most promising candidate in the family of q = 2 agents. Gd-AAZTA has a thermodynamic stability and kinetic inertness higher in comparison with linear compounds, showed no transmetalation in presence of Zn(II), Mn(II), or Ca(II), and showed a relaxivity (7.1 mM^{-1} s^{-1} at 0.5T at 25°C) ca. 50% higher than the reference compounds Gd-DTPA and Gd-DOTA (**60,62,63**). The advantages of this complex will be further discussed in Paragraph 3.1.

The reorientational correlation time is mainly dependent on the molecular size of the complex (**60**). Longitudinal relaxivity, especially at the magnetic field strength of interest for clinical MRI, is directly related to τ_R. Therefore, the restriction of the rotational motion of the complex leads to an increase of the relaxivity. This phenomenon will be further described in both Paragraph 2.1, 3.1, and 3.2, where it will be illustrated how the increase in the size of a paramagnetic complex can affect its relaxivity.

Finally, also τ_M, the residence lifetime of the inner sphere water molecules is a crucial parameter in defining r_1 values. It has been demonstrated that, especially for slow tumbling complexes, optimal values are in the 10-50 ns range (**60**). As the matter of fact, for values shorter than nanoseconds, there is no enough time for the water protons to be influenced by the metal center and, whereas, for τ_M longer than microseconds, the inner sphere contributions is “quenched” (see Equation 3), because of the non efficient transmission of the paramagnetic effect to the bulk solvent. Gd-AAZTA displays a τ_M value (at 25°C) of 90 ns (**62**), much closer to the ideal value than Gd-DTPA (300 ns) and Gd- DOTA (240 ns), thus making this complex particularly promising for *in vivo* imaging applications (**64**).

3 - Fluorescence Imaging Basics

Fluorescence is a radiative process for which a molecule called fluorophore suitably excited by a photon, emits an electromagnetic radiation with a wavelength longer than the exciting photon. The process can be described by the Jabłoński diagram reported in Figure 8.

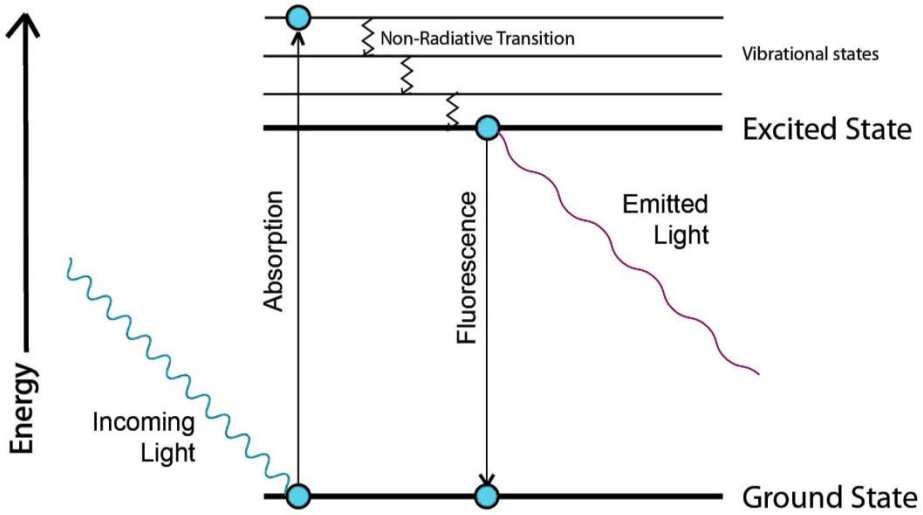

Figure 8. Graphical representation of the Jabłoński Diagram

The phenomenon is mainly composed by three-steps: 1) excitation, 2) excited-state lifetime, and 3) emission. The light absorption by the fluorophore brings an electron from the ground to any vibrational levels of a singlet excited state. From there, the electron reaches the lowest vibrational level of the excited state by loosing energy through non-radiative mechanisms. Then, the electron returns back to the ground state by emitting a photon. Since a fraction of the absorbed light energy is dissipated by vibrational interaction, the absorption wavelength is always shorter (higher energy) than the emitted one (**66**). The energy difference between absorption and emission photons is called Stoke shift. For polyatomic molecules in solution, the discrete electronic transitions are replaced by a broad range spectra called excitation and emission spectra, characteristic for each fluorescent molecule.

These molecular phenomena have been widely exploited to visualize cellular and subcellular processes with *in vivo* Optical Imaging (OI), a diffuse imaging technique especially at preclinical level. The most commonly used class of fluorophores for in vivo imaging applications is represented by cyanines (**66**). These dyes are typically characterized by two nitrogen heterocyclic rings joined by a conjugation chain of carbon atoms. Even if the Quantum Yield (the parameter that represented the ratio quantity of photon absorbed respect to the emitted one) it is not the highest for the

fluorescent dye, the characteristic emission make them perfect candidates for the *in vivo* applications (**67**). As a matter of fact, the emission in the Near infrared (NIR) spectrum avoid the overlap with endogenous autofluorescence signals (**68**) and considerably increase the light penetration inside the tissues (**69**). Despite the many advantages, the use of OI for deep tissue imaging remains a huge challenge: physical mechanisms, from absorption to scattering, represent an insurmountable obstacle for the "visible-NIR fluorescence light based'' imaging techniques.

In the last years, in vivo fluorescence imaging moved from the conventional diagnostic applications to the visualization of a lesion during a surgery intervention (Image-Guided Surgery) (**70,71**). In fact, during a surgical treatment, the tissue of the patient is directly exposed to the light, thus limiting the problem of the poor light penetration, and simplifying fluorescence acquisition by the camera. Exploiting the high sensitivity of the technique, it is possible to precisely localize even small tumor foci in the tissue. Moreover, the performance of this approach can be significantly improved using targeted fluorescence probes. The application of this technique in the surgical treatment of prostate cancer will be presented in Paragraph 3.3.

4 - Imaging of Pathological Conditions

The above mentioned techniques have been largely involved in the non-invasive identification of different types of pathological conditions. During this PhD project the attention has been mainly focused on two diffuse diseases such as neuroinflammation and prostate cancer.

4.1 Neuroinflammation

Neuroinflammation is finely related to many neurological diseases including Stroke, Alzheimer disease, Multiple Sclerosis and Central Nervous System (CNS) neoplasm (**72,73,74**). The interplay between neuroinflammation and CNS diseases is a delicate balance, which is finally aimed at repairing and regenerating the tissue, but that could bring also to brain damages. Many factors are involved in the activation and maintenance of neuroinflammation, from the production of cytokines/chemokine to the activation of resident microglia, (**75**) that brings to the infiltration of peripheral immune cells (monocytes, leukocytes) across the altered Blood Brain Barrier (BBB) (**76**). Though in the last years several diagnostic tools have been developed for imaging these pathologial conditions, there is still a strong demand for the design of improved imaging probes for a better visualization of neuroinflammation processes.

Brain imaging is limited by two issues: i) the presence of the skull, which can make difficult the use of less penetrating radiations, and ii) the BBB, which prevents the diffusion of many molecules (including the diagnostic probes) into the brain. However, given the difficulties of the therapeutic intervention in the late stage of the brain diseases, it is fundamental to identify neuroinflammation as an early stage as possible. PET, SPECT and MRI are the mainly exploited imaging techniques at clinical and preclinical levels, for the *in vivo* visualization of neuroinflammation (**76**). PET imaging is focused on the visualization of markers overexpressed inside the brain, mainly on resident immune cells as microglia. One of the most spread tracers in clinical research, despite its low BBB penetration and highly aspecific binding (**77**), is [^{11}C]PK11195, a molecule designed to detect the activity of traslocator protein (TSPO), a traslocation mitochondrial protein upregulated following microglia and astrocytes activation (**78**).

The relatively poor sensitivity of MRI makes very challenging to reach intracerebral targets with high concentration of the probe. Therefore, most of the work carried out so far aimed at: i) visualizing the recruitment of immune cells, by using specific cell-labelling agents, or ii) visualizing vascular biomarkers of inflammation, typically represented by the receptors involved in the chemoattraction, adhesion and transmigration of circulating immunocells (**79,80**). In this PhD

project, a nanosized MRI agent targeting the Vascular Adhesion Molecule 1 (VCAM-1) receptors, overexpressed on the vessel endothelial cells after cytokines stimulations (**81**), has been investigated (Chapters 2.1 and 2.2). Even if target negative contrast agents (e.g. USPIO, MPIO) were designed to recognize the receptor (**82,83**), the MRI signal obtained could be not univocal and confused with hemorrages, air of mineral deposit (**84**).

4.2 Prostate Cancer

Prostate is a small gland located in the pelvis area, surrounded by rectum and bladder and fundamental for the reproductive system in male (**85**). Uncontrolled proliferation of epithelial cells present in the gland leads to the development of Prostate Cancer (PCa). Nowadays, the disease is the most spread non-cutaneous cancer and one of the most lethal worldwide (**86**).

During the years, different diagnostic tools were developed: the two most spread are the physical rectal examination and PSA test. However, regarding the first method, especially for early stage of PCa, it is particularly complicated to identify the presence of the tumor. The PSA level, the most diffused diagnostic assay, cannot discriminate between tumor and Benign Prostate Hyperplasia (BPH) (**87**). Since this test is often ambiguous in the detection of the tumor, the physicians are often pushed to perform an invasive biopsy.

US, mp-(multi parametric)MRI and PET are imaging techniques used to non-invasively and precisely localize the tumor inside the gland. TRUS (Trans Rectal UltraSound), even being cheap and easy handling, could not clearly identify the malignancy, often confused with prostatitis, inflammation or BPH (**88**). mp-MRI is also commonly used as diagnostic tools and combines T_2-weighted MRI with functional (DWI and DCE) sequences. Even if the contrast in the tissue is excellent (much higher than US), it is really expensive and normally requires highly specialized experts to acquire and analyze images (**85,89**). PET, even offering information at different tumor stages, it is expensive and poses different technological and clinical challenges, such as the attenuation correction or radioactivity exposure (**85,90**). Finding an easy and reliable way to identify the prostate tumor is nowadays an essential need. In Paragraph 3.2 is proposed a novel probe for univocal tumor localization, based on T_1 contrast enhancement in MRI images.

The diagnosis of PCa is often followed, if the malignancy is identified, by surgery, radiotherapy of hormonal therapy. Especially with localized PCa, the most diffuse treatment is the complete surgical removal of the whole gland. This process, called Radical Prostatectomy (RP), is often associate with incontinence or erectile disfunction (**91,92,93**). Even if recently the use of robotic laparoscopic RP reduces drastically the side effects, then represent a disabling problem, especially for young patients

(**94**). In Paragraph 3.3, an optical image-guided surgery application to precisely localized the tumor cells in the prostate is discussed.

5 - Aim of the Thesis

The aim of the thesis is to design novel imaging probes for diagnostic and therapeutic purposes applied to different pathological conditions. In particular, the work has been focused on molecular and nanosized agents for MRI (diagnostic tool) and Optical Imaging (treatment tool), to detect two diffuse disease conditions such as neuroinflammation and prostate cancer. As discussed in **Paragraph 2.1**, a micellar probe, based on Gd(III) and tailored with an anti-VCAM-1 peptide, was synthesized, extensively characterized and tested on a peripheral model on muscle inflammation. Subsequently, in **Paragraph 2.2**, it is described how the system works on a neuroinflammation model induced by intra-striatal injection of LPS. Further characterizations were performed on brain endothelial cells and *ex vivo* studies underline the interplay of the micelles with the immunosystem in the brain.

The following paragraphs are mainly focused on prostate cancer detection, exploiting the two different techniques. **Paragraph 3.1** is mainly focused on the development of the tetrameric platform based on AAZTA chelating agent, for the easy bioconjugation of different vectors. The Gd-complex, that shows a high relaxivity in vitro, was firstly synthesized with a terminal amino group and properly modified adding different bioactive groups such as maleimide, aromatic aldehyde and dibenzocyclooctyne (DBCO). All the products were extensively characterized by HPLC-MS, NMR and relaxometry. The maleimide-activated compound was then exploited for the bioconjugation of the CREKA (Cys,Arg,Glu,Lys,Ala) peptide, able to recognize fibrin-fibronectin complexes. This target was exploited, as described in **Paragraph 3.2**, to perform efficient T_1 MRI imaging of prostate cancer and following the dynamic change of the MRI contrast *in vivo*. The orthotopic model was devised by injecting human PC3 cell line directly into the prostate of immune deficient mice. The latter model was exploited in **Paragraph 3.3** to test the designed optical probe as NIRF molecule for prostate image-guided surgery. After *in vitro* tests on prostate tumor cells, the distribution of the targeted dye was followed by NIRF imaging. Finally, preliminary tests of the effectiveness of the probe, mimicking the surgical conditions, were performed on an adapted ZEISS microscope for surgical purposes.

The general concluding remarks regarding all the different themes treated during the thesis will be reported in **Chapter 4.**

References

1. Weissleder, R.; Mahmood, U., Molecular imaging. *Radiology* 2001, *219* (2), 316-33.

2. James, M. L.; Gambhir, S. S., A molecular imaging primer: modalities, imaging agents, and applications. *Physiol Rev* 2012, *92* (2), 897-965.

3. Ido, T.; Wan, C. N.; Casella, V.; Fowler, J. S.; Wolf, A. P.; Reivich, M.; Kuhl, D. E., Labeled 2-Deoxy-D-Glucose Analogs - F-18-Labeled 2-Deoxy-2-Fluoro-D-Glucose, 2-Deoxy-2-Fluoro-D-Mannose and C-14-2-Deoxy-2-Fluoro-D-Glucose. *J Labelled Compd Rad* 1978, *14* (2), 175-183.

4. Gallagher, B. M.; Fowler, J. S.; Gutterson, N. I.; MacGregor, R. R.; Wan, C. N.; Wolf, A. P., Metabolic trapping as a principle of oradiopharmaceutical design: some factors resposible for the biodistribution of [18F] 2-deoxy-2-fluoro-D-glucose. *J Nucl Med* 1978, *19* (10), 1154-61.

5. Taegtmeyer, H.; Dilsizian, V., Imaging myocardial metabolism and ischemic memory. *Nat Clin Pract Cardiovasc Med* 2008, *5 Suppl 2*, S42-8.

6. Matsui, T.; Nakata, N.; Nagai, S.; Nakatani, A.; Takahashi, M.; Momose, T.; Ohtomo, K.; Koyasu, S., Inflammatory cytokines and hypoxia contribute to 18F-FDG uptake by cells involved in pannus formation in rheumatoid arthritis. *J Nucl Med* 2009, *50* (6), 920-6.

7. Takuma, K.; Kamisawa, T.; Itoi, T., Positive response to steroid therapy for autoimmune pancreatitis evaluated with fluorodeoxyglucose positron emission tomography. *Clin Gastroenterol Hepatol* 2010, *8* (5), e54-5.

8. Li, X. F.; Ma, Y.; Sun, X.; Humm, J. L.; Ling, C. C.; O'Donoghue, J. A., High 18F-FDG uptake in microscopic peritoneal tumors requires physiologic hypoxia. *J Nucl Med* 2010, *51* (4), 632-8.

9. Avril, N., GLUT1 expression in tissue and (18)F-FDG uptake. *J Nucl Med* 2004, *45* (6), 930-2.

10. Khandani, A. H.; Whitney, K. D.; Keller, S. M.; Isasi, C. R.; Donald Blaufox, M., Sensitivity of FDG PET, GLUT1 expression and proliferative index in bronchioloalveolar lung cancer. *Nucl Med Commun* 2007, *28* (3), 173-7.

11. Horiuchi, C.; Tsukuda, M.; Taguchi, T.; Ishiguro, Y.; Okudera, K.; Inoue, T., Correlation between FDG-PET findings and GLUT1 expression in salivary gland pleomorphic adenomas. *Ann Nucl Med* 2008, *22* (8), 693-8.

12. Krzeslak, A.; Wojcik-Krowiranda, K.; Forma, E.; Jozwiak, P.; Romanowicz, H.; Bienkiewicz, A.; Brys, M., Expression of GLUT1 and GLUT3 glucose transporters in endometrial and breast cancers. *Pathol Oncol Res* 2012, *18* (3), 721-8.

13. Wang, J.; Ye, C.; Chen, C.; Xiong, H.; Xie, B.; Zhou, J.; Chen, Y.; Zheng, S.; Wang, L., Glucose transporter GLUT1 expression and clinical outcome in solid tumors: a systematic review and meta-analysis. *Oncotarget* 2017, *8* (10), 16875-16886.

14. Pizzuti, L.; Sergi, D.; Mandoj, C.; Antoniani, B.; Sperati, F.; Chirico, A.; Di Lauro, L.; Valle, M.; Garofalo, A.; Vizza, E.; Corrado, G.; Tomao, F.; Rinaldi, M.; Carpano, S.; Maugeri-Sacca, M.; Conti, L.; Digiesi, G.; Marchetti, P.; De Maria, R.; Giordano, A.; Barba, M.; Carosi, M. A.; Vici, P., GLUT 1 receptor expression and circulating levels of fasting glucose in high grade serous ovarian cancer. *J Cell Physiol* 2017.

15. Kim, Y. H.; Jeong, D. C.; Pak, K.; Han, M. E.; Kim, J. Y.; Liangwen, L.; Kim, H. J.; Kim, T. W.; Kim, T. H.; Hyun, D. W.; Oh, S. O., SLC2A2 (GLUT2) as a novel prognostic factor for hepatocellular carcinoma. *Oncotarget* 2017, *8* (40), 68381-68392.

16. Chen, K.; Chen, X., Design and development of molecular imaging probes. *Curr Top Med Chem* 2010, *10* (12), 1227-36.

17. Joshi, B. P.; Wang, T. D., Exogenous Molecular Probes for Targeted Imaging in Cancer: Focus on Multi-modal Imaging. *Cancers (Basel)* 2010, *2* (2), 1251-87.

18. Lodish H, B. A., Zipursky SL, et al., Molecular Cell Biology. 4th edition. 2000, *New York: W. H. Freeman; 2000.*

19. Jiang, G.; Zhang, B. B., Glucagon and regulation of glucose metabolism. *Am J Physiol Endocrinol Metab* 2003, *284* (4), E671-8.

20. Wu, G.; Fang, Y. Z.; Yang, S.; Lupton, J. R.; Turner, N. D., Glutathione metabolism and its implications for health. *J Nutr* 2004, *134* (3), 489-92.

21. Dimitriadis, G.; Mitrou, P.; Lambadiari, V.; Maratou, E.; Raptis, S. A., Insulin effects in muscle and adipose tissue. *Diabetes Res Clin Pract* 2011, *93 Suppl 1*, S52-9.

22. Patel, Y. C., Somatostatin and its receptor family. *Front Neuroendocrinol* 1999, *20* (3), 157-98.

23. Merrifield, R. B., Solid Phase Peptide Synthesis. I. The Synthesis of a Tetrapeptide. 1963, *J. Am. Chem. Soc.* (85 (14)), pp 2149–2154.

24. White, W. C. C. a. P. D., Fmoc Solid Phase Peptide Synthesis: a practical approch. *Oxford University Press* 2000.

25. Zwick, M. B.; Shen, J.; Scott, J. K., Phage-displayed peptide libraries. *Curr Opin Biotechnol* 1998, *9* (4), 427-36.

26. Lee, S.; Xie, J.; Chen, X., Peptide-based probes for targeted molecular imaging. *Biochemistry* 2010, *49* (7), 1364-76.

27. Chen, X., Protein and peptide probes for molecular imaging. *Amino Acids* 2011, *41* (5), 1009-12.

28. Kim, L. T.; Yamada, K. M., The regulation of expression of integrin receptors. *Proc Soc Exp Biol Med* 1997, *214* (2), 123-31.

29. Liu, Z.; Wang, F.; Chen, X., Integrin alpha(v)beta(3)-Targeted Cancer Therapy. *Drug Dev Res* 2008, *69* (6), 329-339.

30. Beer, A. J.; Haubner, R.; Wolf, I.; Goebel, M.; Luderschmidt, S.; Niemeyer, M.; Grosu, A. L.; Martinez, M. J.; Wester, H. J.; Weber, W. A.; Schwaiger, M., PET-based human dosimetry of 18F-galacto-RGD, a new radiotracer for imaging alpha v beta3 expression. *J Nucl Med* 2006, *47* (5), 763-9.

31. Beer, A. J.; Grosu, A. L.; Carlsen, J.; Kolk, A.; Sarbia, M.; Stangier, I.; Watzlowik, P.; Wester, H. J.; Haubner, R.; Schwaiger, M., [18F]galacto-RGD positron emission tomography for imaging of alphavbeta3 expression on the neovasculature in patients with squamous cell carcinoma of the head and neck. *Clin Cancer Res* 2007, *13* (22 Pt 1), 6610-6.

32. Van Der Gucht, A.; Pomoni, A.; Jreige, M.; Allemann, P.; Prior, J. O., 68Ga-NODAGA-RGDyK PET/CT Imaging in Esophageal Cancer: First-in-Human Imaging. *Clin Nucl Med* 2016, *41* (11), e491-e492.

33. Shao, G.; Gu, W.; Guo, M.; Zang, S.; Fu, J.; Liu, S.; Wang, F.; Wang, Z., Clinical study of 99mTc-3P-RGD2 peptide imaging in osteolytic bone metastasis. *Oncotarget* 2017, *8* (43), 75587-75596.

34. Reubi, J. C.; Laissue, J.; Krenning, E.; Lamberts, S. W., Somatostatin receptors in human cancer: incidence, characteristics, functional correlates and clinical implications. *J Steroid Biochem Mol Biol* 1992, *43* (1-3), 27-35.

35. Gomez, M.; Ferrando, R.; Vilar, J.; Hitateguy, R.; Lopez, B.; Moreira, E.; Kapitan, M.; De Lima, F.; Aguero, B.; Gabriela Villegas, M.; Urdaneta, N.; Gutierrez, E.; Battegazzore, A.; Bayardo, K.; Silveira, A.; Lago, G.; Paez, A., [99mTc-OCTREOTIDE in patients with neuroendocrine tumors from the GI tract]

99mTc-OCTREOTIDE en pacientes con tumores neuroendocrinos gastroenteropancreaticos. *Acta Gastroenterol Latinoam* 2010, *40* (4), 332-8.

36. Chen, S. H.; Chang, Y. C.; Hwang, T. L.; Chen, J. S.; Chou, W. C.; Hsieh, C. H.; Yeh, T. S.; Hsu, J. T.; Yeh, C. N.; Tseng, J. H.; Chen, T. C.; Yen, T. C., 68Ga-DOTATOC and 18F-FDG PET/CT for identifying the primary lesions of suspected and metastatic neuroendocrine tumors: A prospective study in Taiwan. *J Formos Med Assoc* 2017.

37. Becker, A.; Hessenius, C.; Licha, K.; Ebert, B.; Sukowski, U.; Semmler, W.; Wiedenmann, B.; Grotzinger, C., Receptor-targeted optical imaging of tumors with near-infrared fluorescent ligands. *Nat Biotechnol* 2001, *19* (4), 327-31.

38. Licha, K.; Hessenius, C.; Becker, A.; Henklein, P.; Bauer, M.; Wisniewski, S.; Wiedenmann, B.; Semmler, W., Synthesis, characterization, and biological properties of cyanine-labeled somatostatin analogues as receptor-targeted fluorescent probes. *Bioconjug Chem* 2001, *12* (1), 44-50.

39. Chen, X.; Conti, P. S.; Moats, R. A., In vivo near-infrared fluorescence imaging of integrin alphavbeta3 in brain tumor xenografts. *Cancer Res* 2004, *64* (21), 8009-14.

40. Cheng, Z.; Wu, Y.; Xiong, Z.; Gambhir, S. S.; Chen, X., Near-infrared fluorescent RGD peptides for optical imaging of integrin alphavbeta3 expression in living mice. *Bioconjug Chem* 2005, *16* (6), 1433-41.

41. Wu, Y.; Cai, W.; Chen, X., Near-infrared fluorescence imaging of tumor integrin alpha v beta 3 expression with Cy7-labeled RGD multimers. *Mol Imaging Biol* 2006, *8* (4), 226-36.

42. Wu, P.; Brand, L., Resonance energy transfer: methods and applications. *Anal Biochem* 1994, *218* (1), 1-13.

43. Johansson, M. K.; Cook, R. M., Intramolecular dimers: a new design strategy for fluorescence-quenched probes. *Chemistry* 2003, *9* (15), 3466-71.

44. Klein, T.; Bischoff, R., Physiology and pathophysiology of matrix metalloproteases. *Amino Acids* 2011, *41* (2), 271-90.

45. Burtea, C.; Laurent, S.; Port, M.; Lancelot, E.; Ballet, S.; Rousseaux, O.; Toubeau, G.; Vander Elst, L.; Corot, C.; Muller, R. N., Magnetic resonance molecular imaging of vascular cell adhesion molecule-1 expression in inflammatory lesions using a peptide-vectorized paramagnetic imaging probe. *J Med Chem* 2009, *52* (15), 4725-42.

46. Ye, F.; Jeong, E. K.; Parker, D.; Lu, Z. R., Evaluation of CLT1-(Gd-DTPA) for Cancer MR Molecular Imaging in a Mouse Breast Cancer Model. *Bo Pu Xue Za Zhi* 2011, *2* (5), 325-330.

47. Tei, L.; Barge, A.; Geninatti Crich, S.; Pagliarin, R.; Negri, V.; Ramella, D.; Cravotto, G.; Aime, S., Target visualization by MRI using the avidin/biotin amplification route: synthesis and testing of a biotin-Gd-DOTA monoamide trimer. *Chemistry* 2010, *16* (27), 8080-7.

48. Morelli, J. N.; Runge, V. M.; Williams, J. M.; Beissner, R. S.; Tweedle, M., Evaluation of a fibrin-binding gadolinium chelate peptide tetramer in a brain glioma model. *Invest Radiol* 2011, *46* (3), 169-77.

49. Zhou, Z.; Wu, X.; Kresak, A.; Griswold, M.; Lu, Z. R., Peptide targeted tripod macrocyclic Gd(III) chelates for cancer molecular MRI. *Biomaterials* 2013, *34* (31), 7683-93.

50. Tan, M.; Wu, X.; Jeong, E. K.; Chen, Q.; Lu, Z. R., Peptide-targeted Nanoglobular Gd-DOTA monoamide conjugates for magnetic resonance cancer molecular imaging. *Biomacromolecules* 2010, *11* (3), 754-61.

51. Yoo, S. P.; Pineda, F.; Barrett, J. C.; Poon, C.; Tirrell, M.; Chung, E. J., Gadolinium-Functionalized Peptide Amphiphile Micelles for Multimodal Imaging of Atherosclerotic Lesions. *ACS Omega* 2016, *1* (5), 996-1003.

52. Ringhieri, P.; Mannucci, S.; Conti, G.; Nicolato, E.; Fracasso, G.; Marzola, P.; Morelli, G.; Accardo, A., Liposomes derivatized with multimeric copies of KCCYSL peptide as targeting agents for HER-2-overexpressing tumor cells. *Int J Nanomedicine* 2017, *12*, 501-514.

53. Henderson, R. G., Nuclear magnetic resonance imaging: a review. *J R Soc Med* 1983, *76* (3), 206-12.

54. Bley, T. A.; Wieben, O.; Francois, C. J.; Brittain, J. H.; Reeder, S. B., Fat and water magnetic resonance imaging. *J Magn Reson Imaging* 2010, *31* (1), 4-18.

55. Odaibo, S. G., A Quantum Mechanical Review of Magnetic Resonance Imaging. 2012.

56. Xiao, Y. D.; Paudel, R.; Liu, J.; Ma, C.; Zhang, Z. S.; Zhou, S. K., MRI contrast agents: Classification and application (Review). *Int J Mol Med* 2016, *38* (5), 1319-1326.

57. Weinstein, J. S.; Varallyay, C. G.; Dosa, E.; Gahramanov, S.; Hamilton, B.; Rooney, W. D.; Muldoon, L. L.; Neuwelt, E. A., Superparamagnetic iron oxide nanoparticles: diagnostic magnetic resonance imaging and potential therapeutic applications in neurooncology and central nervous system inflammatory pathologies, a review. *J Cereb Blood Flow Metab* 2010, *30* (1), 15-35.

58. Wang, Y. X.; Idee, J. M., A comprehensive literatures update of clinical researches of superparamagnetic resonance iron oxide nanoparticles for magnetic resonance imaging. *Quant Imaging Med Surg* 2017, *7* (1), 88-122.

59. Aime, S.; Cabella, C.; Colombatto, S.; Geninatti Crich, S.; Gianolio, E.; Maggioni, F., Insights into the use of paramagnetic Gd(III) complexes in MR-molecular imaging investigations. *J Magn Reson Imaging* 2002, *16* (4), 394-406.

60. Aime A., B. M., Terreno E., Gd(III)-BASED CONTRAST AGENTS FOR MRI. *ADVANCES IN INORGANIC CHEMISTRY* 2005, *VOLUME 57*.

61. Rogosnitzky, M.; Branch, S., Gadolinium-based contrast agent toxicity: a review of known and proposed mechanisms. *Biometals* 2016, *29* (3), 365-76.

62. Aime, S.; Calabi, L.; Cavallotti, C.; Gianolio, E.; Giovenzana, G. B.; Losi, P.; Maiocchi, A.; Palmisano, G.; Sisti, M., [Gd-AAZTA]-: a new structural entry for an improved generation of MRI contrast agents. *Inorg Chem* 2004, *43* (24), 7588-90.

63. Baranyai, Z.; Uggeri, F.; Giovenzana, G. B.; Benyei, A.; Brucher, E.; Aime, S., Equilibrium and kinetic properties of the lanthanoids(III) and various divalent metal complexes of the heptadentate ligand AAZTA. *Chemistry* 2009, *15* (7), 1696-705.

64. Powell, D. H. N., O. M.; Pubanz, D.; Helm, L.; Lebedev, Y. S.; Schlaepfer, W.; Merbach, A. E., Structural and dynamic parameters obtained from O-17 NMR, EPR, and NMRD studies of monomeric and dimeric Gd3+ complexes of interest in magnetic resonance imaging: An integrated and theoretically self consistent approach. *Journal of the American Chemical Society* 1996, *118 (39)*, 9333-9346.

65. Jablonski, A., Efficiency of Anti-Stokes Fluorescence in Dyes. *Nature* 1933, (131), 839–840

66. Williams, R. T.; Bridges, J. W., Fluorescence of Solutions: A Review. *J Clin Pathol* 1964, *17*, 371-94.

67. Shi, C.; Wu, J. B.; Pan, D., Review on near-infrared heptamethine cyanine dyes as theranostic agents for tumor imaging, targeting, and photodynamic therapy. *J Biomed Opt* 2016, *21* (5), 50901.

68. Monici, M., Cell and tissue autofluorescence research and diagnostic applications. *Biotechnol Annu Rev* 2005, *11*, 227-56.

69. Sandell, J. L.; Zhu, T. C., A review of in-vivo optical properties of human tissues and its impact on PDT. *J Biophotonics* 2011, *4* (11-12), 773-87.

70. Keereweer, S.; Van Driel, P. B. A. A.; Snoeks, T. J. A.; Kerrebijn, J. D. F.; de Jong, R. J. B.; Vahrmeijer, A. L.; Sterenborg, H. J. C. M.; Lowik, C. W. G. M., Optical Image-Guided Cancer Surgery: Challenges and Limitations. *Clinical Cancer Research* 2013, *19* (14), 3745-3754.

71. Vahrmeijer, A. L.; Hutteman, M.; van der Vorst, J. R.; van de Velde, C. J. H.; Frangioni, J. V., Image-guided cancer surgery using near-infrared fluorescence. *Nat Rev Clin Oncol* 2013, *10* (9), 507-518.

72. Amor, S.; Puentes, F.; Baker, D.; van der Valk, P., Inflammation in neurodegenerative diseases. *Immunology* 2010, *129* (2), 154-69.

73. Ellwardt, E.; Zipp, F., Molecular mechanisms linking neuroinflammation and neurodegeneration in MS. *Exp Neurol* 2014, *262 Pt A*, 8-17.

74. Faden, A. I.; Loane, D. J., Chronic neurodegeneration after traumatic brain injury: Alzheimer disease, chronic traumatic encephalopathy, or persistent neuroinflammation? *Neurotherapeutics* 2015, *12* (1), 143-50.

75. Becher, B.; Spath, S.; Goverman, J., Cytokine networks in neuroinflammation. *Nat Rev Immunol* 2017, *17* (1), 49-59.

76. Jacobs, A. H.; Tavitian, B.; consortium, I. N., Noninvasive molecular imaging of neuroinflammation. *J Cereb Blood Flow Metab* 2012, *32* (7), 1393-415.

77. Janssen, B.; Vugts, D. J.; Funke, U.; Molenaar, G. T.; Kruijer, P. S.; van Berckel, B. N.; Lammertsma, A. A.; Windhorst, A. D., Imaging of neuroinflammation in Alzheimer's disease, multiple sclerosis and

stroke: Recent developments in positron emission tomography. *Biochim Biophys Acta* 2016, *1862* (3), 425-41.

78. Liu, G. J.; Middleton, R. J.; Hatty, C. R.; Kam, W. W.; Chan, R.; Pham, T.; Harrison-Brown, M.; Dodson, E.; Veale, K.; Banati, R. B., The 18 kDa translocator protein, microglia and neuroinflammation. *Brain Pathol* 2014, *24* (6), 631-53.

79. Man, S. M.; Ubogu, E. E.; Ransohoff, R. M., Inflammatory cell migration into the central nervous system: A few new twists on an old tale. *Brain Pathology* 2007, *17* (2), 243-250.

80. Ley, K.; Laudanna, C.; Cybulsky, M. I.; Nourshargh, S., Getting to the site of inflammation: the leukocyte adhesion cascade updated. *Nat Rev Immunol* 2007, *7* (9), 678-89.

81. Wong, D.; Dorovini-Zis, K., Expression of vascular cell adhesion molecule-1 (VCAM-1) by human brain microvessel endothelial cells in primary culture. *Microvasc Res* 1995, *49* (3), 325-39.

82. McAteer, M. A.; Sibson, N. R.; von zur Muhlen, C.; Schneider, J. E.; Lowe, A. S.; Warrick, N.; Channon, K. M.; Anthony, D. C.; Choudhury, R. P., In vivo magnetic resonance imaging of acute brain inflammation using microparticles of iron oxide. *Nat Med* 2007, *13* (10), 1253-1258.

83. Gauberti, M.; Montagne, A.; Quenault, A.; Vivien, D., Molecular magnetic resonance imaging of brain-immune interactions. *Front Cell Neurosci* 2014, *8*, 389.

84. Zimny, A.; Neska-Matuszewska, M.; Bladowska, J.; Sasiadek, M. J., Intracranial Lesions with Low Signal Intensity on T2-weighted MR Images - Review of Pathologies. *Pol J Radiol* 2015, *80*, 40-50.

85. Sarkar, S.; Das, S., A Review of Imaging Methods for Prostate Cancer Detection. *Biomed Eng Comput Biol* 2016, *7* (Suppl 1), 1-15.

86. Siegel, R. L.; Miller, K. D.; Jemal, A., Cancer Statistics, 2017. *CA Cancer J Clin* 2017, *67* (1), 7-30.

87. Botchorishvili, G.; Matikainen, M. P.; Lilja, H., Early prostate-specific antigen changes and the diagnosis and prognosis of prostate cancer. *Curr Opin Urol* 2009, *19* (3), 221-6.

88. Harvey, C. J.; Pilcher, J.; Richenberg, J.; Patel, U.; Frauscher, F., Applications of transrectal ultrasound in prostate cancer. *Br J Radiol* 2012, *85 Spec No 1*, S3-17.

89. Sosnowski, R.; Zagrodzka, M.; Borkowski, T., The limitations of multiparametric magnetic resonance imaging also must be borne in mind. *Cent Eur J Urol* 2016, *69* (1), 22-23.

90. Schoder, H.; Gonen, M., Screening for cancer with PET and PET/CT: potential and limitations. *J Nucl Med* 2007, *48 Suppl 1*, 4S-18S.

91. Stitzenberg, K. B.; Wong, Y. N.; Nielsen, M. E.; Egleston, B. L.; Uzzo, R. G., Trends in radical prostatectomy: centralization, robotics, and access to urologic cancer care. *Cancer* 2012, *118* (1), 54-62.

92. Park, Y. H.; Jeong, C. W.; Lee, S. E., A comprehensive review of neuroanatomy of the prostate. *Prostate Int* 2013, *1* (4), 139-45.

93. Kung, T. A.; Waljee, J. F.; Curtin, C. M.; Wei, J. T.; Montie, J. E.; Cederna, P. S., Interpositional Nerve Grafting of the Prostatic Plexus after Radical Prostatectomy. *Plast Reconstr Surg Glob Open* 2015, *3* (7), e452.

94. Salinas, C. A.; Tsodikov, A.; Ishak-Howard, M.; Cooney, K. A., Prostate cancer in young men: an important clinical entity. *Nat Rev Urol* 2014, *11* (6), 317-23.

Chapter 2

Imaging of Inflammation

2.1- Targeting VCAM-1 Receptors for MRI Visualization of Inflammation

Based on:

Pagoto A., Stefania R., Garello F., Arena F., Digilio G., Aime S., Terreno E.
Paramagnetic Phospholipid-Based Micelles Targeting VCAM-1 Receptors for MRI Visualization of Inflammation, Bioconjugate Chemistry – 2016

Introduction

Inflammation is a complex phenomenon that implies a series of molecular and cellular modifications, such as changes in the vascular permeability and volume, infiltration, and activation of both circulating leukocytes and resident immune competent cells (**1**). Although the inflammatory response varies considerably with the nature of the insult, it occurs in many pathologies including atherosclerosis, cancer, and diseases of the nervous system (**2-4**). The activation of inflammatory cells in response to an injury is accompanied by the upregulation of endothelial inflammatory proteins, such as endothelial cell adhesion molecules (CAMs). These molecules (e.g., VCAM-1, ICAM-1, PECAM, and E- and P-selectins) play an important role in the tethering, rolling, adhesion, and extravasation of immune cells, in particular leucocytes (**5,6**). The molecular mechanisms responsible for specific recognition steps between activated cells and endothelium represent an intriguing opportunity for the design of imaging agents able to visualize the inflammation process. Furthermore, the intravascular localization of these epitopes makes them easily accessible for a systemically injected agent, and this feature is particularly important when a signal amplification strategy is necessary to detect the target-associated imaging response. Among CAMs, vascular cell adhesion molecule-1 (VCAM-1, member of the Ig superfamily) has been shown to be an important biomarker of several inflammatory disorders, mediating leukocyte movement across the endothelium, and its overexpression is recognized as a typical endothelial marker of inflammation (**7-9**), though it has been demonstrated to be involved also in other biological events (**10**). Most of the clinically available imaging techniques, namely, positron emission tomography (PET), computed tomography (CT), ultrasound (US), and magnetic resonance imaging (MRI) are currently under intense scrutiny for the design of protocols aimed at visualizing the inflammatory response (**11**). In virtue of the use of nonionizing radiations, as well as of the superb spatial resolution and ability to differentiate soft tissues, MRI is an excellent candidate to tackle this task. Moreover, MRI is often considered the technique of choice in the diagnosis of diseases with strong inflammatory components, such as stroke and atherosclerosis (**12-14**). Because of the poor sensitivity in the detection of molecular MRI agents, the search for signal amplification strategies is mandatory for the design of MR-molecular imaging protocols (**15**). Typically, the increase in sensitivity is achieved by loading a high number of imaging probes (e.g., Gd-complexes) on macromolecular or nano/microsized carriers. These systems (especially nano/microparticles) have a limited or null blood extravasation, thus making them optimal candidates for the detection of intravascular targets. Much efforts for the MRI visualization of inflammation have dealt with the use of agents

reporting about the recruitment of immune cells in the diseased region (**16, 17**). Nevertheless, MR-molecular imaging of inflammation using contrast agents directed to vascular inflammatory markers is an expanding field of research, and several successful examples have been already reported (**18**). In particular, VCAM-1 receptors have been exploited as MR-molecular targets in experimental models of cardiovascular and neurologic diseases, and in some cases, superparamagnetic iron oxides particles were used as imaging reporting units (**19-22**). Though quite sensitive, such particles generate a T_2*/T_2 contrast that leads to a loss of MRI signal, thus making difficult their detection in tissues with intrinsically low signals. In this respect, contrast agents that yield a T_1 weighted signal enhancement, as Gd- or Mn-based probes, appear preferable. So far, two examples of Gd-based T_1 agents targeting VCAM-1 receptors can be found in the literature. In one case, a monomeric Gd-DOTA-like complex (DOTA: 1,4,7,10-tetraazacyclododecane-1,4,7,10-tetraacetic acid) was conjugated to a peptide selected by phage display showing high affinity to the target (**23**). Quite unexpectedly, the presence of a single Gd per targeting vector (relaxivity of ca. 7.0 $s^{-1}mMGd^{-1}$ at 1.5 T and 37 °C) allowed for the detection of inflamed states in mice models of hepatitis (MRI contrast enhanced by a factor of 3 with respect to the control untargeted agent) and atherosclerosis (enhancement of a factor <2 in comparison with the agent conjugated with a scrambled untargeted peptide) in mice models. The second study dealt with rod-like nanoparticles of tobacco mosaic virus that were covalently conjugated to a VCAM-1 peptide and loaded with ca. 1200 units of a Gd-DOTA-like complex (relaxivity of 14.6 $s^{-1}mMGd^{-1}$ at 1.5 T and 25 °C) (**24**). Injected in a mouse model of atherosclerosis, this agent produced a 2-/3-fold increase in MRI contrast when compared with that obtained on both healthy mice and diseased animals administered with free Gd-DOTA.

With the aim to further improve the MRI detectability of VCAM-1 receptors using Gd-based agents, we report here a new nanosized agent based on mixed micelles made of a pegylated phospholipid, an amphiphilic Gd-complex, and a newly synthesized phospholipid conjugated to the VCAM-1 targeting peptide (DSPE-PEG2000-peptide in Scheme 1). We tested the in vivo MRI performance of the paramagnetic micelles on a LPS (lipopolysaccharide)-induced peripheral inflammation model in mice (**25**).

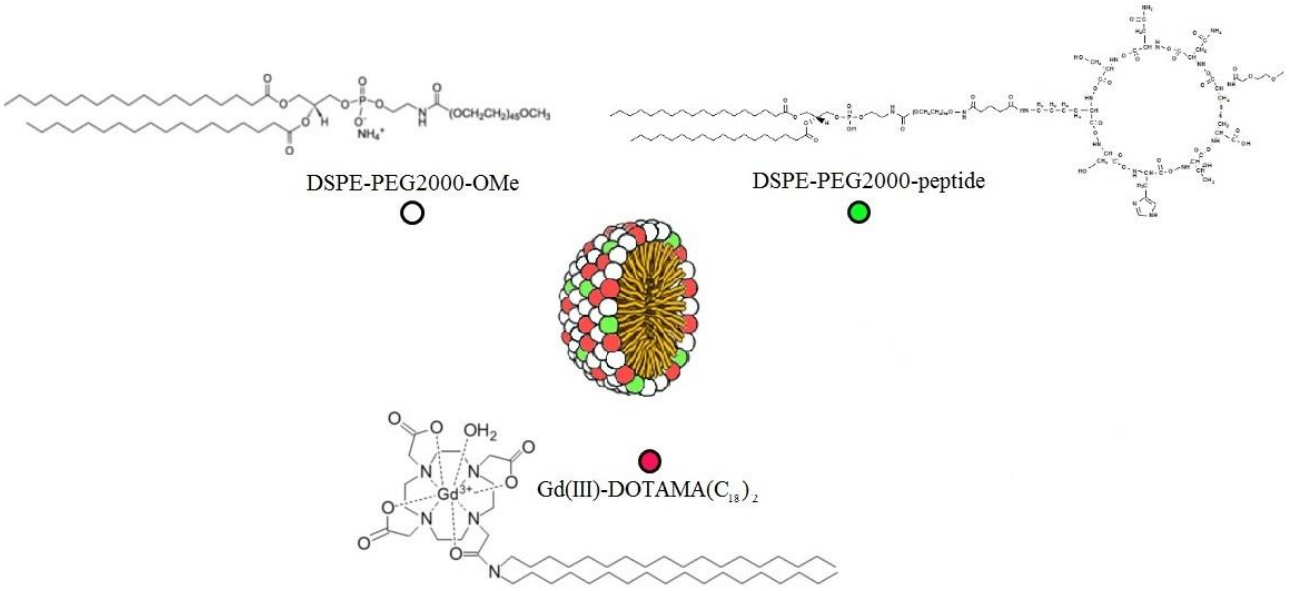

Scheme 9. Micelle Composition: DSPE-PEG2000-OMe (white circle), DSPE-PEG2000-peptide (green circle), and Gd(III)-DOTAMA(C_{18})$_2$ (red circle)

Experimental Procedures

Chemicals

1,2-Distearoyl-sn-glycero-3-phospho-ethanolamine-N-[amino(poly(ethyleneglycol)2000] ammonium salt (DSPE-PEG2000-NH_2) and 1,2-distearoyl-sn-glycero-3-phosphoethanolamine-N-[methoxy(polyethylene glycol)-2000] ammonium salt (DSPE-PEG2000-OMe) were obtained from Avanti Polar Lipids (Alabaster,USA). Gd-DOTAMA(C_{18})$_2$ was synthesized as described elsewhere (**43**). Disuccinimidyl glutarate (DSG) was prepared in-house from glutaric acid and NHS.

Synthesis of the Targeting Peptide and Its Scrambled Version

The cyclic (*represents the cyclization points) peptides C*NNSKSHTC* and HSC*NKNSC*T were synthesized on a Liberty CEM microwave peptide synthesizer using H-Cys(Trt)-2-chlorotrityl resin and standard FMOC (fluorenylmethyloxycarbonyl chloride) chemistry. The attachment of the first amino acid Fmoc-Cys-(Trt)–OH or Fmoc-Tyr(tBu)–OH to 2-chlorotrityl chloride resin to give H-Cys(Trt)-2-chlorotrityl resin was carried out as follows. Fmoc-Cys-(Trt)–OH (3.28 g, 5.6 mmol) or Fmoc-Tyr(tBu)–OH (2.76 g, 6 mmol) was dissolved in 5 mL of DCM (dichloromethane) and then added to DIPEA (diisopropylethylamine) (0.896 mL, 5.12 mmol). The mixture was stirred for 10 min. While under stirring, 2-chlorotrityl chloride resin (2.0 g, 2.24 mmol,) was added. The resulting mixture was continuously stirred for 3 h. The resin was filtered and washed with DCM (10 mL × 6 washings 3 min each). The resin was capped with MeOH (methanol)/DIPEA (5:1, 10 mL × 3 times)

for 5 min. The resin was first washed with DMF (dimethylformamide) (10 mL × 6 times, 3 min each) and then in DCM (10 mL × 3 times, 3 min each). Next, the resin was dried for 12 h under high vacuum. Yield >90%. Substitution: 0.59 mmol/g. The remaining amino acids were coupled automatically by using 5.0 equiv excess of Fmoc-amino acids, 5 min at 75 °C, 35 W, in the presence of PyBOP (benzotriazol-1-yl-oxytripyrrolidinophosphonium hexafluorophosphate), and DIPEA in DMF, and the Fmoc-deprotection steps (20% piperidine in DMF) were completed within 3 min at 75 °C. The cleavage from the resin was pursued with TFA (Trifluoroacetic)/TIPS (Triisopropylsilane)/EDT (ethanedithiol)(95:3:2, v/v) for 2 h at room temperature. The peptide was then precipitated and washed with diethyl ether. The obtained solid was dissolved in water with 5% of DMSO (dimethyl sulfoxide) and stirred for 24 h to afford the cyclization of the two Cys residues within the peptides. The solution was lyophilized to give the final product (166 mg, yield 61%, purity = 91% for C*NNSKSHTC* and 72 mg, yield 65%, and purity 92% for HSC*NKNSC*T). Analytical HPLC-MS was carried out on a Waters Fraction Lynx autopurification system equipped with micromass ZQ (ESCI ionization mode and dual-λ detectors), a Waters Atlantis RP-C18 column, 5 µm, 4.6 mm × 150 mm, eluents A, H_2O(0,1% TFA); B, CH3CN (0,1% TFA), elution initial condition 5% B, linear gradient 5–10% B over 2.49 min, 10–15% B over 15 min, flow rate 1 mL/min, and UV detection at 220 nm. t_R = 8.4 min, MS-ESI(+) m/z: 1107 $[M + H]^+$, 554 $[M+2H]^{2+}$, calculated for $C_{41}H_{66}N_{14}O_{18}S_2$ = 1106. The corresponding data for HSC*NKNSC*T were tR = 9.4 min. MS-ESI(+): m/z: found. 1106 $[M + H]^+$, 554 $[M+2H]^{2+}$ calculated for $C_{41}H_{66}N_{14}O_{18}S_2$ = 1106.

Peptides were also characterized by ^1H NMR and 2D-TOCSY, NOESY, and COSY spectra in H_2O (0.550 mL)–D_2O (0.050 mL) at pH 5 and room temperature. NMR spectra were recorded on Bruker Avance 600 spectrometer and analysed using the Computed Aided Resonance Assignment software (The Swiss Federal Institute of Technology, Zurich, Switzerland).

Preparation and Purification of DSPE-PEG2000-Peptide

A solution of the cyclic nonapeptide (0.020 g, 0.017 mmol) dissolved in anhydrous DMF (1.0 mL) was added to a solution of DSG (41.0 mg, 0.128 mmol) dissolved in anhydrous DMF (0.5 mL) containing DIPEA (0.057 mL, 0.34 mmol, 20 equiv), and the solution was vigorously shaken for 2 min. The reaction mixture was stirred for 5 min. Then, 10 mL of ethyl acetate was added to the reaction mixture, and the precipitate, corresponding to the glutaric acid monoamide mono-NHS ester of the peptides, was centrifuged to a pellet and washed twice with ethyl acetate (10 mL). A solution of this product in anhydrous DMSO (0.5 mL) containing DIPEA (0.050 mL, 0.3 mmol, 20 equiv) was added to a DMSO solution (0.5 mL) of DSPE-PEG2000-NH2 (0.021 g, 0.0075 mmol, 0.5 equiv), and the

mixture was stirred at room temperature. The reaction was monitored by analytical HPLC and reached completeness after 24 h. The reaction mixture was added with 10 mL of water and then lyophilized. The products were purified by preparative HPLC using a Waters XTerra RPdC_8, 19/100 column, 7 mM CH_3COONH_4 (A) e CH_3CN (B) as eluents, initial condition 40% B, 40–80% B in 2.45 min, 80–90% B in 7 min, and flow rate 20 mL/min.

Analytical HPLC: t_R = 17.55 min, purity 70%, a Fluofix 120 E (4.6 mm × 250 mm) column, eluents, A, H2O, and B, ethanol/isopropyl alcohol 70:30 (v/v), elution, initial condition 20% B, isocratic gradient 20% B in 5 min, 20–80% B in 20 min, 80–100% B in 3 min, flow rate 1.2 mL/min, column temperature 40 °C, and ELSD detection (temp 45 °C, pressure 35 atm).

C*NNSKSHTC*: MS-MALDI–TOF m/z 4017 calcd $C_{178}H_{333}N_{16}O_{74}PS_2$ = 3974.

HSC*NKNSC*T: MS-MALDI–TOF m/z 4005 calcd $C_{178}H_{335}N_{17}O_{74}PS_2$ = 3977

Mixed Micelle Preparation

Micelles were formulated with DSPE-PEG2000-OMe, Gd-DOTAMA(C_{18})$_2$, and DSPE-PEG2000-VCAM1-pep (or scr) in a molar ratio of 58:40:2. The mixture (total amount 22.5 mg) was dissolved in chloroform and MeOH (4:1 v/v), and the solution was slowly evaporated (30 °C) to form a thin film on the bottom of a flask. The film was hydrated at 50 °C for 10 min adding 1.5 mL of HEPES-buffered saline (pH 7.4, 38 mM of HEPES, 0.15 M of NaCl). The suspension was sonicated twice for 90 s (power 70%, Sonicator Bandelin Sonoplus HD 2070, Berlin, Germany). During sonication, the mixture was cooled with ice to keep the temperature under 10 °C.

Micelle Characterization

The millimolar longitudinal relaxivity (r_1) of the paramagnetic nanoparticles was measured at 0.5 T (Stelar Spinmaster Spectrometer, Pavia, Italy). The concentration of Gd(III) in the micelle suspension was determined by relaxometry (**44**). The mean hydrodynamic diameter of the particles was determined using dynamic light scattering (Malvern ZS Nanosizer, UK) with a scattering angle of 90 °C. The polydispersion index (PDI) was used as an indicator of the particle size distribution. Micelle stability was investigated monitoring longitudinal relaxivity and size over 5 days (DLS) and 15 days (relaxometry) in human serum (HS, SERO, Billingstad, Norway). The relaxation rate of the micelle-containing suspension was also measured at 25 °C over magnetic field strengths ranging from 7 to 20 MHz (Spinmaster FFC2000 1T C/DC, Stelar, Mede (PV), Italy). Additional values at higher Larmor frequencies (30–70 MHz) were obtained with a tunable relaxometer (Spinmaster, tunable magnet, Stelar, Mede (PV), Italy). Temperature was controlled with a Stelar VTC-91 airflow heater equipped with a calibrated copper–constantan thermocouple (uncertainty of ± 0.1 K). Variable-

temperature ^{17}O NMR measurements were recorded on a Bruker Avance 600 spectrometer equipped with a 5mm probe and standard temperature control unit. The micelle suspension contained 2.0% of ^{17}O water (Cambridge Isotope).

The observed transverse relaxation rates were calculated from the signal width at half-height. The diamagnetic contribution was calculated using a suspension of Gd-free micelles.

The number of Gd(III)-complexes loaded in a single micelle was estimated as follows:

[1] $$n_{micelle}^{Gd} = \frac{n_T^{Gd}}{n_T^{micelle}}$$

where n_T^{Gd} and $n_T^{micelle}$ represent the total number of Gd-complexes and particles, respectively. $n_T^{micelle}$ can be obtained from the ratio between the total surface area of the micelles (A_T) over the surface of the single, spherical, particle:

[2] $$n_T^{micelle} = \frac{A_T}{A_{single}} = \frac{A_T^{Gd} + A_T^{DSPE}}{4\pi r^2} = \frac{mol^{Gd} N_{AV} A^{Gd} + mol^{DSPE} N_{AV} A^{DSPE}}{4\pi r^2}$$

where the $mol^i N_{AV}$ terms refer to the number of Gd-complexes (i = Gd) and DSPE molecules (i = DSPE) in a given micelle suspension, A^i values represent the molecular surface areas for the two components, and r is the average particles radius (N_{AV} is the Avogadro's constant).

Under the assumption that the molar ratio between the micelle components does not vary during the preparation:

[3] $$mol^{DSPE} = mol^{Gd} \frac{\%^{DSPE}}{\%^{Gd}}$$

where $\%^i$ represents the molar ratio of the i component in the formulation (in this work, 40% and 60% for Gd-DOTAMA(C_{18})$_2$ and DSPE-PEG2000, respectively).

Equation 1 can be rearranged considering eqs 2 and 3 and substituting n_T^{Gd} with $mol^{Gd}N_{AV}$:

[4] $$n_{micelle}^{Gd} = \frac{mol^{Gd} N_{AV}}{\frac{mol^{Gd} N_{AV} A^{Gd} + mol^{Gd} \frac{\%^{DSPE}}{\%^{Gd}} N_{AV} A^{DSPE}}{4\pi r^2}} = \frac{4\pi r^2}{A^{Gd} + \frac{\%^{DSPE}}{\%^{Gd}} A^{DSPE}}$$

Animal Model

C57BL/6J male mice (20–25 g) were divided into two groups: (A) LPS inflamed mice receiving the targeted micelles (n = 6) and (B) LPS inflamed mice receiving the untargeted micelles exposing the

scrambled peptide (n = 6). The inflammation was induced in the right calf muscle by intramuscular injection of 100 µL of LPS 0.5 mg/mL in PBS (phosphate buffered saline) (LPS, Escherichia coli 055:B5) under 1.5% isoflurane anesthesia. In control mice, 100 µL of PBS was injected in the right calf muscle. Animals were recruited for MRI 48 h after LPS injection. The model was validated histologically. To this purpose, 48 h post-LPS injection, right and left legs were excised and immediately cryopreserved in optimum cutting temperature (O.C.T.) compound (VWR International) (5 min in liquid nitrogen before cooling down to −80 °C). Slices (thickness 5 µm) were cut using a cryostat (Leica CM 1950) and fixed in formalin for 10 min. Sections were then hydrated, stained with hematoxylin and eosin, and dehydrated to be mounted with a coverslip. Images of the samples were obtained by using an Olympus BH2 optical microscope.

Animal manipulation and experimental procedures were carried out in accordance with the European Community guidelines, and under the approval of the Italian Ministry of Health.

Immunofluorescence

Indirect immunofluorescent detection and localization of VCAM-1 receptors were performed. Sections (5-µm thick) of the leg muscles were cut with a cryostat (Leica CM 1950) and then fixed with ethanol 99% at room temperature for 8 min and washed with PBS. To block nonspecific binding sites, sections were incubated for 1 h with 10% BSA (Bovine Serum Albumin) in PBS. Sections were then incubated with primary Ab (ab24853, Abcam) at 4 °C (diluted 1:200 for VCAM-1 in PBS containing 10% BSA) overnight. After three washings with PBS, sections were incubated for 60 min with FITC-tagged goat antirat IgG (35552, ThermoFisher) (1:500 dilution in PBS) at room temperature. After washings with PBS, sections were stained with Hoechst (33342, Sigma) (1:10000 dilution in PBS for nuclear staining). After quick (5 min) washing in bidistilled water, the sections were mounted with ProLong (ThermoFisher) antifade mountant. Microscopic observation and image acquisition were performed with a Leica TCS SP5 confocal microscope (Leica Microsystems s.r.l.).

In Vivo MRI Experiments

48 h post-LPS injection, 200 µL of a suspension of targeted or untargeted micelles (0.055 mmol Gd/kg bw) were intravenously administered to C57BL/6J mice. MRI was performed before and then 20 min, 40 min, 4, 4.5, and 24 h after micelle injection on a Bruker Icon (1 T). A RARE sequence with the following acquisition parameters was used: TR/TE = 380/14.7 ms, matrix = 256, number of

averages = 6, FOV = 5 cm, slice thickness = 1.5 mm, 121 axial slices, and TA = 254 s. Mice were kept under isoflurane anesthesia during image acquisition.

ICP-MS Measurements

ICP-MS (Thermo Scientific ELEMENT 2 ICP-MS -Finnigan, Rodano, Milano, Italy) was used to quantify Gd (III) on explanted tissues. Inflamed and contralateral healthy muscles of mice injected with the micelles were resected 4 h post injection. The specimens were digested in nitric acid (1 mL) and then mineralized at 160 °C under microwave heating (Milestone MicroSYNTH Microwave labstation equipped with an optical fiber temperature control and HPR-1000/6 M six position high-pressure reactor, Bergamo, Italy).

Image Processing and Analysis

Image analysis was performed using Bruker ParaVision 4.0 software. Regions of interest (ROIs) were manually drawn over the inflamed and controlateral healthy legs in all the axial imaging slices, and the average signal intensity was calculated. The % T_1 contrast enhancement at a given time after administration (% $T1^{enh}{}_{(t)}$) was obtained as follows:

$$\%T_1^{enh}{}_{(t)} = \frac{S_{(t)}^{POST} - S^{PRE}}{S^{PRE}} \times 100$$

where S^{PRE} and $S_{(t)}^{POST}$ represent the average signal before and after the injection of the contrast agent, respectively (**35**). p values were calculated using Student's t-test, assuming statistical significance at $p < 0.05$ and $p < 0.01$.

Results

The VCAM-1 receptor targeting cyclic nonapeptide C*NNSKSHTC* and its untargeted scrambled version HSC*NKNSC*T were synthesized by solid phase peptide synthesis. The first amino acids (C and T, respectively) were attached to the resin manually, whereas the remaining amino acids were sequentially and automatically conjugated afterward. The thus-obtained linear nonapeptides were cleaved from the resin using a solution of TFA /TIPS /EDT and then cyclized to obtain the final products (yield ca. 60%). Next, the peptides were reacted with DSG to conjugate the mono-N-hydroxy succinimide (NHS) ester at the amino group of the Lys residue of the cyclic peptides (Scheme 2). The activated NHS moiety allowed for the conjugation of DSPE-PEG2000-NH_2 to form DSPE-PEG2000-VCAM1-pep and DSPE-PEG2000-scr-pep with a yield of about 50% (**26**). The

formation of the products was monitored by analytical HPLC, whereas purification was carried out by preparative HPLC using a buffered solution of ammonium acetate as eluent. The characterization of the final products was performed by ^{1}H NMR and mass spectrometry. A purity around 70% was determined by analytical HPLC-ELSD for both of the compounds. The remaining 30% was represented by the unconjugated phospholipid DSPE-PEG2000-NH_2. Because of the small amount of targeting phospholipid used in the formulation, it can be assumed that the unconjugated phospholipid (whose amount was in any case considered in the formulation of the micelles) did not interfere with the micelle formation.

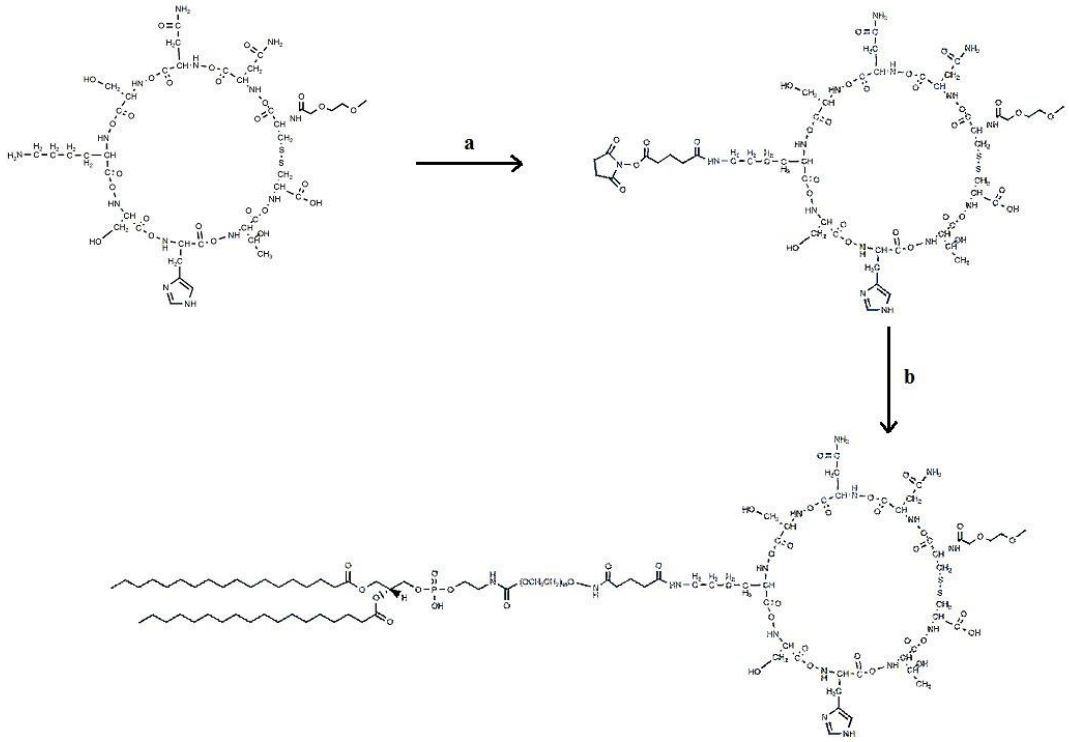

Scheme 2. Synthetic Pathway to DSPE-PEG2000-VCAM1-pep (a) DSG, DIPEA, DMF, 2 min; (b) DSPE-PEG2000-NH_2, DIPEA, DMSO, 24 h.

Preparation and Characterization of the Mixed Micelles

Paramagnetic mixed micelles were prepared by blending DSPE-PEG2000-OMe, DSPE-PEG2000-VCAM1-pep (or DSPE-PEG2000-scr-pep), and Gd-DOTAMA(C_{18})$_2$ in the molar ratio of 58:2:40, respectively. The hydrodynamic diameter of the micelles (determined by DLS on 3 batches) was 20 nm with a PDI of 0.2 ± 0.1. The millimolar longitudinal relaxivity (r1) at 0.5 T of the micelles exposing the targeting peptide was 34.9 s^{-1} $mmolGd^{-1}$ at 25 °C and 35.3 s^{-1} $mmolGd^{-1}$ at 37 °C. The relaxivity was also measured as a function of the proton Larmor frequencies (from 0.01 to 70 MHz), and the experimental data are reported in Figure 1 (left).

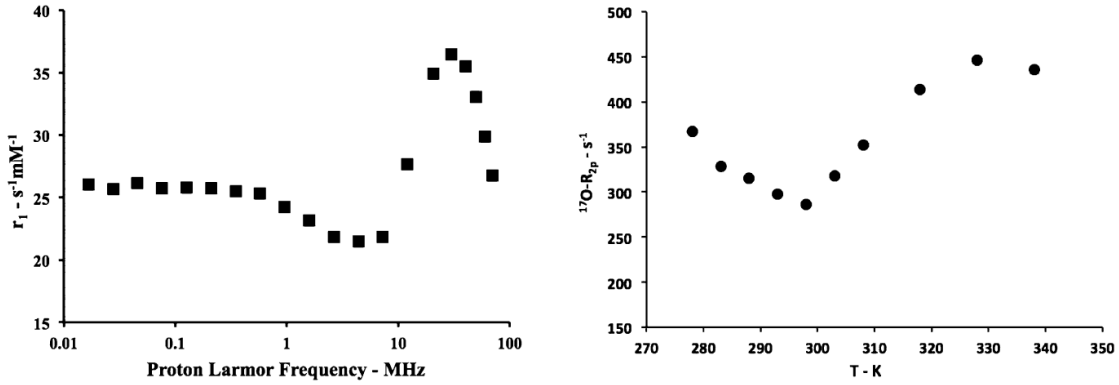

Figure 1. NMRD profile at 25 °C (left) and temperature dependence of water ^{17}O-R_2p (right, normalized to 20 mM of Gd) of VCAM-1 targeted paramagnetic micelles.

The obtained NMRD (nuclear magnetic relaxation dispersion) profile is characterized by a relaxivity hump at ca. 20–30 MHz, a feature that clearly indicates the occurrence of a restricted rotational motion for the paramagnetic Gd-complexes in the micelles (**27**). The NMRD data were complemented by the measurement of the temperature dependence of the transverse relaxation of ^{17}O-water, from which it is possible to determine the exchange lifetime, τ_M, of the water molecule coordinated to the metal center. Very interestingly, the data displayed a "two-component" behavior, thus indicating the presence of two species with very different exchange dynamics of their Gd-bound waters (Figure 1, right) (**28,29**). Since several parameters controlling ^1H and ^{17}O relaxation rates are common, NMRD and ^{17}O-data were analyzed simultaneously according to the well-established Solomon–Bloembergen–Morgan and Freed theories (**27**).

As such theories have some limitations to properly model the behaviour of slowly tumbling systems at low Larmor frequencies (**30**), NMRD data were analysed only in the high-frequency region (>5 MHz).

The results from the fitting of experimental vs calculated values are reported in Table 1, whereas Figure 2 shows the fitting curves as well as the relative contributions of the two species to the measured relaxation rates.

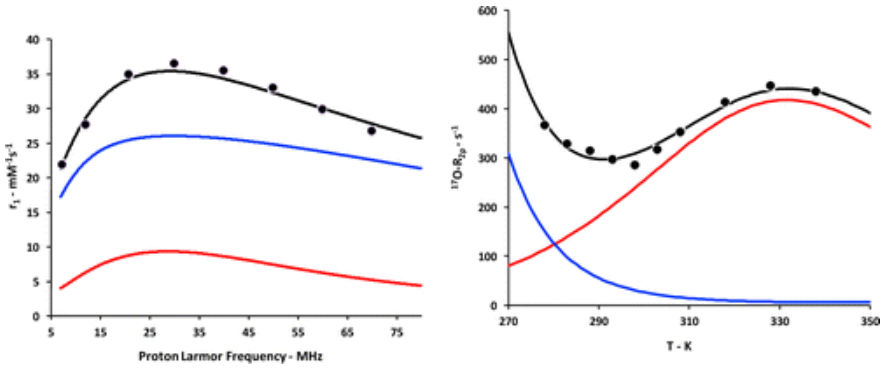

Figure 2. NMRD (left) and ^{17}O-data (right) analyzed according to the SBM-Freed theory for a system containing two species. Red and blue lines represent the contribution from species 1 and 2, respectively.

parameter	species 1 (SAP)	species 2 (TSAP)
$\Delta^2 \times 10^{19}$ (s^{-2})	2.2 ± 0.9	0.9 ± 0.1
τ_V (ps)	58.7 ± 4.9	41.4 ± 11.9
τ_M (ns)	380.1 ± 21.4	1.5 ± 0.2
τ_R (ns)	7.9 ± 0.8	7.5 ± 0.7
mol. fraction (%)	21.1	78.9

[a]The values of τ_V, τ_M, and τ_R refer to 25 °C.

Table 1. Values of the Parameters Obtained from the Simultaneous Fitting of NMRD and ^{17}O-R_{2p} Data for the VCAM-1 Targeted Paramagnetic Micelles.

The analysis was carried out by considering Δ^2, τ_V, τ_R, τ_M, and the molar fraction of the two species (assumed to be temperature independent) as variable parameters, whereas the following parameters were kept fixed during the fitting procedure: r_{Gd-H} = 3.0 Å (SAP), 3.1 Å (TSAP); r_{Gd-O}= 2.5 Å, D = 2.25 × 10^{-5} cm^2s^{-1}, q = 1, a = 3.8 Å, and A/h = −3.8 × 10^6. The activation energies related to the dynamic parameters obtained from the analysis were $E_{\tau V}$ = 7.8 kJ/mol, $E_{\tau R}$ = 13.1 kJ/mol, $E_{\tau M}$ = 27.2 kJ/mol (SAP); $E_{\tau V}$ = 0.9 kJ/mol, $E_{\tau R}$ = 10.7 kJ/mol, and $E_{\tau M}$ = 53.7 kJ/mol (TSAP). As it has been reported that the hydration state (expressed by the q/r^6 value) of Gd(III) in macrocyclic conformers with different water exchange rates is inversely related to the τ_M value (**31,32**), the analysis was performed using r_{Gd-H} values of 3.0 and 3.1 Å for species 1 and 2, respectively (**31**). The good quality of the data fitting is an indirect proof that the advantages deriving from a fast water exchange rate are partially limited by a reduced hydration state. The result of the analysis is consistent with the presence of two paramagnetic species with a predominance of the complex with a very short water exchange lifetime (species 2). The occurrence of a very short τ_M may considerably reduce the contribution of the complex to the water ^{17}O-R_{2p} values as the temperature increases. Conversely, the contribution from the complex with the slower water exchange rate (species 1) displayed a monotonic increase of ^{17}O-R_{2p}values with temperature. Therefore, in spite of the higher amount of the species 2 in the solution, ^{17}O-R_{2p} relaxation is almost exclusively determined by species 1 at physiological temperature. However, the effect of τ_M on the proton relaxivity is quite different, and the r_1 values of the micellar agent are mainly determined by the contribution of the species 2 over the entire interval of magnetic field strengths investigated. The *in vitro* stability of the micelles was assessed at 37 °C in human serum, by measuring both size and proton relaxation rate as a function of time. The stability of the nanoparticles was excellent, and no changes in size and R_1 values were observed over a period of 5 days.

In Vivo MRI Testing of the Paramagnetic Micelles

The *in vivo* MRI performance of the micelles was tested on a murine inflammation model obtained by injecting LPS in the mouse leg skeletal muscles. Conventional H&E (hematoxylin and eosin) histology confirmed the extensive infiltration of monocytes, lymphocytes, and neutrophils in the leg 48 h after LPS injection (Figure 3). Furthermore, immunofluorescence experiments confirmed the expression of VCAM-1 receptors in the inflamed muscle

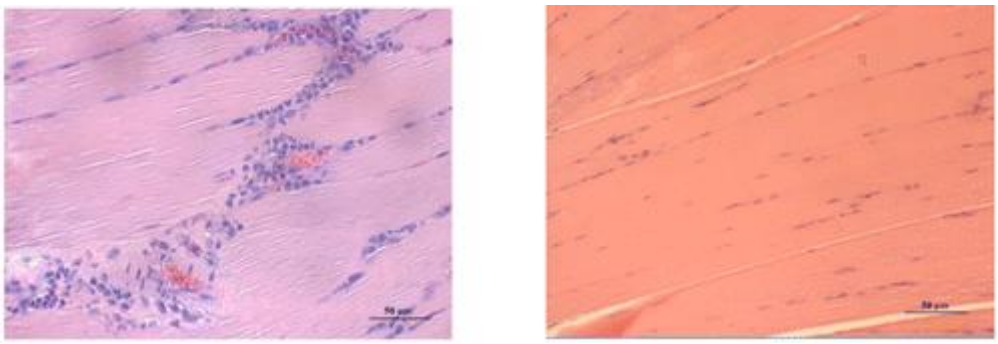

Figure 3. Histological slices stained with hematoxylin–eosin of inflamed (left) and healthy (right) leg skeletal muscle.

Forty-eight hours after the induction of inflammation, the paramagnetic micelles (containing the targeting or the scrambled peptide) were injected intravenously in the tail vein at a Gd dose of 55.0 µmol/kg bw. Then, the animals (n = 6) were scanned by MRI (at 1 T) over a period of 24 h post-injection. A T_1 contrast enhancement around 45% was observed in the inflamed region 4 h post-injection (Figure 4).

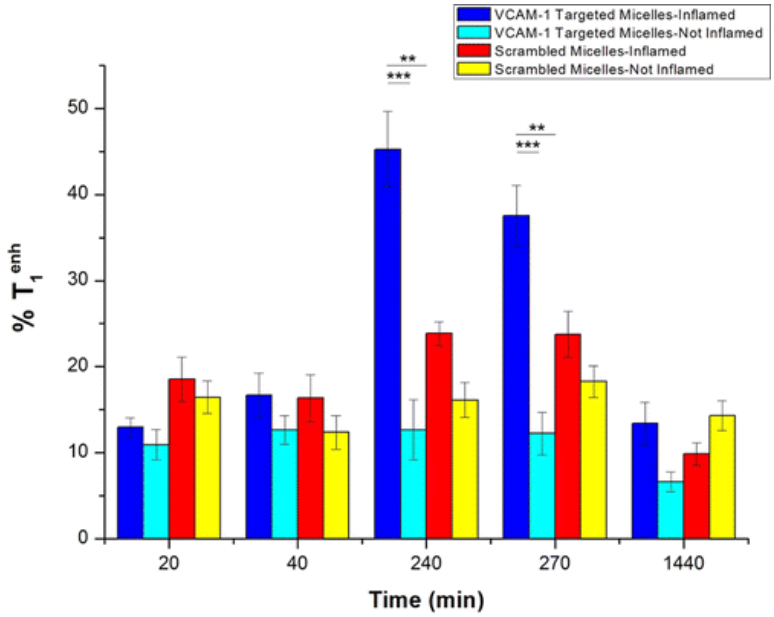

Figure 4. MRI T1 contrast enhancement at 1 T measured after intravenous injection of paramagnetic micelles. Blue bars refer to the VCAM-1 targeted micelles on an inflamed leg, while red bars refer to the control experiment (scrambled peptide) on an inflamed leg. Cyan and yellow bars refer to targeted and control micelles on healthy legs, respectively (*** $p < 0.01$–** $p < 0.05$). Error bars represent SE (standard error) of the mean (n = 6).

The contrast measured in the inflamed leg was ca. 5-fold higher than the enhancement detected in the contralateral healthy leg, and 2-fold higher than the response measured upon administration of the control micelles functionalized with the scrambled peptide. The MR images reported in Figure 5 show that 4 h after the injection of the micelles, a hyperintense signal was visible in the inflamed leg (red circle), while no brightening was detected in the control experiment.

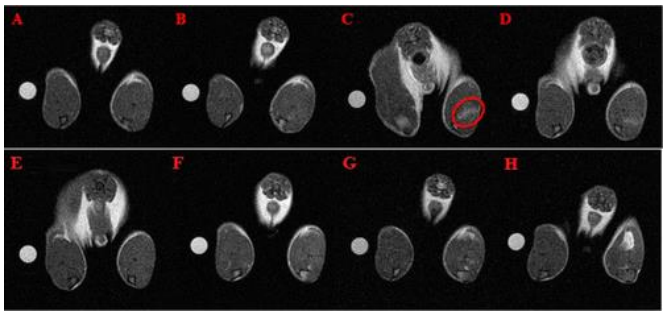

Figure 5. Axial T1w MR images of the legs of C57BL/6J mice acquired pre (A,E), 40 min (B,F), 4 h (C,G), and 24 h (D,H) after the injection of micelles targeting VCAM-1 receptors (top row) or micelles loaded with the scrambled peptide (bottom row). LPS was injected in the right leg muscle. The red oval highlights the inflamed area detected with the targeted agent.

Besides the inflamed legs, a significant MRI contrast was also detected in the liver, spleen, and kidneys even 24 h after the injection of the micelles. The accumulation of the MRI agent in the legs was confirmed by ICP-MS analysis (Figure 6), which showed that the amount of metal ion in the inflamed muscles after the injection of the VCAM-1-targeted micelles was ca. 40% higher than the amount found in the diseased tissue after the injection of the control micelles loaded with the scrambled peptide and ca. 3-fold higher with respect to the Gd found in the healthy muscles regardless of the type of micelles injected.

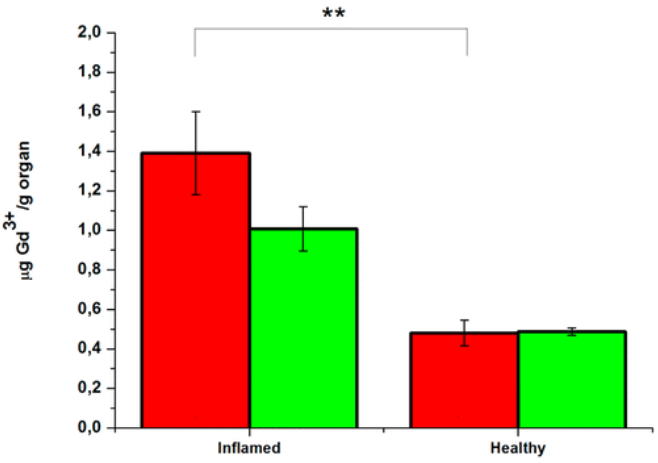

Figure 6. Amount of Gd (normalized to the organ weight) measured in legs excised 4 h after the intravenous injection of paramagnetic micelles. Red, VCAM-1 targeted agent; green, control agent. Error bars refer to the SE of the mean (n = 6). (** $p < 0.05$).

Discussion

The primary motivation of this work was to develop an improved MRI T_1 Gd-based agent for targeting the intravascular VCAM-1 receptors, as a biomarker of endothelium activated by inflammation. The most straightforward approach to increase the detection sensitivity of MRI contrast is to load a high number of paramagnetic centers to a nanocarrier suitably designed to bind the desired target. The loading of the agent to the carrier invariably slows down the rotational motion of the paramagnetic complex, and consequently, it can markedly affect the magnetic field dependence of the relaxivity of the system. In particular, an increase in sensitivity occurs in a field range between 0.2 and 1.5 T, mainly depending on the exchange rate of the Gd-bound water protons and the electronic relaxation times of the paramagnetic center. Though several hints to design Gd(III) complexes with high relaxivity at fields exceeding 1.5 T have been already proposed (**33,34**), the simplest approach to increase the sensitivity relies on: (a) the use of thermodynamically and kinetically stable Gd-agents (possibly already validated *in vivo)*, (b) their loading into a biocompatible targeted carrier, and (c) the detection of the contrast on a MR scanner operating at a magnetic field chosen to maximize the relaxometric properties of the agent. Steps a and b are somehow related because the choice of the Gd-agent may be influenced by the physicochemical properties of the carrier. In this work, we decided to use phospholipid-based micelles for their high biocompatibility and favourable pharmacokinetic properties. The easiest way to load a MRI agent in these soft self-aggregates is through the design of a metal complex with a phospholipid-like structure, i.e., characterized by the presence of a lipophilic portion conjugated to the hydrophilic coordination cage hosting the paramagnetic metal. The complex Gd-DOTAMA(C_{18})$_2$ perfectly meets this requirement, and it was already successfully used in many literature reports, mostly incorporated in bilayered membranes of liposomes (**35-37**). Though the presence of an amidic coordinating group does not guarantee an optimal exchange rate of the water molecule bound to the metal, the thermodynamic and kinetic stabilities of the complex, as well as the efficiency and stability of the loading to lipid-based particles, are very good, thus making this agent an excellent option for the preparation of MRI detectable nanocarriers. In addition to the MRI probe, micelles were also loaded with a newly synthesized phospholipid-based peptide for targeting VCAM-1 receptors. The peptide, selected by phage display by others (**23**), was prepared by solid phase synthesis and then conjugated at the polar distal end of the phospholipid DSPE-PEG2000. In parallel, a nontargeted scrambled version of the peptide was synthesized, conjugated with the same phospholipid, and used to prepare paramagnetic micelles acting as control for the *in vivo* imaging experiments. The shape of the NMRD profile measured for the paramagnetic micelles (Figure 1, left)

was fully consistent with the occurrence of a restricted rotational motion for the Gd-complex embedded in the nanoparticle. The relaxivity reached a maximum value of 36.4 $s^{-1}mM_{Gd}^{-1}$ at the Larmor frequency of 30 MHz (and 25 °C), i.e., about 5-fold larger than the corresponding value measured for the monomeric agent reported in ref 23, and 2.5 times higher than the r_1 value reported for the nanosized agent based on the tobacco mosaic virus (**24**). In the latter system, a number of ca. 1200 Gd-complexes per particle was estimated, which led to a particle relaxivity of 17520 $s^{-1}mM^{-1}$. We made a rough calculation of the number of Gd-DOTAMA(C_{18})$_2$ units loaded into a single micelle on the basis of the area occupied by the two main components (DSPE-PEG2000 and Gd-DOTAMA(C_{18})$_2$; see Experimental Procedures). Considering a molecular surface area of 0.45 nm^2 and 0.8 nm^2 for DSPE-PEG2000 and Gd-DOTAMA(C_{18})$_2$, respectively (36,38), and using the average particle radius obtained by DLS measurements (10 nm), ca. 850 Gd-complexes resulted in being loaded in a single micelle, which corresponds to a particle relaxivity of about 30000 $s^{-1}mM^{-1}$, with an improvement of ca. 70% with respect to the agent reported in ref 24. Interestingly, the temperature dependence of water ^{17}O-R_{2p} (Figure 1, right) clearly indicated the presence of two paramagnetic species in the micelle suspension, characterized by very different water exchange rates. This behaviour, which was observed in a series of *trans*-bisamide derivatives of Gd-DOTA (**28**) and more recently even for Gd-HPDO3A (**29**), can be interpreted in terms of the presence of comparable amounts of the two conformational isomers of Ln-DOTA complexes with capped square antiprismatic (SAP) and capped twisted square antiprismatic (TSAP) structures (**39**). It has been clearly demonstrated that the two isomeric configurations display different exchange rates for the water molecule occupying the capped position, with the TSAP isomer being the structure with the faster exchange (**40, 41**). The simultaneous analysis of NMRD and ^{17}O-R_{2p} data for the paramagnetic micelles investigated in this work allowed the estimation of the residence lifetime (τ_M) for the Gd-bound water molecule in the two species that resulted in 380 and 1.5 ns for SAP and TSAP isomers, respectively (Table 1). Therefore, it is straightforward to assign the species with the larger τ_M value to the SAP conformation and the one with the faster exchange to the TSAP structure. The ratio between the τ_M values for the two diastereoisomers (about 310) lies in the middle of the range reported in the literature for Gd-DOTA bisamide complexes (100–700) (**28**). However, likely due to the electroneutrality of Gd-DOTAMA(C_{18})$_2$ complex, the exchange lifetime for both the isomers incorporated in the micelles is almost an order of magnitude lower than the mono positively charged bisamide derivatives. Because of the water insolubility of Gd-DOTAMA(C_{18})$_2$, it was not possible to assess if the distribution (21.8% SAP and 78.2% TSAP as obtained from the relaxometric analysis) and water dynamics of the two isomers are influenced by the inclusion of the amphiphilic complex

in the nanoparticle. Actually, effects of the characteristics of the local microenvironment on the isomer distribution in DOTA-amide complexes have been already reported (**42**). It is interesting to note that, unlike other macrocyclic complexes, the SAP/TSAP ratio for Gd-DOTAMA(C_{18})$_2$ in micelles is lower than 1. This finding is very important because the occurrence of a short water residence lifetime allows the attainment of high relaxivities especially when (as in this case) the Gd-complex experiences a slow rotational motion. The different water exchange regime for the two conformations likely accounts for the very similar r_1 values (at 0.5 T) measured at 25 °C (34.9 mM^{-1} s^{-1}) and 37 °C (35.3 $s^{-1}mM^{-1}$), respectively. The NMRD profile clearly identifies the range of magnetic field where the micelles display the best performance to generate MRI contrast and, on this basis, the *in vivo* testing was performed at 1 T (corresponding to a Larmor frequency of 42.5 MHz). The agent was validated *in vivo* on an inflammation model obtained upon intramuscular injection of LPS in mice legs. The effective onset of inflammation 48 h after LPS injection was confirmed histologically (Figure 3). The paramagnetic micelles were intravenously injected at a dose of 55.0 µmol Gd/kg bw, and the animals were monitored by MRI at different times (20 min, 40 min, 4, 4.5, and 24 h) post injection. The data shown in Figure 4 indicated that the micelles targeting VCAM-1 receptors yielded a maximum contrast enhancement (ca. 45%) 4 h post-injection. Such a contrast was ca. 5-fold higher than the response observed in the healthy contralateral leg, and ca. 2-fold higher than the contrast measured upon injection of the control micelles loaded with the scrambled peptide. Likely, the difference in the contrast observed between the diseased and the healthy leg after the injection of the control micelles (also observed in ref 23) can be ascribed to a nonspecific accumulation of the untargeted probe in the lesion. The different contrast enhancement measured *in vivo* was confirmed by the amount of Gd determined in the explanted muscles by ICP-MS. The data obtained (shown in Figure 6) paralleled the trend observed for the MRI contrast, thus highlighting the superior accumulation of the targeted agent in the inflamed region. However, the difference observed among the experimental groups in the ICP-MS analysis was smaller than MRI contrast (e.g., the 40% difference between the amount of Gd found in the inflamed muscles in targeted and control groups was not statistically significant). This is likely the result of the different contribution of the inflamed tissues in the two experiments. In fact, while it was possible to calculate the MRI contrast mostly in the inflamed area, the amount of Gd was determined over the whole explanted muscle, thus diluting the difference with the control group.

In conclusion, this work proposes a new highly sensitive MRI nanoagent for the *in vivo* visualization of inflammation through the targeting of the intravascular VCAM-1 receptors. The system derives by the self-assembling of natural phospholipids (or partly conjugated with a VCAM-1 directed peptide) and an amphiphilic Gd-complex, which forms micelles with a diameter of ca. 20 nm. The combination between the high relaxivity displayed by the single contrastophore and the high number of complexes loaded per micelle makes this agent suitable to overcome the sensitivity issue often associated with MR-molecular imaging experiments. However, the favourable property of this agent can be fully exploited only if it is imaged at a magnetic field tuned with the NMRD profile of the system (here 0.5–1.5 T). When injected *in vivo* in a mouse model of acute inflammation and monitored at 1 T, the agent performed very well allowing the detection of a contrast about 5-fold higher than that measured in the noninflamed tissue. We expect that the herein reported results will stimulate research to further assess and optimize the pharmacokinetic properties with the ultimate goal to develop a clinical-translatable MRI agent for diagnostic/theranostic protocols on inflammation-associated diseases.

References

1. Ryan, G. B., and Majno, G. (1977) Acute inflammation. A review. Am. J. Pathol. 86, 183−267.

2. Libby, P., Ridker, P. M., and Maseri, A. (2002) Inflammation and Atherosclerosis. Circulation 105, 1135−1143.

3. Grivennikov, S. I., Greten, F. R., and Karin, M. (2010) Immunity, Inflammation, and Cancer. Cell 140, 883−899.

4. Xanthos, D. N., and Sandkü hler, J. (2014) Neurogenic neuroinflammation: inflammatory CNS reactions in response to neuronal activity. Nat. Rev. Neurosci. 15, 43−53.

5. Gahmberg, C. G., Tolvanen, M., and Kotovuori, P. (1997) Leukocyte adhesion, Structure and function of human leukocyte P,- integrins and their cellular ligands. Eur. J. Biochem. 245, 215−232.

6. Carlos, T. M., and Harlan, J. M. (1994) Leukocyte-Endothelial Adhesion Molecules. Blood 7, 2068−2101.

7. Blake, G. J., and Ridker, P. M. (2002) Inflammatory bio-markers and cardiovascular risk prediction. J. Intern. Med. 252, 283−294.

8. Blake, G. J., and Ridker, P. M. (2001) Novel Clinical Markers of Vascular Wall Inflammation. Circ. Res. 89, 763−771.

9. Cook-Mills, J. M., Marchese, M. E., and Abdala-Valencia, H. (2011) Vascular Cell Adhesion Molecule-1 Expression and Signaling During Disease: Regulation by Reactive Oxygen Species and Antioxidants. Antioxid. Redox Signaling 15, 1607−1638.

10. Dean, D. C., Iademarco, M. F., Rosen, G. D., and Sheppard, A. M. (1993) The Integrin α4β1 and Its Counter Receptor VCAM-1 in Development and Immune Function. Am. Rev. Respir. Dis. 148, S43−S46.

11. Jacobs, A. H., Tavitian, B., and the INMIND consortium (2012) Noninvasive molecular imaging of neuroinflammation. J. Cereb. Blood Flow Metab. 32, 1393−1415.

12. Deddens, L. H., van Tilborg, G. A., van der Toorn, A., van der Marel, K., Paulis, L. E., van Bloois, L., Storm, G., Strijkers, G. J., Mulder, W. J., de Vries, H. E., and Dijkhuizen, R. M. (2013) MRI of ICAM-1 Upregulation After Stroke:the Importance of Choosing the Appropriate Target-Specific Particulate Contrast Agent. Mol. Imaging Biol. 15, 411−422.

13. Baird, A. E., and Warach, S. (1998) Magnetic resonance imaging of acute stroke. J. Cereb. Blood Flow Metab. 18, 583−609.

14. Corti, R., and Fuster, V. (2011) Imaging of atherosclerosis: magnetic resonance imaging. Eur. Heart J. 32, 1709−1719b.

15. Caravan, P. (2006) Strategies for increasing the sensitivity of gadolinium based MRI contrast agents. Chem. Soc. Rev. 35, 512−523.

16. Beckmann, N., Cannet, C., Babin, A. L., Ble, F. X., Zurbruegg, S.,´ Kneuer, R., and Dousset, V. (2009) In vivo visualization of macrophage infiltration and activity in inflammation using magneticresonance imaging. Wiley Interdiscip. Rev. Nanomed. Nanobiotechnol. 1, 272−298.

17. Stoll, G., Basse-Lü sebrink, T., Weise, G., and Jakob, P. (2012) Visualization of inflammation using (19)F-magnetic resonance imaging and perfluorocarbons. Wiley Interdiscip. Rev. Nanomed. Nanobiotechnol. 4, 438−447.

18. Chacko, A. M., Hood, E. D., Zern, B. J., and Muzykantov, V. R. (2011) Targeted Nanocarriers for Imaging and Therapy of Vascular Inflammation. Curr. Opin. Colloid Interface Sci. 16, 215−227.

19. Burtea, C., Ballet, S., Laurent, S., Rousseaux, O., Dencausse, A., Gonzalez, W., Port, M., Corot, C., Vander Elst, L., and Muller, R. N. (2012) Development of a magnetic resonance imaging protocol for the characterization of atherosclerotic plaque by using vascular cell adhesion molecule-1 and apoptosis-targeted ultrasmall superparamagnetic iron oxide derivatives. Arterioscler., Thromb., Vasc. Biol. 32, 36− 48.

20. Michalska, M., Machtoub, L., Manthey, H. D., Bauer, E., Herold, V., Krohne, G., Lykowsky, G., Hildenbrand, M., Kampf, T., Jakob, P., Zernecke, A., and Bauer, W. R. (2012) Visualization of vascular inflammation in the atherosclerotic mouse by ultrasmall superparamagnetic iron oxide vascular cell adhesion molecule-1-specific nanoparticles. Arterioscler., Thromb., Vasc. Biol. 32, 2350−2357.

21. Gauberti, M., Montagne, A., Marcos-Contreras, O. A., Le Behot,´ A., Maubert, E., and Vivien, D. (2013) Ultra-sensitive molecular MRI of vascular cell adhesion molecule-1 reveals a dynamic inflammatory penumbra after strokes. Stroke 44, 1988−1996.

22. Patel, N., Duffy, B. A., Badar, A., Lythgoe, M. F., and Årstad, E. (2015) Bimodal Imaging of Inflammation with SPECT/CT and MRI Using Iodine-125 Labeled VCAM-1 Targeting Microparticle Conjugates. Bioconjugate Chem. 26, 1542−1549.

23. Burtea, C., Laurent, S., Port, M., Lancelot, E., Ballet, S., Rousseaux, O., Toubeau, G., Vander Elst, L., Corot, C., and Muller, R. N. (2009) Magnetic Resonance Molecular Imaging of Vascular Cell Adhesion Molecule-1 Expression in Inflammatory Lesions Using a Peptide-Vectorized Paramagnetic Imaging Probe. J. Med. Chem. 52, 4725−4742.

24. Bruckman, M. A., Jiang, K., Simpson, E. J., Randolph, L. N., Luyt, L. G., Yu, X., and Steinmetz, N. F. (2014) Dual-modal magnetic resonance and fluorescence imaging of atherosclerotic plaques in vivo using VCAM-1 targeted tobacco mosaic virus. Nano Lett. 14, 1551− 1558.

25. Al Faraja, A., Luciani, N., Kolosnjaj-Tabi, J., Mattar, E., Clement, O., Wilhelm, C., and Gazeau, F. 2013) Real-time high-resolution magnetic resonance tracking of macrophage subpopulations in a murine inflammation model: a pilot study with a commercially available cryogenic probe. Contrast Media Mol. Imaging 8, 193−203.

26. Pillai, R., Marinelli, E. R., Fan, H., Nanjappan, P., Song, B., von Wronski, M. A., Cherkaoui, S., Tardy, I., Pochon, S., Schneider, M., Nunn, A. D., and Swenson, R. E. (2010) A Phospholipid-PEG2000 Conjugate of a Vascular Endothelial Growth Factor Receptor 2 (VEGFR2)-Targeting Heterodimer Peptide for Contrast-Enhanced Ultrasound Imaging of Angiogenesis. Bioconjugate Chem. 21, 556−562.

27. Merbach, A. S., Helm, L, and Toth, E. (2013) The Chemistry of Contrast Agents in Medical Magnetic Resonance Imaging, 2nd ed., John Wiley and Sons, West Sussex, UK.

28. Zhang, S., Kovacs, Z., Burgess, S., Aime, S., Terreno, E., and Sherry, A. D. (2001) {DOTA-bis(amide)}lanthanide Complexes: NMR Evidence for Differences in Water-Molecule Exchange Rates for Coordination Isomers. Chem.−Eur. J. 7, 288−296.

29. Delli Castelli, D., Caligara, M. C., Botta, M., Terreno, E., and Aime, S. (2013) Combined high resolution NMR and 1H and 17O relaxometric study sheds light on the solution structure and dynamics of the lanthanide(III) complexes of HPDO3A. Inorg. Chem. 52, 7130− 7138.

30. Troughton, J. S., Greenfield, M. T., Greenwood, J. M., Dumas, S., Wiethoff, A. J., Wang, J., Spiller, M., McMurry, T. J., and Caravan, P. (2004) Synthesis and evaluation of a high relaxivity manganese(II)- based MRI contrast agent. Inorg. Chem. 43, 6313−6323.

31. Avedano, S., Botta, M., Haigh, J. S., Longo, D., and Woods, M. (2013) Coupling fast water exchange to slow molecular tumbling in Gd3+ chelates: why faster is not always better. Inorg. Chem. 52, 8436− 8450.

32. Webber, B. C., and Woods, M. (2014) The confluence of structure and dynamics in lanthanide(III) chelates: how dynamics help define structure in solution. Dalton Trans. 43, 251−258. (33) Caravan, P., Farrar, C. T., Frullano, L., and Uppal, R. (2009) Influence of molecular parameters and increasing magnetic field strength on relaxivity of gadolinium- and manganese-based T1 contrast agents. Contrast Media Mol. Imaging 4, 89−100.

34. Helm, L. (2010) Optimization of gadolinium-based MRI contrast agents for high magnetic-field applications. Future Med. Chem. 2, 385−396.

35. Cittadino, E., Ferraretto, M., Torres, E., Maiocchi, A., Crielaard, B. J., Lammers, T., Storm, G., Aime, S., and Terreno, E. (2012) MRI evaluation ofthe antitumor activity of paramagnetic liposomes loaded withprednisolone phosphate. Eur. J. Pharm. Sci. 45, 436−441.

36. Cittadino, E., Botta, M., Tei, L., Kielar, F., Stefania, R., Chiavazza, E., Aime, S., and Terreno, E. (2013) In Vivo Magnetic Resonance Imaging Detection of Paramagnetic Liposomes Loaded with Amphiphilic Gadolinium(III) Complexes: Impact of Molecular Structure on Relaxivity and Excretion Efficiency. ChemPlusChem 78, 712−722.
37. Filippi, M., Martinelli, J., Mulas, G., Ferraretto, M., Teirlinck, E., Botta, M., Tei, L., and Terreno, E. (2014) Dendrimersomes: a new vesicular nano-platform for MR-molecular imaging applications. Chem. Commun. 50, 3453−3456.
38. Qin, S. S., Yu, Z. W., and Yu, Y. X. (2009) Structural Characterization on the Gel to Liquid-Crystal Phase Transition of Fully Hydrated DSPC and DSPE Bilayers. J. Phys. Chem. B 113, 8114− 8123.
39. Benetollo, F., Bombieri, G., Calabi, L., Aime, S., and Botta, M. (2003) Structural variations across the lanthanide series of macrocyclic DOTA complexes: insights into the design of contrast agents for magnetic resonance imaging. Inorg. Chem. 42, 148−157.
40. Aime, S., Barge, A., Bruce, J. I., Botta, M., Howard, J. A. K., Moloney, J. M., Parker, D., De Sousa, A. S., and Woods, M. (1999) NMR, Relaxometric, and Structural Studies of the Hydration and Exchange Dynamics of Cationic Lanthanide Complexes of Macrocyclic Tetraamide Ligands. J. Am. Chem. Soc. 121, 5762−5771.
41. Dunand, F. A., Aime, S., and Merbach, A. E. (2000) First 17O NMR Observation of Coordinated Water on Both Isomers of [Eu(DOTAM)(H2O)]3+: A Direct Access to Water Exchange and its Role in the Isomerization. J. Am. Chem. Soc. 122, 1506−1512.
42. Miller, K. J., Saherwala, A. A., Webber, B. C., Wu, Y., Sherry, A. D., and Woods, M. (2010) The Population of SAP and TSAP Isomers in Cyclen-Based Lanthanide(III) Chelates Is Substantially Affected by Solvent. Inorg. Chem. 49, 8662−8664.
43. Anelli, P. L., Lattuada, L., Lorusso, V., Schneider, M., Tournier, H., and Uggeri, F. (2001) Mixed micelles containing lipophilic gadolinium complexes as MRA contrast agents. MAGMA 12, 114−20.
44. Vaccaro, M., Mangiapia, G., Paduano, L., Gianolio, E., Accardo, A., Tesauro, D., and Morelli, G. (2007) Structural and relaxometric characterization of peptide aggregates containing gadolinium complexes as potential selective contrast agents in MRI. ChemPhysChem 8, 2526−38.

2.2- MRI visualization of neuroinflammation

Based on:

Garello F., **Pagoto A**., Arena F., Buffo A., Blasi F., Alberti D, Terreno E.
MRI visualization of neuroinflammation using VCAM-1 targeted paramagnetic micelles, Nanomedicine: NMB - 2017

Introduction

Neuroinflammation is an active multifaceted adaptive process. It has been detected in infectious brain diseases as well as following central nervous system (CNS) traumatic injury, and, more recently, in patients affected by various neurodegenerative pathologies (**1-3**). The main features of this dynamic process are: (i) changes in the vasculature, (ii) activation of resident immune competent cells, (iii) infiltration of blood circulating immune cells (neutrophils, macrophages, lymphocytes), and (iv) cytokine production (**4,5**). This orchestrated machinery would have the purpose of limiting the extent of the disease, clearing tissue damage and supporting repair and regeneration; but at the same time, it could lead to the boosting and perpetuation of inflammation (**6-8**). The precise mechanisms regulating and driving this frail equilibrium are not completely clarified yet. Indeed, the close relationship between neuroinflammation and the onset and development of many neurodegenerative diseases is becoming more and more undeniable (**9-15**) Since these disorders are affecting millions of people worldwide and their prevalence is expected to raise in the next decades (**5**), the need for specialized non-invasive imaging techniques is increasing to better clarify the role and the spatio-temporal correlation between inflammation and degeneration. So far, in clinics, most of the available imaging techniques allowed for the diagnosis of neurodegenerative diseases only at later stage of progression, hence limiting the treatment outcome (**16–18**). Various targeted Positron Emission Tomography (PET) tracers have been designed and tested in clinics to detect neurodegeneration or neuroinflammation (**19-21**) However, despite the great sensitivity of PET imaging and the possibility to obtain quantitative information, these compounds, due to their lipophilic nature, display a considerable non-specific binding, resulting in remarkable signal overlap with control patients (**22-25**). In addition, PET imaging is characterized by high costs, reduced half-life time of the tracers and limited follow up of the patients due to the invasiveness of the technique. A valuable alternative to PET is Magnetic Resonance Imaging (MRI), which with its outstanding spatial resolution, moderate cost-effectiveness, relatively slow kinetics of probes and lack of radiation exposure, can be considered a technique of choice in neuroimaging. The diagnosis of different neurological disorders, indeed, can be performed through the MR assessment of volume changes in specific brain regions or the MR detection of distinct pathological hallmarks (**26-31**). However, routine structural neuroimaging evaluations are normally based on the observation of late features in the progression of the disease. Therefore, the development of new MRI approaches for early and specific recognition of neurological diseases at the prodromal stages would be of crucial importance. In light of the low sensitivity of MRI and of the difficulties encountered by the mostly hydrophilic commercialy available paramagnetic probes in overcoming

an intact blood brain barrier (BBB), a suitable strategy to obtain a considerable signal is the development of molecules targeting the neuroinflammation-mediated changes in the vasculature. More in details, in the event of neuroinflammation, infiltration of immune cells from the bloodstream into CNS parenchyma occurs through a sequential and coordinated process involving tethering, rolling, adhesion and transmigration of leucocytes across the BBB (**32,33**). Each step involves interaction of BBB endothelial cells and leukocytes via endothelial expression of Cell Adhesion Molecules (CAMs), among which vascular CAM-1 (VCAM-1) is one of the most investigated. VCAM-1 is not constitutively expressed on the endothelium but is up-regulated upon endothelial activation, thus being an attractive target of early cerebral inflammation, easily accessible to blood borne contrast agents (**34-36**). Superparamagnetic iron oxide microparticles (MPIO) were already conjugated to antibodies (**37,38**) or peptidic vectors (**39**) for targeting VCAM-1 receptors to generate highly specific hypointense contrast effects associated with the overexpression of the target in animal models where inflammation is relevant. However, so far, Gd-containing nanosystems targeting the over expression of VCAM-1 have not been tested yet in the visualization of CNS inflammation (**40**). Indeed, the use of positive contrast agents is advisable to unequivocally locate the inflamed region, avoiding signal misunderstandings due to the presence of hemorrhages, air or abnormal mineral substances accumulation (**41**). In addition, as MPIO are avidly taken up from the immune system cells, the use of stealthier particles is desirable to increase the blood half-life time of the system and increase the targeting selectivity. In the herein reported work, VCAM-1 targeted Gd-based paramagnetic micelles, developed by our group and already successfully validated on a model of peripheral inflammation (**42**) were tested in a murine model of acute neuroinflammation to investigate their potential application in the early detection of neurodegenerative processes.

Experimental procedures

Animal care and use

C57BL/6J female mice (8-12 weeks old) were obtained from the animal facility at the Molecular Biotechnology Center of the University of Torino. The animal study was approved by the Italian Ministry of Health; the procedures followed were in accordance with institutional guidelines and ensured the humane care of the animals. Anesthesia was provided by 1%-2% isoflurane inhalation or by intramuscular injection of a combination of 20 mg/kg tiletamine/zolazepam (Zoletil 100; Virbac, Milan, Italy) and 5 mg/kg xylazine (Rompun; Bayer, Milan, Italy)

Micelles preparation and characterization

The procedure was described in Chapter 2.1.

Estimation of VCAM-1 receptor expression

First, the expression of VCAM-1 receptor in the bEnd.3 cell line before and after activation with Tumor Necrosis Factor alpha (TNF-alpha) was investigated by fluorescence-activated cell sorting (FACS) analysis. To this purpose, bEnd.3 cells were cultured in complete Dulbecco's Modified Eagle's Medium (DMEM) until confluence was reached and then were either treated for 4 hours with TNF-alpha (50 ng/mL) or left in complete growth medium. Subsequently, cells were detached with Versene (EDTA) 0.02%, divided in different aliquots ($0.2x10^6$ cells/tube) and resuspended in 100 µL of Phosphate Buffered Saline (PBS) enriched with 0.1% Bovine Serum Albumin (PBS-BSA). Incubation with FITC conjugated anti VCAM-1 antibody was carried out for 1 h in ice. Mouse IgG1-FITC isotype was used as control. Cells were rinsed in PBS-BSA to remove unbound material and finally resuspended at a concentration of $0.6x10^6$ cells/mL in PBS-BSA. The presence of VCAM-1 receptor was investigated on a Flow Cytometer (Becton Dickinson, FACS Calibur). To determine the mean number of VCAM-1 receptors/cell, the same experiment was repeated without BSA in order to avoid interactions with serum proteins. To this end, after FACS analysis, cells were sonicated in ice (20 W) for 30 s. The protein concentration was then measured spectrophotometrically (6715 UV/Vis Spectrophotometer, Jenway) in each sample using the commercial Bradford assay (Bio-rad Protein Assay, Hercules, CA, USA). Since the number of cells is proportional to the protein concentration, this value was converted into the corresponding cell number (N_{cells}) using a dedicated calibration curve. Then the fluorescence of each sample was measured in a solution of Triton X-100 0.1% (v/v) in PBS by spectrofluorimetry (Fluoromax-4-Horiba Scientific) using λ_{exc} of 492 nm and λ_{em} of 517 nm. The fluorescence value of cells incubated with the mouse isotype was considered as aspecific contribution and subtracted from the measured fluorescence intensity values. A calibration curve of standard FITC (fluorescence intensity vs. concentration) was used to correlate the normalized intensity values to the moles of FITC. Finally, the number of VCAM-1 receptors/bEnd.3 cell was estimated as follows:

$$\frac{VCAM1_{receptors}}{bEnd.3\ Cell} = [([FITC]/7)\ x\ N_A]/Ncells$$

where 7 is the number of FITC molecules/antibody, and N_A is the Avogadro constant.

In vitro assays

An in vitro assay was performed to evaluate the binding ability of targeted micelles to VCAM-1 receptors in brain endothelial cells. To achieve this goal, bEnd.3 cells were cultured until confluence in two different T175 flasks, then to one flask 50 ng/mL of TNF-alpha were added for 4 hours to induce VCAM-1 over-expression, whilst to the other flask fresh complete growth medium was added. Cells were then detached with Versene (EDTA) from both flasks and divided into three aliquots. The first aliquot was kept as control, the second and third ones were incubated with either VCAM-1 targeted micelles or scrambled micelles at 2 mM Gd(III) concentration. Incubation was performed at 4°C for 30 minutes in order to allow receptor binding and minimize micelle uptake. Subsequently, cells were thoroughly washed, resuspended in 50 µL of PBS, transferred into glass capillaries and centrifuged to obtain cell pellets. The capillaries were then inserted into an agar phantom in order to mimic tissues and imaged at 7.0 T with a NMR Bruker Avance 300. T_{1w} Multi Slice Multi Echo MSME (Echo Time (TE)/ Repetition Time(TR)/ Number of Averages(NAV) 3.68/200/12, Matrix 128x128) and T_{2w} RARE (TE/TR/NAV/Rare Factor(RF) 3.68/200/12/32, Matrix 128x128) sequences were acquired. T_1 measurement of the cell phantom was performed varying the repetition time from 50 to 8000 ms (TE/TR/NR 3.68/50-8000/10, Matrix 128x128). The T_1 of each sample was then calculated by means of ROI selection directly on the acquired images. The longitudinal relaxation values ($R_1 = 1/T_1$) were also calculated. At the end of the acquisition, the samples were recollected, suspended in 200 µL of PBS and sonicated at 20 W for 30 s in ice. Then, the amount of proteins was measured with the Bradford assay and the related number of cells estimated as reported above (paragraph 2.4). To quantify the amount of gadolinium in each sample, cell extracts were digested with concentrated HNO_3 (70%, 1 mL) under microwave heating (Milestone MicroSYNTH Microwave labstation), recollected in ultrapure milli-Q water and analyzed by inductively coupled plasma mass spectrometry (ICP-MS; element-2; Thermo-Finnigan, Rodano (MI), Italy). The mean Gd(III) content in each cell was then calculated as mol of Gd/cell. Moreover, the normalized relaxivity r_1 of each sample s was calculated as:

$$r_1^s = \frac{R_1^s - 0.40}{[Gd]}$$

To visualize the binding of the micelles to VCAM-1 receptors expressed by bEnd.3 cells, the cells were plated in ibidi® µ-slide wells ($1x10^4$ cells/well) and cultured until confluence. Then, in 4 wells cells were treated with TNF-alpha to induce VCAM-1 receptor over-expression, whereas in the other

four wells complete growth medium was added. After 4 hours, cells were washed twice with PBS and incubated with VCAM-1 targeted micelles (0.12 mM Gd) for 30 min at 4°C. At the end of incubation, cells were thoroughly washed with PBS, fixed in 4% formalin (15 min, RT) and stained with Hoechst to visualize nuclei. Confocal microscopy images were acquired with a Leica SP5 confocal microscope ($laser_1$ excitation 405 nm, acquisition window 415–480 nm, $laser_2$ excitation 561 nm, acquisition window 580–675 nm, to visualize Hoechst and rhodamine dyes, respectively).

Half-life time of VCAM-1 targeted micelles

The blood half-life time of VCAM-1 targeted micelles was investigated in healthy C57BL/6J female mice (n = 3). Micelles were administered through tail vein injection at 0.05 mmolGd/kg body weight. At different time points (5, 15, 30 min, 1, 2, 4 and 24 h) post injection, a micro aliquot of blood was collected from the tail vein. 20 µL of Heparin (500 UI/mL) were added to each sample to avoid coagulation. The volume of blood collected at each time was quantified, then the samples were digested with concentrated HNO3 (70%, 1 mL) under microwave heating, recollected in ultrapure milli-Q water and analyzed by ICP-MS to measure Gd(III) content at each time point. Data obtained, displayed as millimolar concentration vs. time post injection, were fitted with a mono-exponential decay curve and the half-life time was calculated.

LPS-induced neuroinflammation model

Acute neuroinflammatory response was induced in the right striatum of 8 to 12-week-old C57BL/6J female mice (weight 18±3 g). The animals were divided into 3 different groups: neuroinflamed mice administered with VCAM-1 targeted micelles (n=8), neuroinflamed mice administered with untargeted scrambled micelles (n=4), and neuroinflamed mice administered with the clinically approved contrast agent MultiHance® (n=4). One healthy mouse and one PBS intra-striatally injected mouse were used as supplementary controls. To obtain the model, mice were anesthetized, positioned in a stereotaxic apparatus (Stoelting) and the skull was exposed. The brain of the animal was then exposed via a hole, which was drilled through the skull. A glass capillary was inserted into the right striatum using the following stereotaxic coordinates from bregma: + 0.1 mm antero-posterior, − 2.1 mm mediolateral, − 2.6 mm dorsoventral. 1 µL of lipopolysaccharide (LPS) (E. coli 026:B6, Sigma-Aldrich) in sterile phosphate buffered saline PBS at a concentration of 5 µg/µl was then infused with a pneumatic pressure injection apparatus (Picospritzer II, General Valve Corporation) over 5 min followed by a 2 minutes rest period to allow the solution to diffuse into the brain prior to the removal of the capillary. For the saline control mouse, the same surgery described

above was performed, but the vehicle only (1 µL of PBS) was injected intra-striatally. The presence of inflammation was investigated ex-vivo by hematoxylin and eosin staining; VCAM-1 over-expression in the inflamed striatum was assessed by confocal microscopy following staining with FITC anti VCAM-1 antibody and Hoechst.

In vivo MRI

All the MR images were acquired on a Bruker Icon (1 T) equipped with a brain surface coil. Animals were recruited 24 h post LPS injection. MRI acquisition was performed under 1% isoflurane anesthesia. Animals were scanned before and 20 min, 4 h, 24 h, 48 h post injection of VCAM-1 targeted paramagnetic micelles or micelles decorated with the scrambled peptide. T2-weighted MRI images were obtained using a RARE sequence protocol (TR/TE/NAV = 2500/26.7/12). T1-weighted MRI images were acquired using a FLASH sequence (TR/TE/NAV = 75/5.8/18, field of view (FOV) = 1.2 cm). To compare the contrast obtained with VCAM-1 targeted micelles with the one obtained after the administration of the clinically approved contrast agent MultiHance™, the agent was injected in the tail vein, 24 h after the induction of inflammation, at the concentration of 0.2 $mmol_{Gd}$/kg and the animals were imaged repeatedly for 30 min.

Image processing and analysis

Image analysis was performed using Bruker ParaVision 5.1 imaging software. Regions of interest (ROIs) were drawn over right (inflamed) and left (non-inflamed) striatum in the imaging plan and average signal intensity was measured. The % T_1 signal enhancement (% T_1-SE) over pre-images was calculated as follows:

$$\%T_1\ SE = \frac{SNR_t - SNR_0}{SNR_0} \times 100$$

Where

$$SNR_i = \frac{SI_i}{SD_i\ noise}$$

SNR stands for Signal to Noise Ratio, SI stands for Signal Intensity (with *i* = 0 or *t*), while 0 and *t* refer to the measurement carried out before and after the injection of the contrast agent, respectively.

Biodistribution of VCAM-1 targeted micelles

Micelle homing to the main excretory organs, liver, kidneys and spleen, was followed by MRI at different time points after the administration of VCAM-1 targeted micelles (*n* = 6). 24 h post injection the animals were sacrificed and the liver, spleen, kidneys, lungs, left and right cerebral hemispheres were excised, weighted and digested in concentrated nitric acid (70%) under microwave heating, recollected in ultrapure milli-Q water and analyzed by ICP-MS to measure Gd content. The amount of Gd (mg_{Gd}/g_{organ}) was calculated. Moreover, an estimation of the percentage of residual Gd in each organ according to the administered dose was evaluated in all the excised organs as follows:

$$\%Gd = \frac{mol\ Gd_{g\ organ} \times g\ organ}{mol\ Gd\ administered} \times 100$$

Ex-vivo studies

To investigate the presence of VCAM-1 targeted micelles in the inflamed brain regions, 24 hours post administration of the nanosystem the animals (*n*=2) were sacrificed following MRI acquisition and the brain was extracted and cryopreserved at -80°C until cryostat sectioning. Slices (20 µm of thickness) were cut using a Leica CM 1950 cryostat and fixed in absolute ethanol for 5 min. Then, slices were rinsed with phosphate-buffered saline (PBS) and nuclei were stained with Hoechst ($8x10^{-5}$ mg/mL, 10 min incubation). After a fast washing in purified water, slices were mounted using ProLong® Gold Antifade Mountant (TermoFisher Scientific, Waltham, Massachusetts, USA). To visualize blood vessels, CD-31 was stained, whereas to visualize microglia/peripheral macrophages, anti F4/80 antibody was used. To this purpose following fixation in ethanol, slices were washed in PBS and then blocking with 10% goat serum was performed for 1 h at room temperature. Subsequently, the primary antibody was added to the slices in 10% goat serum and left overnight at 4°C (anti CD31 1:200 dilution, anti F4/80 1:50 dilution). The day after, the slices were rinsed in PBS and staining with the secondary antibody (1:500) was carried out for 1 hour at room temperature. Three washings were performed to remove unbound material, and then nuclei were stained with Hoechst ($8x10^{-5}$ mg/mL, 10 min incubation). After a fast washing in purified water, slices were mounted using ProLong®. All the slices were imaged by confocal microscopy, magnification 40x, laser excitation 405, 488, 561 nm to detect Hoechst, Alexa Fluor 488 or Rhodamine, respectively.

Statistical analysis

All data were presented as mean values ± Standard Error of mean (SE). Significant differences among experimental conditions were identified by applying the one-way ANOVA test, assuming statistical significance at $P < 0.05$.

Results

Micelle preparation and characterization

VCAM-1 targeted paramagnetic micelles were prepared by the lipid thin film hydration method. The mean size of the obtained nanosystem, checked by DLS, was 17 ± 2 nm with a PDI value of 0.2 ± 0.1 (13 replicates). The longitudinal relaxivity (r_1) measured at 1 T and 37 °C was 35.0 $s^{-1}mM_{Gd}^{-1}$. Micelles bearing the scrambled version of the targeting peptide did not differ significantly in size and relaxivity in comparison to the VCAM-1 directed nanosystem.

Estimation of VCAM-1 receptor expression

In order to investigate the BBB targeting of the developed micelles, the murine brain endothelial cell line bEnd.3 was chosen as *in vitro* model. Although these cells are reported to constitutively express VCAM-1 receptor below passage 30, stimulation with TNF-alpha further increases the receptor expression. Flow cytometry was employed to investigate the presence of the surface receptor before and 4 h after incubation with TNF-alpha. The analysis of cell samples acquired by fluorescence-activated cell sorting (FACS) after incubation with the FITC anti VCAM-1 antibody showed a remarkable enhancement in VCAM-1 expression after treatment with TNF-alpha. The mean number of VCAM-1 receptors/cell was determined by spectrofluorimetry. More in details, before and after treatment with TNF-alpha, the cells were incubated with FITC-tagged anti VCAM-1 antibody to label the receptor. Subsequently, the cells were washed and sonicated in order to measure for each sample the mg of proteins, correlated to the number of cells, and the fluorescence intensity, correlated to the number of receptors. The results obtained displayed a four-fold increase in VCAM-1 expression after treatment with TNF-alpha (Figure 1), thus validating the use of such brain endothelial cells as *in vitro* model to assess the potential interaction between the receptor and the targeted nanosystem.

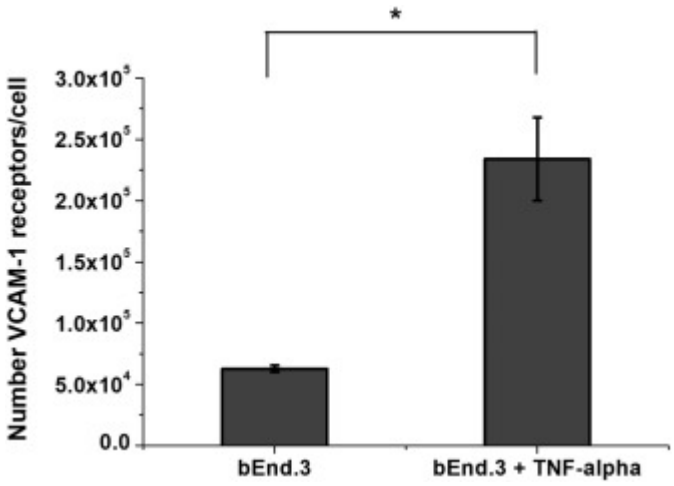

Figure 1. Mean number of VCAM-1 receptors/bEnd.3 cell before and after stimulation with TNF-alpha. The number of cells was estimated with the Bradford assay, while FITC concentration was determined by spectrofluorimetry (* $P < 0.05$). Error bars represent SE of the mean.

In vitro targeting assays

The affinity of targeted and non-targeted micelles towards VCAM-1 receptors was investigated *in vitro* using bEnd.3 cells. The whole experiment was carried out at 4 °C in order to avoid the cell internalization of the nanosystem. Confocal microscopy images, taken 30 min after incubation with the targeted micelles, proved that the selected timeframe was sufficient to achieve a considerable cell membrane labelling. An overall enhancement in the red fluorescence from naïve to activated bEnd.3 cells was observed, suggesting the presence of an active membrane labelling process. To quantify the amount of receptor-bound nanosystem and the MRI signal obtained after incubation of cell samples with targeted or scrambled micelles, an additional experiment was performed. More in detail, cells were detached with EDTA before and after treatment with TNF-alpha; incubation with targeted or untargeted (*i.e.* conjugated with a scrambled peptide) micelles (total Gd(III) concentration 2 mM) was performed in suspension for 30 min at 4 °C. At the end of the incubation, cells were profusely washed to remove unbound micelles, and then centrifuged into glass capillaries to obtain a cell pellet. The pellet was imaged by MRI at 7.0 T and the T_1 of each sample was measured. Immediately after imaging, the cell pellets were recollected and sonicated to estimate the number of bEnd.3 cells using the Bradford assay and to quantify the amount of gadolinium by ICP-MS. The amount of Gd(III) found in activated cells incubated with targeted micelles was *ca.* 90% higher than cells incubated with scrambled micelles (1.5×10^{-15} *vs.* 7.9×10^{-16} mol_{Gd}/cell). A similar disparity was noticed between the amount of Gd(III) in activated and non-activated cells incubated with VCAM-1 targeted micelles (1.5×10^{-15} *vs.* 6.6×10^{-16} mol_{Gd}/cell, $P < 0.05$) (Figure 2A). No significant differences were found in non-activated cells incubated with VCAM-1 targeted or untargeted micelles. Interestingly, the

relaxivity values determined for the non-activated cells were slightly lower than the activated ones, and, for the latter, the relaxivity of the targeted micelles was higher than the untargeted nanosytem (Figure 2B). The combination between the amount of cell-bound Gd and the relaxivity value justifies the different MRI contrast observed in the pellets (Figure 2C), where the samples incubated with VCAM-1 targeted micelles displayed the higher contrast.

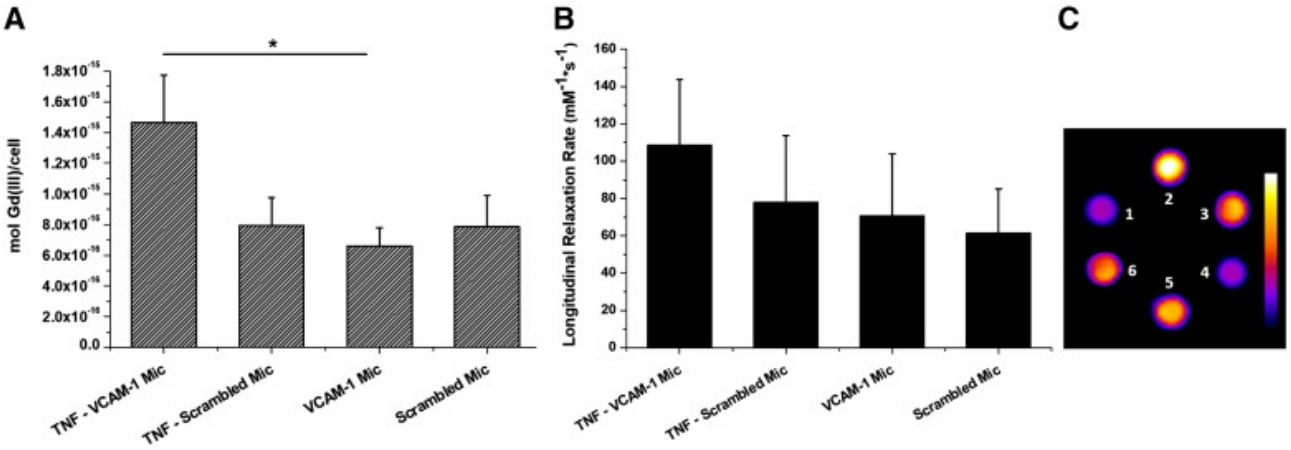

Figure 2. In vitro study on targeted or scrambled micelle binding affinity towards VCAM-1 in activated or non-activated brain endothelial cells. (A) Moles of Gd(III) per cell calculated using Bradford assay, to determine the number of cells, and ICP-MS, to measure Gd(III) concentration. (B) r_1 values of bEnd.3 cells measured at 7.0 T and normalized to ICP-MS values of Gd(III) concentration. (C) T_{1w} image (pseudo-colorized, originally in gray scale) of (1) activated bEnd.3 cells, (2) activated bEnd.3 cells incubated with VCAM-1 targeted micelles, (3) activated bEnd.3 cells incubated with scrambled micelles, (4) non-activated bEnd.3 cells, (5) non-activated bEnd.3 cells incubated with VCAM-1 targeted micelles and (6) non- activated bEnd.3 cells incubated with scrambled micelles. The incubation was carried out at 4 °C (30 min). Error bars represent SE of the mean (* $P < 0.05$).

In vivo blood half-life time of VCAM-1 targeted micelles

The blood half-life time of VCAM-1 targeted micelles was assessed in healthy mice ($n = 3$). The targeting nanosystem was administered by tail vein injection, and blood samples were collected at different time points, ranging from 5 min to 24 h, mixed with heparin to avoid coagulation, and quantified in terms of volume. Following digestion in concentrated nitric acid, the exact amount of Gd(III) at each time point was determined by ICP-MS. Data obtained were plotted and fitted with a mono-exponential decay curve, resulting in a mean half-life time of 376 ± 22 min ($R^2 = 0.99$, Figure 3).

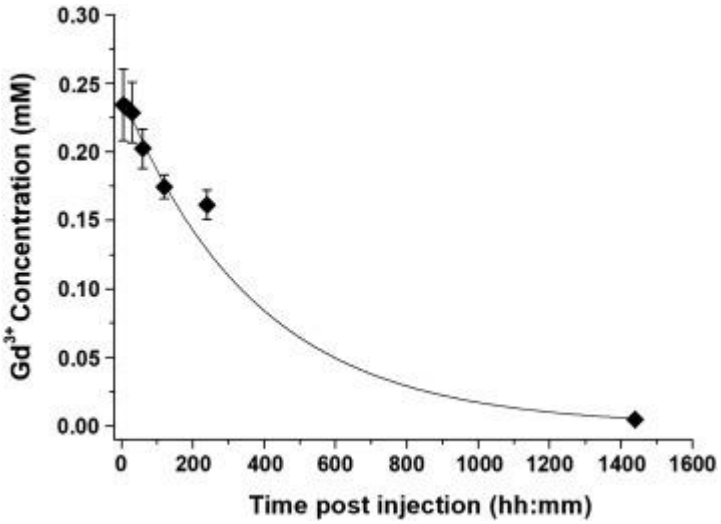

Figure 3. Mean half-life time of VCAM-1 targeted micelles assessed in healthy C57BL/6J female mice (n = 3) by ICP-MS analysis of blood samples collected at different time points post injection. Error bars represent SE of the mean.

In vivo MRI

On the basis of the promising *in vitro* results, the potential of VCAM-1 targeted micelles to bind VCAM-1 receptors at the blood brain barrier was investigated in a murine model of neuroinflammation. Acute neuroinflammatory response was induced in the right striatum by local injection of lipopolysaccharide (LPS). The presence of inflammation and the over-expression of VCAM-1 in the involved hemisphere were detectable already 24 h after surgery by *ex-vivo* histological studies. In the contra-lateral hemisphere, almost no hallmarks of inflammation were present. The animals were enrolled in the study 24 h after LPS injection, received intravenous administration of VCAM-1 targeted micelles (0.05 $mmol_{Gd}$/kg body weight) and were imaged at 1.0 T at 20 min, 4 h, 24 h and 48 h post injection (Figure 4) to monitor micelle homing to the site of inflammation.

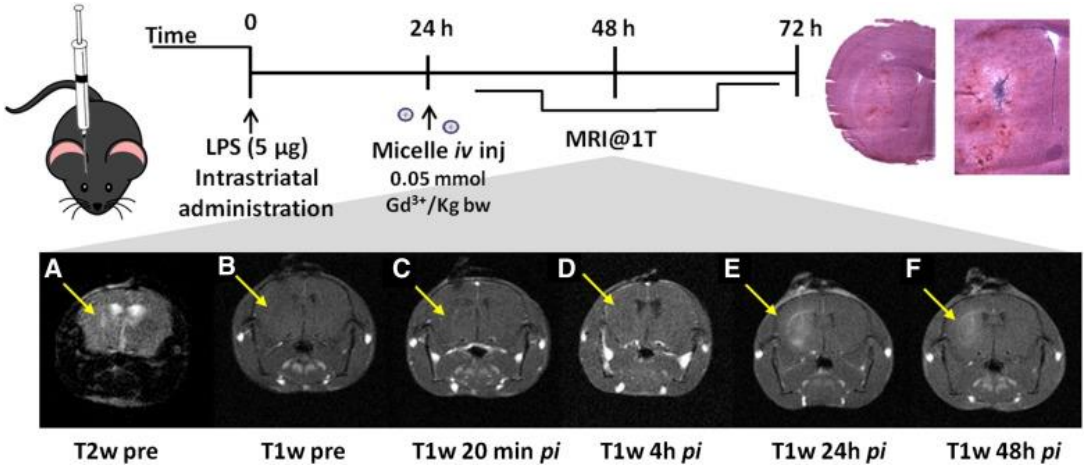

Figure 4. Top: Schematic representation of the experimental procedure: C57BL6/J mice were subjected to surgery to inject 5 µg of LPS intra-striatally in the right hemisphere; 24 h after surgery VCAM-1 targeted micelles were administered intravenously and the mice were imaged at 1 T: (A) T_{2w} image pre-injection, (B) T_{1w} image pre-injection, (C) T_{1w} image 20 min post injection, (D) T_{1w} image 4 h post injection, (E) T_{1w} image 24 h post injection, (F) T_{1w} image 48 h post injection. Yellow arrows indicate the inflamed region.

In T_{2w} anatomical images, a confined bright area in the inflamed hemisphere was occasionally observed, suggesting the presence of an edematous region. However, only after the injection of VCAM-1 targeted micelles were the real extension of the inflamed area clearly detectable and delineated (Figure 4E). In particular, the T_1 signal enhancement calculated over pre-images, reached a peak value 24 h post micelle injection, with a statistically significant difference between diseased and healthy hemispheres (39.3 ± 4.4 *vs.*4.1 ± 2.7%, respectively, $P < 0.001$, Figure 5).

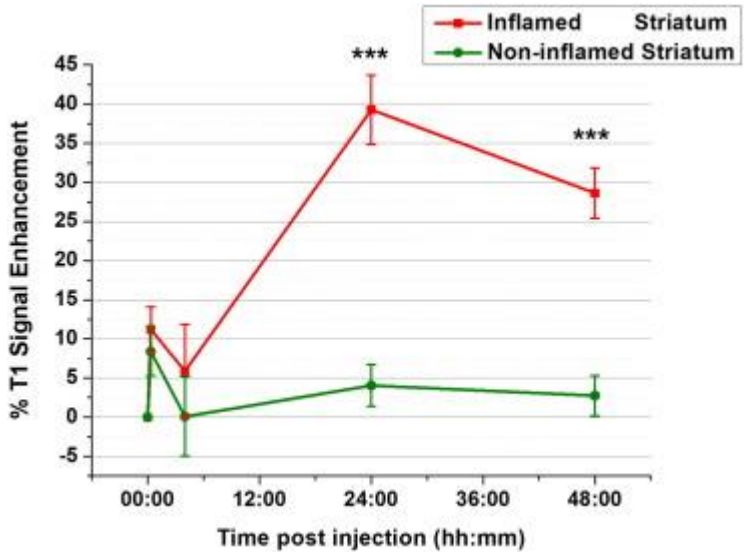

Figure 5. % T_1-SE calculated over pre-images in the striatum at different time points after the injection of VCAM-1 targeted micelles. The nanosystem was administered 24 h after the induction of inflammation (*** P < 0.001, n = 8). Error bars represent SE of the mean.

To ascertain the specificity of the administered nanosystem, a comparison with micelles bearing the untargeted scrambled peptide was conducted. The results obtained displayed a statistically significant difference in the % T_1-SE of the inflamed striatum between targeted and non-targeted micelles at 24 h *p.i.* (39.3 ± 4.4 *vs.* 18.9 ± 2.2%, respectively, ANOVA *P values* = 0.003, Figure 6). At the other time points, no statistically significant differences between the two nanosystems were detected.

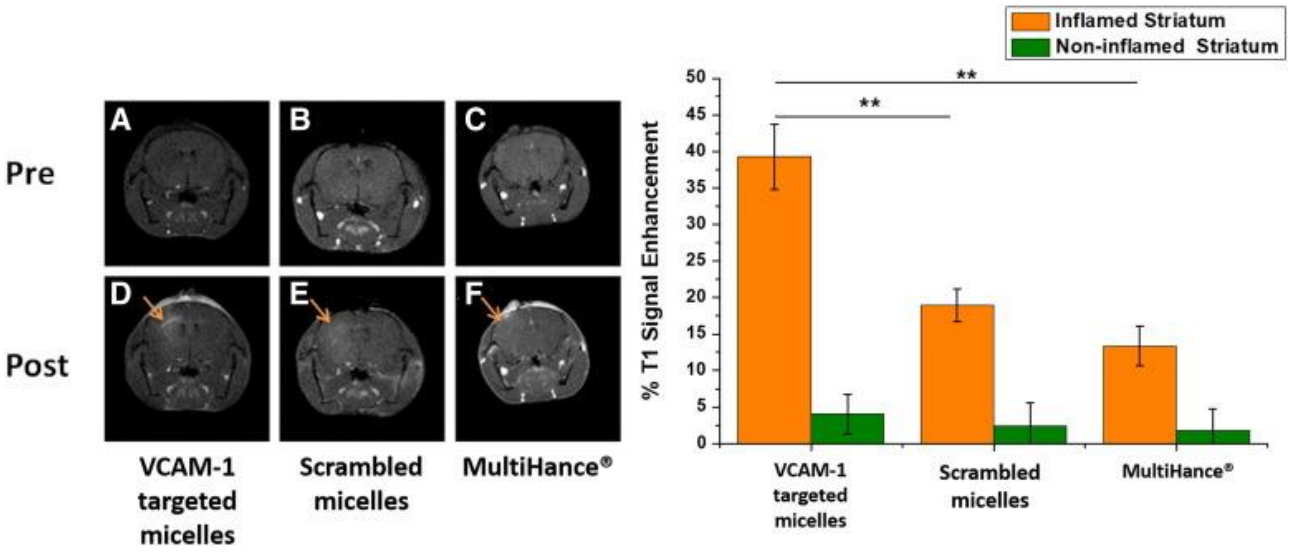

Figure 6. Left: 1 T MRI of neuroinflamed mice before and 24 h after iv injection of (A and D) VCAM-1targeted or (B and E) scrambled micelles (0.05 $mmol_{Gd}$/kg), or before and 20 min post (C and F) MultiHance (0.2 $mmol_{Gd}$/Kg) administration. Right: corresponding % T_1 Signal Enhancement calculated in the diseased (orange bars) and healthy (green bars) striatum. Error bars represent SE of the mean (**P < 0.01, n = 16).

Interestingly, the kinetic of the contrast enhancement observed for the two nanosystems was a bit different, with the targeted system that performed much better after 24 h post-injection, whereas at 48 h the two micelles showed a very similar effect. Most likely, this observation is an indirect demonstration of the effective targeting of the VCAM-1 directed system, and it suggests that the targeting to the receptor (though, likely, it is not the only process accounting for the accumulation of the probe in the inflamed area) is a faster event than the passive accumulation occurring for the untargeted micelles. The signal obtained 24 h post injection of the scrambled micelles was definitely comparable to the T_1-SE detected 20 min after the administration of the contrast agent MultiHance (13.4% ± 2.7%), which is clinically employed to evaluate the presence of alterations in blood brain barrier permeability. This finding suggests that the contrast obtained after the administration of scrambled micelles is mainly related to passive extravasation, thus further supporting the view that VCAM-1 targeted micelles effectively bind the corresponding target *in vivo*.

Biodistribution of VCAM-1 targeted micelles

The biodistribution of the targeted micelles was investigated in the main excretory organs, either *in vivo* by MRI (at 20 min, 4 h and 24 h post injection) or *ex-vivo* by ICP-MS (Gd quantification at 24 h post injection, see Supplementary Information). Moreover, with the prospect of assessing the real power of the targeted nanomedicine, the percentage of the metal found in the main excretory and targeted organs 24 h post injection was calculated over the total administered Gd(III) dose. As displayed in Figure 7, the large majority of the administered Gd(III) (44% ± 5%) accumulated in the

liver, whereas much less Gd (0.5%-3%) was found in spleen, lungs, and kidneys. Though only a very small fraction was found in the inflamed region, the amount accumulated in the LPS-treated hemisphere was 400% higher than healthy contralateral brain (0.29% ± 0.03% *vs.* 0.06% ± 0.01%, respectively; $P < 0.0001$).

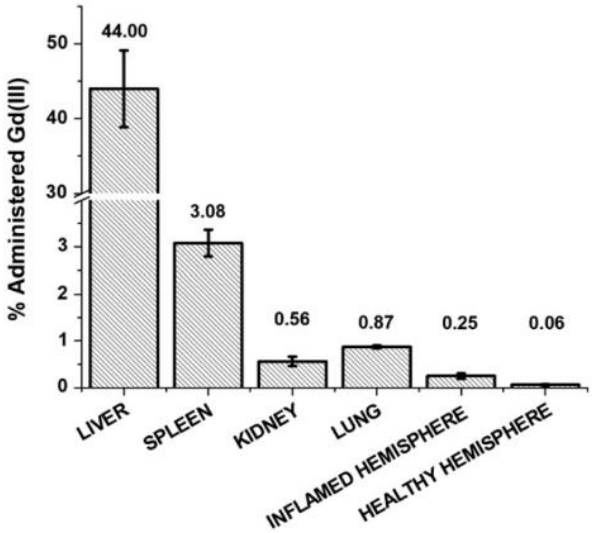

Figure 7. Quantification of % Gd^{3+} content in main excretory and target organs, 24 h post administration of VCAM-1 targeting micelles (n = 6), calculated over the total administered Gd^{3+} dosage. The % mean value measured in each organ is displayed in the chart. Error bars represent SE of the mean.

Ex-vivo studies

The effective targeting of VCAM-1 micelles was also investigated post-mortem by fluorescence microscopy. Brain slices were obtained from treated mice sacrificed 24 h post injection of targeted micelles. A widespread signal originating from the rhodamine dye embedded in the micelles was detected in the inflamed striatum, whereas only a faint and almost negligible fluorescence was visible in the contra-lateral one. Staining of vessels was performed with either anti-CD31 antibody, widely used as marker of brain endothelial cells (**44**) (Figure 8A), or anti VCAM-1 antibody (Figure 8B and C). Results obtained showed a massive accumulation of micelles not only stuck to the vessels, but also in the cytoplasm of adjacent and extravasating cells. Remarkably, a high degree of binding to the target was still present 24 h post injection, confirming the peptide targeting efficiency and supporting the idea of employing ultra-small and long circulating nanosystem. As a result of confocal microscopy experiments, the idea that the homing of VCAM-1 targeted micelles at the inflammation site could be additionally supported by immune system cells was conceived. The hypothesis was based on the view that a variable amount of micelles could be phagocytosed by bone marrow-derived (BMD) cells or activated microglia either during systemic circulation or after the eventual blood brain barrier extravasation. To better clarify this point, brain slices were stained with anti F4-80 antibody (Figure 8D and E) proving a massive presence of macrophages at the lesion site, some

of which loaded with the fluorescent micelles. However, sporadic presence of micelles in non-macrophagic cells was still visible. In the brain slices extracted from mice injected with the scrambled nanosystem, instead, fewer micelles were detected and most of them were confined in the cytoplasm of F4-80 positive cells. The absence of a widespread number of micelles stacked to the vessels supports the idea of an increase of MRI signal closely related to passive extravasation and immune system cell mediated delivery.

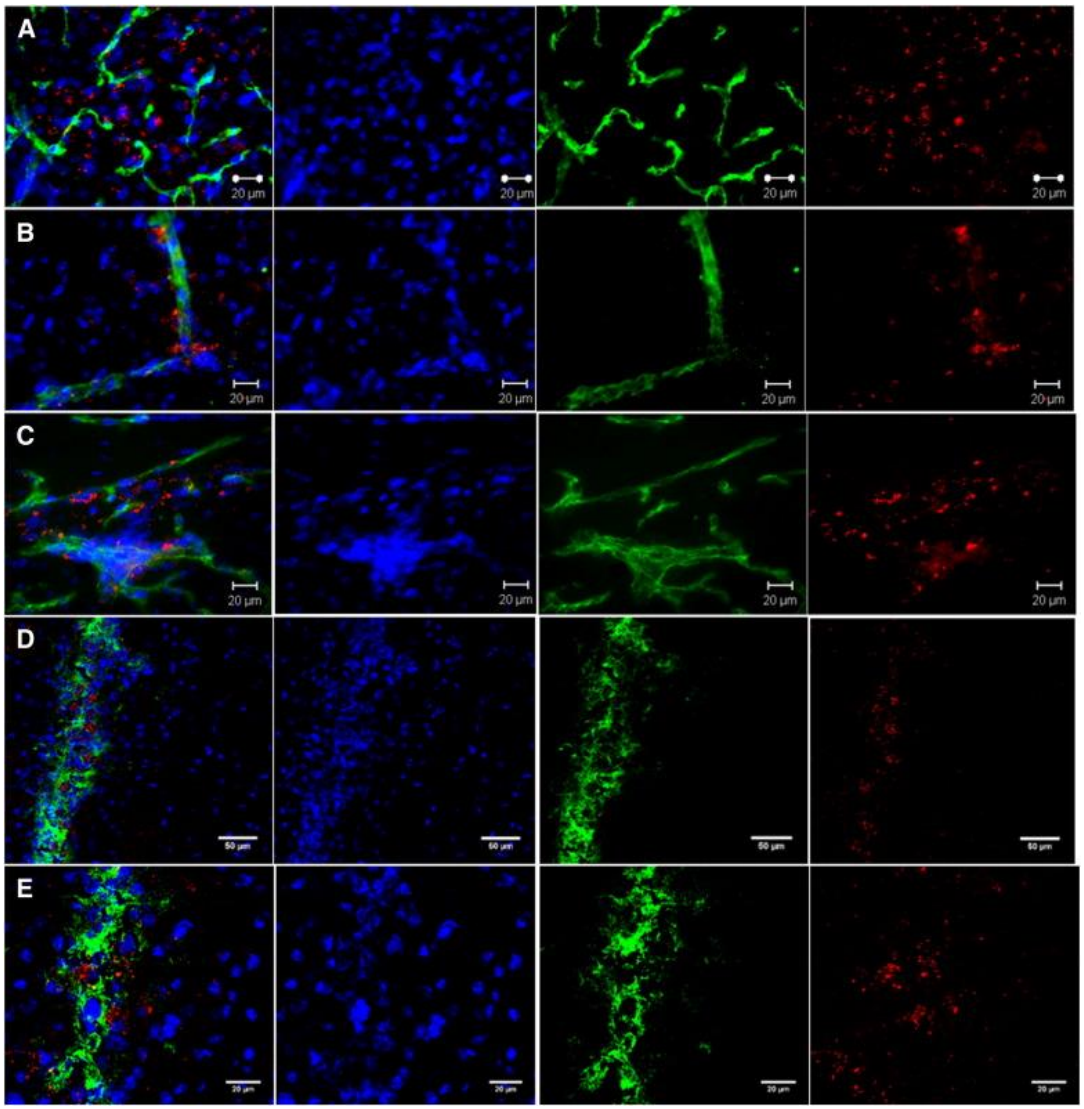

Figure 8. Confocal microscopy images of the inflamed striatum of C57BL/6J mice taken 24 h post VCAM-1 targeting micelle injection. In the first column merge of the three channels is displayed; in the other columns channels are displayed separately. Nuclei are stained in blue; micelles are shown in red. (A) CD31 staining (green) of brain endothelial cells; (B and C) VCAM-1 staining (green) showing colocalization of micelles and related target; (D and E) macrophage staining with anti F4/80 antibody (green) at two different magnifications.

Discussion

The development of an imaging probe for the MRI early visualization of neuroinflammation could be of great help in the comprehension, interception and prevention of various neurological disorders. This process, in fact, is diffuse and actively involved in demyelinating and neurodegenerative diseases, stroke and malignant CNS tumors (**45**). As extensively reviewed by Pulli et al (**46**), VCAM-1 has been selected as target to detect neuroinflammation, mainly by MRI, in manifold papers. However, most of the probes reported were intended to achieve a negative MRI contrast. For instance, 1 μm sized particles of iron oxide conjugated to anti-VCAM1-antibody, further referred to as VCAM1-MPIO, were successfully tested in a model of acute neuroinflammation, of autoimmune encephalomyelitis (EAE) or for earlier detection of brain metastases (**37,47,48**). However, T_2 contrast agents, despite their great sensitivity, are not ideal to detect subtle neurodegenerative disorders as T_2 hyper-intensities in the brain could be also associated with the presence of haemorrhagic foci, intracranial metastases, mucous- or protein-containing lesions, iron, copper or calcium deposition, turbulent flow of the cerebrospinal fluid, air-containing spaces, demyelination or axonal loss (**41**). The signal obtained with T_1 contrast agents, instead, is more specific and limited to the diseased area, without the occurrence of "blooming artifacts". Actually, Gd-complexes are widely used in clinics to highlight BBB breakdown, but a micromolar accumulation of the probe is required to clearly visualize a signal, thus restricting the detection of inflammation to severe clinical cases and reducing the chances of visualization of mild and early-stage phenomena. So far, the use of targeted T_1 probes has been quite limited in literature, possibly due to the lower sensitivity associated with Gd(III) compounds in comparison to iron oxide particles. Chen et al developed a myeloperoxidase (MPO)-activatable paramagnetic sensor to detect more and confirm smaller and earlier active demyelinating lesions in the EAE model, due to the achievement of longitudinal relaxivity values around 25.0 mM_{Gd}^{-1} s^{-1} (at 1.5 T) in the presence of high amounts of the soluble MPO enzyme (49). The micellar probe herein presented has the advantage of carrying a quite high payload of Gd(III) chelates per micelle (*ca.* 850, as calculated from the surface area of the micelle components) (**42**), and it is characterized by a considerably high longitudinal relaxivity value per millimolar concentration of particle of *ca.* 3.0×10^4 mM^{-1} s^{-1} (at 1 T). The targeted micelles displayed a good *in vitro* affinity towards the brain endothelial cell model investigated (bEnd.3), whose VCAM-1 expression was further increased by TNF-alpha activation. The *in vivo* T_1 signal enhancement in the inflamed brain measured 24 h post micelle injection attested at around 40%, a significant value if considered that it was calculated over the entire striatum. Moreover, the real extension of inflammation visible after the

administration of the nanosystem was considerably higher than the one perceived using mere T_2 pre-contrast acquisitions or T_1 images after the injection of the clinical agent MultiHance, thus confirming the good potential of the developed system. The peak of T_1 SE at 24 h post injection was actually quite unexpected as in our previous work (**42**) on a peripheral inflammation model, the maximum contrast was detected 4 h post-injection. However, this finding is not unprecedented (**50-52**). The reason of this delayed enhancement probably lies in the need of a consistent accumulation of the nanosystem at the lesion site, achievable through its progressive binding to VCAM-1 receptor, BBB crossing, possible interaction with proteins and labelling of immune cells that conceivably migrate to the CNS.

A deep pharmacokinetic investigation of the nanosystem was performed and resulted in a mean blood-half-life of targeted micelles a bit longer than 6 h, a value in line with other PEGylated nanosystems (**53**) and remarkably different to the very short (< 5 min) circulation time reported for the micron-sized anti VCAM-1 iron oxide particles mentioned above (**48**). The extended blood circulation time is likely due to the relatively small size of the particle that reduces the recognition by monocytes and macrophages. This is an important finding, not only because a long circulation time may favour the binding of the peptide to the endothelial marker of inflammation, but also for promoting a possible extravasation of the system. As further proof of this observation, the *ex-vivo* histological studies carried out demonstrated the occurrence of a strong binding between micelles and blood brain barrier capillaries, still 24 h post injection, giving the opportunity to follow VCAM-1 expression for a prolonged time window. Even if the presence of micelles inside microglia/macrophages was detected by confocal microscopy, it has to be still clarified whether the uptake occurred during circulation or directly at the inflammation site. However, as far as the detection sensitivity is concerned, this finding is not disturbing because macrophage infiltration and local microglia activation play a key role in neuroinflammation, and both contribute to enhance the MRI contrast in the diseased site with respect to healthy brain. In spite of the good contrast observed, we found that just the 0.3% of the injected Gd(III) reached the targeting site, against a still remarkable liver accumulation (45% of the injected metal), attributable to the unspecific sequestering operated by liver-resident macrophages (**54**). In principle, several routes can be envisaged to improve the overall performance of the protocol including the modulation of the nanoparticle size, the optimization of the micelle formulation (relative ratio among phospholipids, Gd(III), and targeting peptide), the design of a more efficient Gd(III) chelate, and the development of strategies to reduce the liver accumulation of the nanosystem as the pre-saturation of the resident macrophages through the administration of free-Gd micelles before the

injection of the smart nanosystem (**55**). The use of micelles is certainly a valuable approach even in view of the possible exploitation of the VCAM-1 targeted agent for theranostics purposes, as a growing number of papers already demonstrated the advantages of using micelles as drug delivery systems (**56-58**). Loading VCAM1-directed micelles with anti-inflammatory or anti-cancer molecules would allow the monitoring and treatment of neuro-inflammatory disorders or CNS malignant cancer, respectively. However, it has to be noticed that effective potential of the presented nano-agent for assessing neuroinflammation in neurodegenerative diseases will require the validation in more clinically relevant models, *i.e.* characterized by a chronic evolution of the pathology.

In summary, this work demonstrates that paramagnetic Gd-loaded targeted micelles have the potential to visualize VCAM-1 expression *in vivo* in a mouse model of acute neuroinflammation. The developed micelles displayed a quite long blood half-life that guarantees a good accumulation in the inflamed region and a well-detectable imaging contrast. Besides the expected vascular target and limited passive extravasation of the micelles, data also suggested an immune-mediated brain accumulation across the BBB of the nanoparticles. Such results could pave the way to interesting future diagnostic/theranostic applications of this nanosystem implying the loading of neuroprotective or even anti-cancer drugs inside the hydrophobic core of the micelles.

References

1. Amor S, Puentes F, Baker D, van der Valk P. Inflammation in neurodegenerative diseases. Immunology 2010;129(2):154-69.

2. Faden AI, Loane DJ. Chronic neurodegeneration after traumatic brain injury: Alzheimer disease, chronic traumatic encephalopathy, or persistent neuroinflammation? Neurotherapeutics 2015;12(1):143-50.

3. Ellwardt E, Zipp F. Molecular mechanisms linking neuroinflammation and neurodegeneration in MS. Exp Neurol 2014;262(Pt A):8-17.

4. Ory D, Celen S, Verbruggen A, Bormans G. PET radioligands for in vivo visualization of neuroinflammation. Curr Pharm Des 2014;20(37):5897-913.

5. Jacobs AH, Tavitian B, the INMiND Consortium. Noninvasive molecular imaging of neuroinflammation. J Cereb Blood Flow Metab 2012;32(7):1393-415,

6. Morales I, Guzmán-Martínez L, Cerda-Troncoso C, Farías GA, Maccioni RB. Neuroinflammation in the pathogenesis of Alzheimer's disease. A rational framework for the search of novel therapeutic approaches. Front Cell Neurosci 2014;8:112.

7. Wilcock DM. A changing perspective on the role of neuroinflammation in Alzheimer's disease. Int J Alzheimers Dis 2012;2012:495243.

8. Quarantelli M. MRI/MRS in neuroinflammation: methodology and applications. Clin Transl Imaging 2015;3:475-89.

9. Witte ME, Geurts JJ, de Vries HE, van der Valk P, van Horssen J. Mitochondrial dysfunction: a potential link between neuroinflammation and neurodegeneration? Mitochondrion 2010;10(5):411-8.

10. Heneka MT, et al. Neuroinflammation in Alzheimer's disease. Lancet Neurol 2015;14(4):388-405.

11. Frank-Cannon TC, Alto LT, McAlpine FE, Tansey MG. Does neuroinflammation fan the flame in neurodegenerative diseases? Mol Neurodegener 2009;4:4747.

12. Hirsch EC, Hunot S. Neuroinflammation in Parkinson's disease: a target for neuroprotection? Lancet Neurol 2009;8(4):382-97.

13. Haider L, Zrzavy T, Hametner S, et al. The topography of demyelination and neurodegeneration in the multiple sclerosis brain. Brain 2016;139(3):807-15

14. Crotti A, Glass CK. The choreography of neuroinflammation in Huntington's disease. Trends Immunol 2015;36(6):364-73

15. Aronica E, Crino PB. Inflammation in epilepsy: clinical observations. Epilepsia 2011;52(Suppl 3):26-32.

16. Agrawal M, Biswas A. Molecular diagnostics of neurodegenerative disorders. Front Mol Biosci 2015;2:54

17. Mueller SG, Weiner MW, Thal LJ, et al. Ways toward an early diagnosis in Alzheimer's disease: the Alzheimer's disease neuroimaging initiative (ADNI). Alzheimers Dement 2005;1(1):55-66

18. Stoessl AJ. Neuroimaging in the early diagnosis of neurodegenerative disease. Translational Neurodegeneration 2012;1:5

19. Landau SM, Fero A, Baker SL, et al. Measurement of longitudinal β- amyloid change with 18F-florbetapir PET and standardized uptake value ratios. J Nucl Med 2015;56(4):567-74

20. Shoghi-Jadid K, Small GW, Agdeppa ED, Kepe V, Ercoli LM, Siddarth P, et al. Localization of neurofibrillary tangles and beta-amyloid plaques in the brains of living patients with Alzheimer disease. Am J Geriatr Psychiatry 2002;10(1):24-35.

21. Rupprecht R, Papadopoulos V, Rammes G, Baghai TC, Fan J, Akula N, et al. Translocator protein (18 kDa) (TSPO) as a therapeutic target for neurological and psychiatric disorders. Nat Rev Drug Discov 2010;9:971-88.

22. Venneti S, Lopresti BJ, Wiley CA. Molecular imaging of microglia/ macrophages in the brain. Glia 2013;61(1):10-23

23. Thiel A, Heiss WD. Imaging of microglia activation in stroke. Stroke 2011;42(2):507-12.

24. Chauveau F, BoutinH,VanCampN,Dolle F, TavitianB.Nuclear imaging of neuroinflammation: a comprehensive review of [11C]PK11195 challengers. Eur J Nucl Med Mol Imaging 2008;35:2304-19.

25. Jalbert JJ, Daiello LA, Lapane KL. Dementia of the Alzheimer type. Epidemiol Rev 2008;30:15-34.

26. Sabuncu MR, Desikan RS, Sepulcre J, et al. The dynamics of cortical and hippocampal atrophy in Alzheimer disease. Arch Neurol 2011;68(8):1040-8,

27. Mascalchi M, Lolli F, Della Nave R, Tessa C, Petralli R, Gavazzi C, et al. Huntington disease: volumetric, diffusion-weighted, and magnetization transfer MR imaging of brain. Radiology 2004;232(3):867-73.

28. Filippi M, Rocca MA. MR imaging of multiple sclerosis. Radiology 2011;259(3):659-81.

29. Ge Y. Multiple sclerosis: the role of MR imaging. AJNR Am J Neuroradiol 2006;27(6):1165-76.

30. Tuite PJ, Mangia S, Michaeli S. Magnetic resonance imaging (MRI) in Parkinson's disease. J Alzheimers Dis Parkinsonism 2013(Suppl 1):001,

31. Schwarz ST, Afzal M, Morgan PS, Bajaj N, Gowland PA, et al. The ‘swallow tail’ appearance of the healthy nigrosome — a new accurate test of Parkinson's disease: a case-control and retrospective crosssectional MRI study at 3T. PLoS One 2014;9(4)e93814.

32. Ransohoff RM, Kivisäkk P, Kidd K. Three or more routes for leukocyte migration into the central nervous system. Nat Rev Immunol 2003;3(7):569-81.

33. Wilson EH, Weninger W, Hunter CA. Trafficking of immune cells in the central nervous system. J Clin Invest 2010;120(5):1368-79

34. Ceulemans A-G, Zgavc T, Kooijman R, Hachimi-Idrissi S, Sarre S, Michotte Y. The dual role of the neuroinflammatory response after ischemic stroke: modulatory effects of hypothermia. J Neuroinflammation2010;7:74

35. Ferretti MT, Merlini M, Späni C, Gericke C, Schweizer N, Enzmann G, et al. T-cell brain infiltration and immature antigen-presenting cells in transgenic models of Alzheimer's disease-like cerebral amyloidosis. Brain Behav Immun 2016;54:211-25.

36. Man S, Ubogu EE, Ransohoff RM. Inflammatory cell migration into the central nervous system: a few new twists on an old tale. Brain Pathol 2007;17(2):243-50.

37. McAteer MA, Sibson NR, von zur Mühlen C, et al. In vivo magnetic resonance imaging of acute brain inflammation using microparticles of iron oxide. Nat Med 2007;13(10):1253-8,

38. McAteerMA, Akhtar AM, von zurMuhlen C, Choudhury RP. An approach to molecular imaging of atherosclerosis, thrombosis, and vascular inflammation using microparticles of iron oxide. Atherosclerosis 2010;209(1):18-27

39. Burtea C, Ballet S, Laurent S, Rousseaux O, Dencausse A, Gonzalez W, et al. Development of a magnetic resonance imaging protocol for the characterization of atherosclerotic plaque by using vascular cell adhesion molecule-1 and apoptosis-targeted ultrasmall superparamagnetic iron oxide derivatives. Arterioscler Thromb Vasc Biol 2012;32(6):e36-48,

40. Burtea C, Laurent S, Port M, Lancelot E, Ballet S, Rousseaux O, et al. Magnetic resonancemolecular imaging of vascular cell adhesionmolecule-1 expression in inflammatory lesions using a peptide-vectorized paramagnetic imaging probe. J Med Chem 2009;52(15):4725-42,

41. Zimny A, Neska-Matuszewska M, Bladowska J, Sąsiadek MJ. Intracranial lesions with low signal intensity on T2-weighted MR images—review of pathologies. Polish J Radiol 2015;80:40-50

42. Pagoto A, Stefania R, Garello F, Arena F, Digilio G, Aime S, et al. Paramagnetic phospholipid-based micelles targeting VCAM-1 receptors for MRI visualization of inflammation. Bioconjug Chem 2016;27(8):1921-30.

43. Vaccaro M, Mangiapia G, Paduano L, Gianolio E, Accardo A, Tesauro D, et al. Structural and relaxometric characterization of peptide aggregates containing gadolinium complexes as potential selective contrast agents in MRI. ChemPhysChem 2007;8:2526-38.

44. Körbelin J, Dogbevia G, Michelfelder S, et al. A brain microvasculature endothelial cell-specific viral vector with the potential to treat neurovascular and neurological diseases. EMBO Mol Med 2016;8(6):609-25

45. Hohlfeld R, Kerschensteiner M, Meinl E. Dual role of inflammation in CNS disease. Neurology 2007;68

46. Pulli B, Chen JW. Imaging neuroinflammation — from bench to bedside. J Clin Cell Immunol 2014;5:226.

47. Hoyte LC, Brooks KJ, Nagel S, et al. Molecular magnetic resonance imaging of acute vascular cell adhesion molecule-1 expression in a mouse model of cerebral ischemia. J Cereb Blood Flow Metab 2010;30(6):1178-87

48. Serres S, Soto MS, Hamilton A, et al. Molecular MRI enables early and sensitive detection of brain metastases. Proc Natl Acad Sci U S A 2012;109:6674-9.

49. Chen JW, Breckwoldt MO, Aikawa E, Chiang G, Weissleder R. Myeloperoxidase-targeted imaging of active inflammatory lesions in murine experimental autoimmune encephalomyelitis. Brain 2008;131(4):1123-33.

50. Sipkins DA, Gijbels K, Tropper FD, Bednarski M, Li KC, Steinman L. ICAM-1 expression in autoimmune encephalitis visualized using magnetic resonance imaging. J Neuroimmunol 2000;104(1):1-9.

51. Wuerfel E, Infante-Duarte C, Glumm R, Wuerfel JT. Gadofluorine Menhanced MRI shows involvement of circumventricular organs in neuroinflammation. J Neuroinflammation 2010;7:70.

52. Chung EJ, Cheng Y,Morshed R, et al. Fibrin-binding, peptide amphiphile micelles for targeting glioblastoma. Biomaterials 2014;35(4):1249-56.

53. Jokerst JV, Lobovkina T, Zare RN, Gambhir SS. Nanoparticle PEGylation for imaging and therapy. Nanomedicine (Lond) 2011;6(4):715-28

54. Wilhelm S, et al. Analysis of nanoparticle delivery to tumours. Nat Rev Mater 2016;1(5):16014,

55. Dietrich T, et al. Pre-saturation of the liver and subsequent administration of the contrast agent. WO Pat, 2015044312 A1; 2016.

56. Kedar U, Phutane P, Shidhaye S, Kadam V. Advances in polymeric micelles for drug delivery and tumor targeting. Nanomedicine 2010;6(6):714-29, https://doi.org/10.1016/j.nano.2010.05.005.

57. Al-Achi A, Jonathan Lawrence BS. Micelles: chemotherapeutic drug delivery. Clin Pharmacol Biopharm 2013;2e114.

58. Gaucher G, Satturwar P, Jones MC, Furtos A, Leroux JC. Polymeric micelles for oral drug delivery. Eur J PharmBiopharm2010;76(2):147-58,

Chapter 3

Imaging of prostate cancer

3.1- AAZTA tetramers as building blocks for bioconjugation

Based on:

Tripepi M., Capuana F., Gianolio E., Kock F.V., **Pagoto A**., Stefania R., Digilio G., Aime S.
Synthesis of high relaxivity gadolinium AAZTA tetramers as building blocks for bioconjugation, Bioconjugate Chemistry - 2018

Introduction

Low Molecular Weight (LMW) Gd(III)-chelates are used as contrast agents (CAs) in about 40% of the Magnetic Resonance Imaging (MRI) clinical scans worldwide. The efficacy of Gd(III)-complexes as MRI CAs is due to their ability to accelerate the water proton relaxation rate in tissues, adding valuable patho-physiologic contrast information to the inherent anatomic resolution of MR images. Besides the well established applications of Gd-based chelates in clinical MRI, interesting perspectives are expected also in the field of diagnostic X-ray based Computed Tomography (CT) techniques. Spectral Photon Counting Computed Tomography (SPCCT) is a recent X-ray based medical imaging technique that allows the quantitation of electron-dense elements in a specific ROI by exploiting their specific K-edge absorption (**1**). Gadolinium has been shown to have almost ideal physico-chemical properties in terms of K-edge absorption energy and specific absorption coefficient to behave as a CA for SPCCT (**2,3**). However, it is already clear that the new applications will rely on the attainment of high local concentrations of the Gd-containing systems. Currently, CAs used in the clinics are LMW Gd-chelates that extravasate aspecifically into tissues. Some of the clinically relevant LMW Gd-chelates contain hydrophobic groups that endow them with a high binding affinity to serum albumin, hence a prolonged lifetime in the bloodstream and suitable properties for angiographic applications (blood pool agents) (**4-6**). It was soon realized that Gd-chelates could be functionalized with epitopes having high binding affinity and specificity for molecular targets other than albumin, paving the way to molecular imaging by MRI (**7,8**). Molecular imaging of biological targets requires the specific accumulation of suitable amounts of contrast agents at the target. However, the tissue density of the molecular target might be inherently low and MRI has an intrinsically low sensitivity as compared to other molecular imaging modalities, such as nuclear medicine (NM) or optical imaging (OI). As a consequence, MR molecular imaging applications may be hampered by the amount of CA that can be accumulated with a 1:1 gadolinium-to-target stoichiometric ratio (**9,10**). An approach to increase the density of the contrast agent at the targeting sites is to link several Gd-chelates to the same binding vector in order to accumulate multiple copies of the CA in a single target binding event. This can be done by attaching a number of Gd chelates to a scaffold with multimeric/dendrimeric structure, which must be then conjugated to the target binding vector. The target binding moieties used in MR molecular imaging belong to widely heterogeneous classes of chemical structures. Proteins, polypeptides, antibodies, DNA, polysaccharides, and lipids have been used as vectors (**11,12**).

Often, the targeting vector is displayed on the surface of nanoparticles or liposomes (**13**). As the synthesis and/or purification of such systems can be time and effort demanding, it is of paramount

importance to develop highly sensitive, multimeric Gd-chelates carrying functional groups for a prompt, conjugation to the targeting vectors. The availability of such methods will provide molecular imaging scientists with a modular approach to easily assemble the needed imaging labelled targeted probe. In this paper, we describe the synthesis of novel Gd-tetramers ending up with different functional groups ready for the bioconjugation to the targeting vectors (see Scheme 1). The selected metal chelator is the heptadentate AAZTA ligand (AAZTA= 6-amino-6-methylperhydro-1,4-diazepinetetraacetic acid). The [Gd(III)-AAZTA]- complex (shortly, Gd- AAZTA) shows very good relaxivity properties (7.1 mM^{-1} s^{-1} at 21.5 MHz and 25°C), as the heptadentate AAZTA chelator leaves room for two fast exchanging water molecules (q=2, τ_M=90 ns) in the inner coordination sphere of Gd(III) (**14**). Despite the relatively low denticity of AAZTA, the Gd-complex shows very good thermodynamic stability and kinetic inertness as compared to complexes with other octadentate polyaminocarboxylic ligands (**15**). Moreover, its mesocyclic structure should ensure a higher metabolic stability as compared to linear chelators (**16,17**). These properties make Gd-AAZTA very attractive for clinical translation (**18**) and for the development of dendrimers with enhanced relaxivity (**19,20**). Four AAZTA-C_4COOH units were linked through amide bonds to a lysine-based dendrimer (dK3), to obtain the AAZTAtetramer (**L1**). The latter compound was functionalized with three different functional groups for conjugation, to obtain namely: *i)* compound **L2**, bearing the maleimide conjugation group able to react with free thiols to yield a thioester bond; *ii)* compound **L3**, bearing an aromatic aldehyde able to react with an aromatic hydrazine-labeled molecule to yield a bis-aryl hydrazone-conjugate; *iii)* compound **L4** bearing a dibenzocyclooctyne (DBCO) moiety able to react with an azide-labeled molecule to yield a triazole conjugate via Cu(I)-free click chemistry (**21**) The **L2-4** ligands were complexed with Gd(III) ions to yield the corresponding Gd-tetramers (namely, **Gd-L2**, **Gd-L3** and **Gd-L4**), ready for bioconjugation. As an example, the protocol for conjugation of the **Gd-L2** tetramer to a fibrin-targeting peptide is also reported.

Experimental Procedures

Bis-(2-aminoethyl)-ether trityl resin, Fmoc-Lys(Fmoc)-OH and activators HBTU (*O*- (Benzotriazol-1-yl)-*N,N,N',N'*-tetramethyluroniumhexafluorophosphate), PyBOP(Benzotriazole-1-yl-oxy-tris-pyrrolidino-phosphonium hexafluorophosphate) were purchased from Novabiochem (Darmstadt, Germany). All other chemicals were purchased from Sigma-Aldrich. NMR spectra were recorded at 310 K on a Bruker AVANCE 600 spectrometer. Mass spectra with electrospray ionization (ESI) were

recorded on a SQD 3100 Mass Detector (Waters). The HPLC-MS analytical and preparative analysis were carried out on a Waters AutoPurification system (3100 Mass Detector, 600 Quaternary Pump Gradient Module, 2767 Sample Manager and 2487 UV/Visible Detector). All ligands were characterized by NMR on a Bruker AVANCE 600 NMR spectrometer operating at 14T (corresponding to 600 MHz and 150 MHz ^{1}H and ^{13}C Larmor frequencies, respectively). The purified ligands **L1-4** were freeze- dried from water solution at pH 2-3 and the powder re-dissolved in DMSO-d6 for NMR analysis. Either homonuclear (2DTOCSY, 2D-COSY, 2D-NOESY) and heteronuclear (2D-1H,13C HSQC, 2D-^{1}H,^{13}C-HMBC) two-dimensional NMR experiments were acquired to assign the spectra and confirm the structure of the ligands.

Synthesis of L1

Bis-(2-aminoethyl)-ether trityl resin (0.96 mmol; 1.95 g) was loaded into a reaction vessel and dimethylformamide (DMF) (25 mL) was added to swell it for about 10 min. After the elimination of DMF, a mixture of Fmoc-Lys(Fmoc)-OH (2.39 mmol; 1.41 g), PyBOP (2.39mmol; 1.24 g) and DIPEA (4.78 mmol; 0.83 mL) in DMF (20 mL) was added in the reactor and shaken for 1 h. The amino acid solution was then removed and 20% acetic anhydride-DMF (20 mL) was added and shaken for 15 minutes. The resin was washed five times with DMF and then the deprotection of the amino groups from Fmoc was done using 40% piperidine-DMF (20 mL) for 5 min and 20% piperidine-DMF (20 mL) for 15 minutes. After washing five times with DMF, the coupling cycle was repeat using double quantity of Fmoc-Lys(Fmoc)-OH (4.78 mmol; 2.82 g), PyBOP (4.78 mmol; 2.49 g) and DIPEA (9.55 mmol; 1.67 mL) in DMF (20 mL), the reaction was carried out again for 1 h, followed by DMF washing and piperidine treatment. After washing with DMF, a mixture of AAZTA(tBu)$_4$C$_4$COOH$_{22}$ (4.02 mmol; 2.7g), PyBOP (4.01 mmol; 2.09 g) and DIPEA (8.02 mmol; 1.40 mL) in DMF (20 mL) was added to the reactor and it was shaken for 1 hour. The resin was washed five times with DMF and then thrice with dichloromethane (DCM). Afterwards, diethyl ether (Et_2O) was used to completely dry the resin before the cleavage. A cocktail solution of DCM, trifluoroacetic acid (TFA) and triisopropylsilane (TIS) in a ratio 49:49:2 (10 mL) was added in the reactor and it was shaken for 5 min. The solution was collected in a round-bottom flask and the process was repeated three times.

Then the combined filtrate was reduced almost to dryness and freshly TFA was added and stirred overnight until the complete removal of tBu of AAZTA. The mixture was then concentrated *in vacuo* and cold Et_2O (30 mL) was added to let the product precipitate. The precipitate was centrifuged and washed thrice with Et_2O.

The crude product was dissolved in 5 mL of water and purified by preparative RP-HPLC using a Waters XTerra prep RPdC8, 5 µm, 19x100 mm column by Method 1 and H_2O/0.1% TFA (A) and CH_3CN/0.1% TFA (B) as eluents. The volume of injection was 600 µL for every run and the desired product was fractioned, collected and freeze-dried overnight. The pure product was obtained as a white powder (1.2 g, 57% of yield). The purity of the **L1** was evaluated by analytical HPLC using XTerra RPdC8, 5 µm, 4.6x150 mm column, by Method 2 and H_2O/0.1% TFA (A) and CH_3CN/0.1% TFA (B) as eluents: a retention time of 5.84 min and a degree of purity of 98.7% of **L1** were estimated (λ=220 nm).

A

Time	%A	%B
0.00	95	5
1.43	95	5
5.00	85	15
12.00	50	50

B

Time	%A	%B
0.00	95	5
1.25	85	15
8.73	80	20
23.00	60	40
25.00	0	100

Table 1. Method for HPLC-MS analysis of crude product (A) and pure product (B) of the ligand **L1**. eluents A, H_2O(0,1 % TFA); B, CH_3CN (0,1% TFA)

ESI-MS (m/z): $[M+2H]^{2+}$ 1104.0 (obsd.), 1104.0 (calcd. for $C_{94}H_{156}N_{20}O_{40}$); $[M+3H]^{3+}$ 736.3 (obsd.), 736.4 (calcd.); $[M+4H]^{4+}$ 552.6 (obsd.), 552.6 (calcd.). ^{1}H NMR (600 MHz, dmso-d6, T = 310K): 12.20 (br), 7.88 (5H, o), 7.79 (2H, d), 7.73-7.72 (2H, o), 4.22-4.19 (3H, o), 3.78 (16H, s), 3.65 (16H, o), 3.62 (2H, t, o), 3.48 (2H, t), 3.27 (18H, o), 3.20 (16H, o), 3.02 (8H, o), 2.15 (4H, o), 2.07 (4H, o), 1.66-1.53 (6H, o), 1.44- 1.25 (36H, o).

Synthesis of L2, L3 and L4

To a solution of **L1** (0.02 mmol; 50 mg) in buffer phosphate (50 mM; 3 mL; pH 7) was added N-Succinimidyl-3-maleimido propionate (0.06 mmol; 16 mg) or N-Succinimidyl-4-formylbenzoate (0.06 mmol; 15 mg) or Dibenzocyclooctyne-N-hydroxysuccinimidyl ester (0.06 mmol; 24 mg) dissolved in 1 mL of CH_3CN for compound **L2**, **L3**, **L4** respectively. After stirring 4h at RT, the organic phase was evaporated and the excess non-bound reagent and buffer products were removed by size exclusion chromatography on a HiTrap Desalting Column 5 mL prepacked with Sephadex G25, using Milli-Q H_2O as the mobile phase, after which the fractions corresponding to the functionalized product were collected. The **L2**, **L3**, **L4** compounds were checked with ESI-MS(+), freeze-dried obtaining about 70% of yield. The purity of modified **L1** ligands was evaluated by analytical HPLC

using XTerra RPdC8, 5 µm, 4.6x150 mm column, by Method 2 and H_2O/0.1% TFA (A) and CH_3CN/0.1% TFA (B) as eluents.

L2: ESI-MS (m/z): $[M+2H]^{2+}$ 1179.6 (obsd.), 1179.7 (calcd. for $C_{101}H_{161}N_{21}O_{43}$); $[M+3H]^{3+}$ 786.8 (obsd.), 786.8 (calcd.); $[M+4H]^{4+}$ 590.6 (obsd.), 590.2 (calcd.). Retention time 9.90 min, purity 90.0 %. ^{1}H NMR (600 MHz, dmso-d6, T = 310K): 12.20 (16H, br), 8.03 (1H, t), 7.94-7.85 (4H, o), 7.83 (1H, d), 7.80-7.73 (2H, o), 7.00 (2H, s), 4.22-4.13 (3H, o), 3.85-3.75 (16H, o), 3.61- 3.43 (18H, br, o), 3.41 3.35 (4H, o), 3.34-3.27 (18H, o), 3.23 (16H, s), 3.19-3.14 (2H, o), 2.99 (6H, o), 2.37 (2H, t), 2.15 (4H, o), 2.07 (4H, o), 1.66-1.53 (6H, o), 1.44-1.25 (36H, o).

L3: ESI-MS (m/z): $[M+2H]^{2+}$ 1170.0 (obsd.), 1170.0 (calcd. for $C_{102}H_{160}N_{20}O_{42}$); $[M+3H]^{3+}$ 780.5 (obsd.), 780.5 (calcd.); $[M+4H]^{4+}$ 585.8 (obsd.), 585.5 (calcd.). Retention time 10.05 min, purity 93.3 %. ^{1}H NMR (600 MHz, dmso-d6, T = 310K): 12.20 (16H, br), 10.10 (1H, s), 8.81 (1H, t), 8.08 (2H, d), 7.99 (2H, d), 7.95-7.86 (4H, o), 7.85 (1H, d), 7.80-7.75 (2H, o), 4.22-4.13 (3H, o), 3.85-3.75 (16H, o), 3.63 (16H, o), 3.57 (2H, t, o), 3.48 (2H, m, o), 3.45 (2H, o), 3.33-3.27 (18H, o), 3.23 (16H, s) 2.99 (6H, o), 2.15 (4H, o), 2.07 (4H, o), 1.66-1.53 (6H, o), 1.44-1.25 (36H, o).

L4: ESI-MS (m/z): $[M+2H]^{2+}$ 1261.6 (obsd.), 1261.9 (calcd. for $C_{115}H_{173}N_{21}O_{42}$); $[M+3H]^{3+}$ 841.5 (obsd.), 841.6 (calcd.); $[M+4H]^{4+}$ 631.6 (obsd.), 631.4 (calcd.). Retention time 18.47 min, purity 90.1 %. ^{1}H NMR (600 MHz, dmso-d6, T = 310K): 12.20 (16H, br), 8.01 (1H, t), 7.98-7.83 (6H, o), 7.80-7.74 (1H, o), 7.66 (1H, d), 7.59 (1H, d), 7.52 (1H, t), 7.51-7.46 (2H, o), 7.42 (1H, t), 7.38 (1H, t), 7.32 (1H, d), 5.08 (2H, d), 4.24-4.18 (3H, br, o) 3.87 (16H, o), 3.66 (16H, o), 3.43-3.37 (18H, o), 3.36-3.29 (18H, o), 3.25-3.13 (4H, o), 3.02 (6H, o), 2.22-2.13 (6H, o), 2.07 (4H, o), 1.91 (2H, t), 1.79 (2H, m), 1.66-1.53 (6H, o), 1.44-1.25 (38H, o).

Synthesis of Gd(III)-complexes (Gd-L1, Gd-L2, Gd-L3 and Gd-L4).

An equimolar amount of $GdCl_3$ (170 mM water solution) was slowly added to a 60 mM ligand solution; the solutions were maintained at pH 6.5 with NaOH. The complexes were then desalted by size exclusion chromatography on a HiTrap Desalting Column 5 mL prepacked with Sephadex G25, using Milli-Q H_2O as the mobile phase and finally freeze-dried. The amount of residual free Gd^{3+} ions was assessed by the Orange Xylenol UV method (**23**). All complexes were found to contain less than 0.3% (mol/mol) of residual free Gd^{3+} ions. The overall gadolinium contents were determined by ^{1}H NMR T_1 measurement of the mineralized complex solution (in 6M HCl at 393 K for 16 h).

Gd-L1: ESI-MS m/z: $[M-2H]^{2-}$ 1410.9 (obsd.), 1410.3 (calcd. for $C_{94}H_{140}Gd_4N_{20}O_{40}$); $[M-3H]^{3-}$ 940.0 (obsd.), 939.5 (calcd.); $[M-4H]^{4-}$ 704.8 (obsd.) 704.1 (calcd.).

Gd-L2: ESI-MS m/z: $[M-3H]^{3-}$ 990.8 (obsd.), 990.9 (calcd. for $C_{101}H_{149}Gd_4N_{21}O_{43}$); $[M-4H]^{4-}$ 742.7 (obsd.), 742.9 (calcd.).

Gd-L3: ESI-MS m/z: $[M-3H]^{3-}$ 984.5 (obsd.), 984.5 (calcd. for $C_{102}H_{148}Gd_4N_{20}O_{42}$); $[M-4H]^{4-}$ 737.7 (obsd.), 738.4 (calcd.).

Gd-L4: ESI-MS m/z: $[M-3H]^{3-}$ 1045.4 (obsd.), 1045.6 (calcd. for $C_{115}H_{161}Gd_4N_{21}O_{42}$); $[M- 4H]^{4-}$ 783.7 (obsd.), 783.9 (calcd.).

Solid Phase Peptide Synthesis (SPPS)

Peptide WQPCPWESWTFCWDPGGGK containing the fibrin binding motif (**24**), was synthesized on Fmoc-Lys(Boc)-Wang resin by the use of standard 9-fluorenylmethyloxycarbonyl solid-phase peptide synthesis carried out on a Liberty CEM microwave synthesizer on a 0.1 mmol scale. At the end of the last cycle, the synthesized peptide was acetylated using 2-(2-Methoxyethoxy)acetic acid/DIPEA/HBTU. A cocktail solution of TFA, H_2O, Phenol and TIS in a ratio 88:5:5:2 (v/v/wt/v, 6 mL) was used to cleave the peptide from the resin and to obtain the side-chain deprotection. After 3 h, the cleavage solution was collected and concentrated to dryness. Et_2O was added to the residue to precipitate the crude peptide, which was collected. The crude linear dicysteine containing peptide was cyclized by dissolution in DMSO and H_2O (1:1, v/v) adjusting the pH of the solution to 7.5-8.5 by the addition of 100 mM aqueous Nmethylglucamine and stirring for 48 h. The reaction mixture was then diluted with water and purified by preparative HPLC using a Waters XTerra prep RPdC8, 5 µm, 19x100 mm column, by Method 3 and H_2O/TFA 0.1% (A) and CH_3CN/TFA 0.1% (B) as eluents. The purity of the peptide (0.07 g, 30% of yield) was evaluated by analytical HPLC using XTerra RPdC8, 5 µm, 4.6x150 mm column, by Method 4 and H_2O/TFA 0.1% (A) and CH_3CN/TFA 0.1% (B) as eluents. Retention time 19.21 min, purity > 80 %. ESI-MS (m/z): $[M+2H]^{2+}$ 1192.7 (obsd.), 1192.0 (calcd. for the linear peptide $C_{112}H_{143}N_{25}O_{30}S_2$); $[M+2H]^{2+}$ 1191.5 (obsd.), 1191.0 (calcd. for the cyclic peptide $C_{112}H_{141}N_{25}O_{30}S_2$), $[M+3H]^{3+}$ 794.5 (obsd.), 794.7 (calcd.).

A

Time	%A	%B
0.00	85	15
12.00	30	70
17.00	0	100

B

Time	%A	%B
0.00	85	5
21.00	30	5
31.00	0	100

Table 2. Methods for HPLC-MS analysis of peptide. eluents A, H_2O(0,1 % TFA); B, CH_3CN (0,1% TFA)

Next, the peptide was functionalized at the lysine ε-amino group with a SATA group by mixing the peptide and a 10 fold excess of SATA in DMF containing 3.6 % of TEA and stirring at RT, overnight. Subsequently, 10 mL of ethyl acetate were added to the reaction mixture and the precipitate,

corresponding to the SATA-peptide, was centrifuged to a pellet, washed twice with ethyl acetate (10 mL) and dried. The SATA-functionalized fibrinbinding peptide (**FibPep-SATA**) was obtained as a white powder.

ESI-MS (m/z): $[M+2H]^{2+}$ 1249.4 (obsd.), 1249.0 (calcd. for SATA-peptide $C_{116}H_{145}N_{25}O_{32}S_3$); $[M+3H]^{3+}$ 833.2 (obsd.), 833.4 (calcd.).

Synthesis of FibPep-Gd-L2.

To create **FibPep-Gd-L2** the SATA (SIGLA) group of the fibrinbinding peptide was deacetylated: 100ML of deacetylation solution (0.5 M NH_2OH, 25 mM EDTA, 50 mM sodium acetate, pH 6) was added to FibPep-SATA (13 mg, 8 µmol) in buffer (50 mM sodium acetate, pH 6.5, 2 mL), under argon atmosphere and the mixture was incubated at RT for 2 h. Subsequently, **Gd-L2** (24 mg, 8 µmol) was added and the reaction was stirred for other 30 min. The mixture was purified by gel permeation chromatography on a column packed with Sephadex G10 (1.1×12cm), using Milli-Q H_2O as the mobile phase. After freeze-drying the product fractions, 35 mg (80% yield) of a white solid was obtained. ESI-MS (m/z): $[M-5H]^{5-}$ 1085.0 (obsd.), 1084.1 (calcd. for $C_{215}H_{288}Gd_4N_{46}O_{74}S_3$); $[M-6H]^{6-}$ 903.3 (obsd.), 904.05 (calcd.); $[M-7H]^{7-}$ 774.1 (obsd.), 747.4 (calcd.).

Relaxometry

The longitudinal water protons relaxation rates were measured by using a Stelar SpinMaster relaxometer (Stelar, Mede (PV), Italy) operating at 0.5 T (21.5 MHz) Proton Larmor Frequency), by mean of the standard inversion-recovery technique. The temperature was controlled with a Stelar VTC-91 air-flow heater equipped with a copper constantan thermocouple (uncertainty 0.1°C). The proton 1/T1 NMRD profiles were measured at 298 K on a fast field-cycling Stelar relaxometer over a continuum of magnetic field strengths from 0.00024 to 0.47 T (corresponding to 0.01-20 MHz proton Larmor Frequency). The relaxometer operates under computer control with an absolute uncertainty in 1/T1 of ± 1%. Additional data points in the range 21.5-70 MHz were obtained on the Stelar SpinMaster relaxometer. The concentration of free Gd(III) ion in the aqueous solutions was determined after mineralization with HCl 37% w/w (1:1) and incubation at 393 K overnight. From the measurement of the observed relaxation rate (R1obs) of the acidic solution and knowing the relaxivity (r1) of Gd(III)aquo-ion in acid conditions (13.7 mM-1 s-1), it was possible to calculate the exact Gd(III) concentration.

Results and Discussion

Design, synthesis and characterization

The Ligand **L1** was designed to contain a single free amino group at the end of a spacer for further conjugation with a range of functional groups. Four AAZTA-units were connected to form a tetrameric compound through a branched tri-lysine scaffold (Scheme 1).

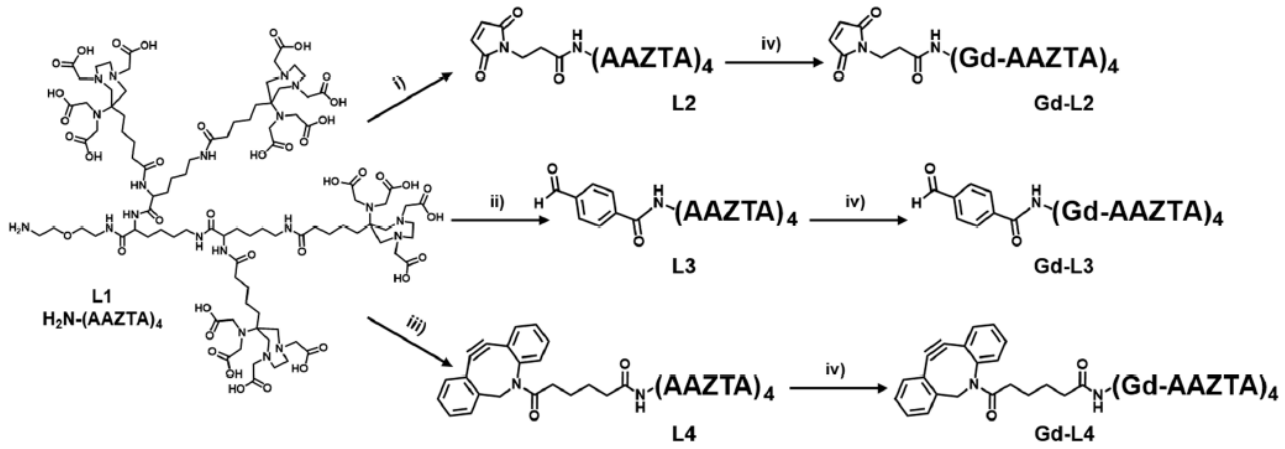

Scheme 1. Synthesis of ligands bearing functional groups for bioconjugation (L2, L3 and L4) and of their Gd(III)-complexes (Gd-L2, Gd-L3 and Gd-L4): i) NSuccinimidyl- 3-maleimido propionate (3 eq.) in buffer phosphate 50 mM at pH 7 and CH3CN; ii) N-Succinimidyl-4-formylbenzoate (3 eq.) in buffer phosphate 50 mM at pH 7 and CH3CN; iii) Dibenzocyclooctyne-N-hydroxysuccinimidyl ester (3 eq.) in buffer phosphate 50 mM at pH 7 and CH3CN; iv) GdCl3 in water.

The spacer and the tri-lysine scaffold are expected to ensure a high flexibility within the tetramer structure. Such a flexibility is sought for minimizing steric hindrance issues in regards to the conjugation reaction to targeting vectors. Moreover, flexibility of the MRI label and suitable spacing from the targeting vector are also thought to minimize possible interference in the molecular recognition of the biological target. As a drawback of such flexibility, some limitation to the attainable relaxivity may also be expected. To synthetize precursor **L1**, the Bis-(2-aminoethyl)-ether trityl resin and Fmoc-protection chemistry were chosen for the set-up of solid phase peptide synthesis (SPPS) approach. After coupling the first lysine residue (under the form of N_{α},N_{ε}-di-Fmoc-L-lysine) to the resin, the resin was treated with acetic anhydride in DMF to acetylate the residual free amino groups exposed on its surface, after FMOC deprotection. Then, two more lysine residues were attached. The coupling reactions were performed with 2.5-fold excess Fmoc-Lys(Fmoc)-OH dissolved in DMF with PyBOP and DIPEA as the activators. Every coupling reaction was followed by the removal of Fmoc: that was accomplished by adding piperidine in DMF solution. The branched tri-lysine core anchored on the resin provided four amino groups (two α-amino and two side-chain amino groups) that were used to synthesize the tetrameric AAZTAbased ligand **L1**. The latter

coupling was performed with a small excess of the AAZTA derivative AAZTA(tBu)$_4$C$_4$COOH (Scheme 1), whose synthesis has been described previously (**22**). The coupling reaction between AAZTA and the tri-lysine scaffold turned out to be a tricky step, as the final yield resulted to be strongly dependent upon the activating agent. PyBOP as activator was found to be the most efficient one for such synthetic step. After cleavage from the resin and purification by semi-preparative HPLC, an overall yield of about 60% and purity of 98% of **L1** was obtained. When HBTU was used instead of PyBOP, a decrease of the yield by 30% and a higher amount of a side-product containing only three AAZTA units coupled to the lysine scaffold was found. Such an impurity gave a characteristic signal at 2.90 ppm in 1H NMR spectra (Fig. 1) and characteristic ESI+ MS peaks at m/z 938.6 $[M+2H]^{2+}$ and 625.9 $[M+3H]^{3+}$, corresponding to the molecular formula $C_{81}H_{139}N_{19}O_{31}$.

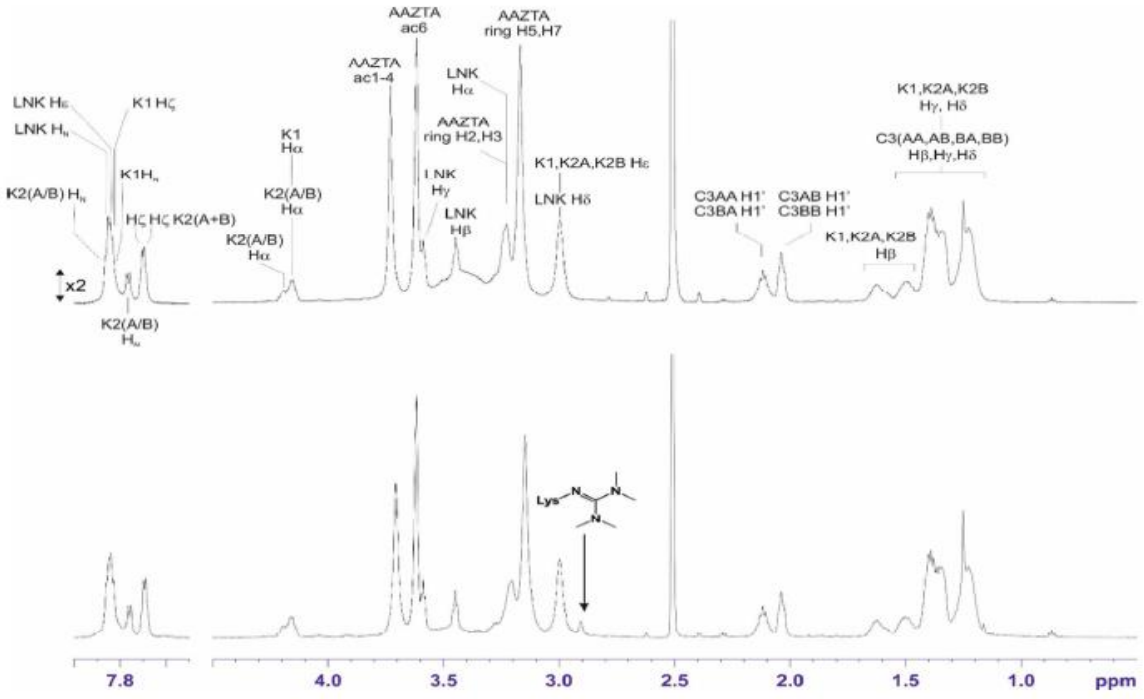

Figure 1. ^{1}H NMR spectrum of L1 synthetized by using PyBOP (top) or HBTU (bottom) as the activator in SPPS, after purification by RP-HPLC. The arrow marks the signal at 2.90 ppm of the side product arising from the transfer of a tetramethyluronium group from HBTU to one lysine, yielding a tetramethylguanidine. NMR spectrum of L1 and atom nomenclature.

This impurity arises from the transfer of a tetramethyluronium moiety from HBTU to the amino group, with the formation of a stable tetramethylguanidine derivative (**25**). Such side reaction is likely favoured by the high density of the amino groups in the tri-lysine scaffold and by the slow rate of coupling of the fourth AAZTA unit due to an increasing steric hindrance. Besides the decrease of the final yield, the formation of such impurity induced problems in the purification step by semi-preparative reverse phase HPLC. The amine end-group in the molecular structure of **L1** was easily converted to maleimide (**L2**), benzaldehyde (**L3**) or cyclooctyne (**L4**) by reacting the **L1** ligand with a

3-fold molar excess of N-Succinimidyl-3-maleimido propionate, or N-Succinimidyl-4-formylbenzoate, or Dibenzocyclooctyne-N-hydroxysuccinimidyl ester, respectively, in phosphate buffer 50mM and CH_3CN 3:1. HPLC-MS (ESI^+) analysis indicated a total conversion of **L1** into the **L2**, **L3** or **L4** compounds. The excess of reagents and salts were removed by size exclusion chromatography, without a significant loss of the product.

Information. The Gd(III) complexes were prepared by mixing stoichiometric amounts (1:4) of the AAZTAtetramer and $GdCl_3$ solution. While this step occurred without any problem for **L1**, **L3** and **L4**, a substantial loss of **L2** may take place because of the hydrolysis of the maleimide group. However, we have found that complete complex formation can be attained, within 1 hour reaction, when the pH is carefully maintained at 6.5 (with the additions of NaOH). Finally, the bifunctional agent has been used to label a fibrin-binding peptide (FibPep). Fibrin is a major component of blood clots and plays an important role in thrombi-related pathologies such as deep venous thrombosis, pulmonary embolism and atherosclerosis. Several examples of fibrin targeted molecular probes have been reported (**26-28**). The primary structure of the FibPep targeting vector is $WQPC^4PWESWTFC^{12}WDPGGGK\text{-}NH_2$, where Cys^4 and Cys^{12} make a disulfide bridge and *N*-Succinimidyl-*S*-acetylthioacetate (SATA) was used for conjugation with **Gd-L2** through the thiol/maleimide chemistry, after deacetylation to free the thiol group. FibPep was reacted with **Gd-L2** at a molar ratio of 1:1 at pH 6.5 to yield the Gd-labelled peptide (**FibPep-Gd-L2**) with 80% yield. It is worth emphasizing that by applying this procedure, Gd-chelates are conjugated to the targeting vector by a one-pot reaction. As opposed to two-step approaches that involve first the conjugation with a chelator and then complexation with gadolinium, the herein presented approach allows to get rid of “free” gadolinium issue (*i.e.* Gd(III) ions being weakly coordinated to the secondary coordinating sites potentially offered by the peptidic structure) (**23,29-31**). The one-pot approach may be particularly useful when the targeting vector has the chemical complexity of proteins, antibodies and polysaccharide-based system, etc.

Relaxivity

The **Gd-L1** complex showed a relaxivity, in water, of 16.4 $mM_{Gd}^{-1}s^{-1}$ (0.5 T, 25°C). It is significantly higher than that of monomeric Gd-AAZTA (7.1 $mM^{-1}s^{-1}$) (**14**), resulting in an overall relaxivity per molecule of 65.6 $mM^{-1}s^{-1}$. The Nuclear Magnetic Resonance Dispersion (NMRD) profile of **Gd-L1** (Fig. 2) as compared to that of Gd-AAZTA shows higher relaxivities throughout all the magnetic field strength studied and a smooth relaxivity peak centered at around 40-50 MHz. This profile is consistent with an increase of the reorientational correlation time, τ_R, expected on the basis of the

increased molecular size due to the tetrameric structure (macromolecule effect). However, the relaxivity is not so high as one could expect on the basis of the size of the tetrameric system. In fact, the observed relaxivity is well below the straight line obtained by plotting the relaxivity of known Gd(III) complexes, with two inner sphere water molecules, versus their molecular weight (Fig. 3).

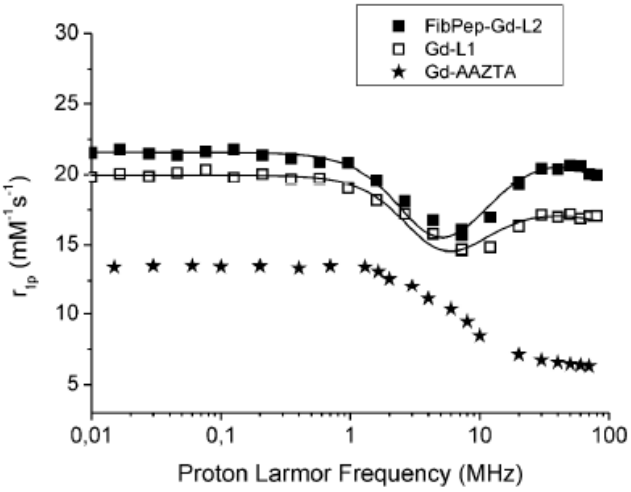

Figure 2. NMRD profiles of Gd-L1 (□) and FibPep-Gd-L2 (■) compared to those of Gd- AAZTA (*). Experimental data points were measured on aqueous solutions of the Gd-complexes at 298 K. Lines are best fitting to the theory. The data refer to 1 mM concentration of gadolinium.

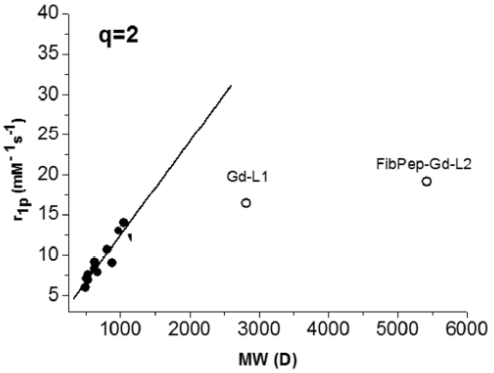

Gd-complex	MW (D)	r_{1p} (0.47T, 25°C)	ref
Gd-DO3A	500	6,0	33
Gd-AAZTA	514	7,1	13
Gd-L1	530	7,6	34
Gd-PCTA[12]	534	6,9	35
Gd-PCTA[12]Bz	625	8,3	36
Gd-L2	629	9,1	34
Gd-BrDO3A	672	7,9	37
Gd-PPDO3A	808	10,7	37
Gd-TREN-Me-3,2 HOPO	880	9,0	38
B25716	974	13,0	39
$(Gd\text{-}AAZTA)_2$	1049	14,0	19
Gd-L1	2820	16,4	this work
FibPep-Gd-L2	5426	19,2	this work

Figure 3. Molecular weight (MW) dependence of the relaxivity (0.47 T, 298 K) for typical Gd(III) complexes with two inner-sphere water molecules. Data points have been interpolated by linear regression: r_{1p}= 0.011MW + 0.928 (r_2= 0.815) (**34-40**)

This can be ascribed to relatively fast internal motions that partially decouple the reorientation of each of the four Gd-AAZTA chelates from the overall global tumbling motion. To get further insights, a quantitative view of the parameters governing the relaxivity of **Gd-L1** has been obtained by multiparametric fitting of the NMRD profile according to the Solomon–Bloembergen–Morgan (SBM) theory for inner sphere paramagnetic relaxation, combined with the Freed theory for outer sphere paramagnetic relaxation (**32**), and modified according to the Lipari-Szabo model-free approach for the description of the rotational dynamics (**33**). This model allows one to take into account the

presence of a certain degree of internal motions superimposed on the overall tumbling motion. These two types of motions, a relatively fast local rotation of the coordination cage, superimposed on the global reorientation of the system, are characterized by different correlation times, namely: τ_{Rl} and τ_{Rg}, respectively. The degree of correlation between global and local rotations is given by the parameter S^2, which takes values between zero (completely independent motions) and one (entirely correlated motions). Such analysis yielded correlation times for both the local and the global motion that are significantly increased as compared to the τ_R value of parent monomeric Gd-AAZTA (74 ps). However, the S^2 value is very low (S^2= 0.068) as a consequence of the great flexibility of the Gd-coordination cages around the linkers that interconnect the four AAZTA chelating units. The relaxivity values of **Gd-L2**, **Gd-L3**, **Gd-L4** were found very similar to that of **Gd-L1.** The relaxivity of **FibPep-Gd-L2,** in water and 25°C, was found to be 19.3 $mMGd^{-1}$ s^{-1} (ca. 80 $mM^{-1}s^{-1}$ per molecule). Upon increasing the temperature, the relaxivity of all the tetramers, decreases as expected on the basis of a shortening of the overall molecular tumbling time. When measured in serum, the observed relaxivities were slightly higher than in water, likely as a consequence of the increased viscosity. More important, on passing from water to serum the absence of any “quenching” of the observed relaxivity indicative of the inability of the endogenous anions (e.g. phosphates, carbonates, etc) to replace the two water molecules in the inner coordination sphere. Thus, the tetrameric derivatives maintain this relevant property of the parent Gd-AAZTA complex.

In conclusion we have presented a protocol for the synthesis of three bifunctional agents, carrying one functional group for bioconjugation to targeting vectors and four Gd-AAZTA like functions as the MRI contrast agent. Despite the high internal flexibility of the Gd(III)-tetramer, the relaxivity per gadolinium shows a 2.4–fold increase as compared to that of monomeric Gd- AAZTA, due to the macromolecule effect. These compounds can be used as building blocks to insert pre-formed, high relaxivity, and high density Gd-centres to biological targeting vectors.

References

1. Schlomka, J., Roessl, E., Dorscheid, R., Dill, S., Martens, G., Istel, T. & Livne, A. (2008).Experimental feasibility of multi-energy photon-counting K-edge imaging in pre-clinical computed tomography. *Physics in medicine and biology*, *53*(15), 4031.

2. Schirra, C. O., Brendel, B., Anastasio, M. A., & Roessl, E. (2014). Spectral CT: a technology primer for contrast agent development. *Contrast media & molecular imaging*, *9*(1), 62-70.

3. Salim, S.-M., Bar-Ness, D., Sigovan, M., Cormode, D. P., Coulon, P., Coche, E., Vlassenbroek, A., Normand, G., Boussel, L., Douek, P. (2017). Review of an Initial Experience with an Experimental Spectral Photon-Counting Computed Tomography System. *Nuclear Instruments and Methods in Physics Research Section A: Accelerators, Spectrometers, Detectors and Associated Equipment*,

4. Caravan, P., Ellison, J. J., McMurry, T. J., & Lauffer, R. B. (1999). Gadolinium (III) chelates as MRI contrast agents: structure, dynamics, and applications. *Chemical reviews*, *99*(9), 2293-2352.

5. Aime, S., Chiaussa, M., Digilio, G., Gianolio, E., & Terreno, E. (1999). Contrast agents for magnetic resonance angiographic applications: 1 H and 17 O NMR relaxometric investigations on two gadolinium (III) DTPA-like chelates endowed with high binding affinity to human serum albumin. *Journal of Biological Inorganic Chemistry*, *4*(6), 766-774.

6. Aime, S., Botta, M., & Terreno, E. (2005). Gd (III)-based contrast agents for MRI. *Advances in Inorganic Chemistry*, *57*, 173-237.

7. Aime, S., Barge, A., Cabella, C., Crich, S. G., & Gianolio, E. (2004). Targeting cells with MR imaging probes based on paramagnetic Gd (III) chelates. *Current pharmaceutical biotechnology*, *5*(6), 509-518.

8. Aime, S., Castelli, D. D., Crich, S. G., Gianolio, E., & Terreno, E. (2009). Pushing the sensitivity envelope of lanthanide-based magnetic resonance imaging (MRI) contrast agents for molecular imaging applications. *Accounts of chemical research*, *42*(7), 822-831.

9. Weissleder, R., & Mahmood, U. (2001). Molecular imaging. *Radiology*, *219*(2), 316-333.

10. Aime, S., Cabella, C., Colombatto, S., Geninatti Crich, S., Gianolio, E., & Maggioni, F. (2002). Insights into the use of paramagnetic Gd (III) complexes in MR-molecular imaging investigations. *Journal of magnetic resonance imaging*, *16*(4), 394-406.

11. James, M. L., & Gambhir, S. S. (2012). A molecular imaging primer: modalities, imaging agents, and applications. *Physiological reviews*, *92*(2), 897-965.

12. Hu, H., Arena, F., Gianolio, E., Boffa, C., Di Gregorio, E., Stefania, R., ... & Aime, S. (2016). Mesoporous silica nanoparticles functionalized with fluorescent and MRI reporters for the visualization of murine tumors overexpressing α v β 3 receptors. *Nanoscale*, *8*(13), 7094-7104.

13. Langereis, S., Geelen, T., Grull, H., Strijkers, G. J., & Nicolay, K. (2013). Paramagnetic liposomes for molecular MRI and MRI-guided drug delivery. *NMR in Biomedicine*, *26*(7), 728- 744.

14. Aime, S., Calabi, L., Cavallotti, C., Gianolio, E., Giovenzana, G. B., Losi, P., ... & Sisti, M. (2004). [Gd-AAZTA]-: a new structural entry for an improved generation of MRI contrast agents. *Inorganic chemistry*, *43*(24), 7588-7590.

15. Baranyai, Z., Uggeri, F., Giovenzana, G. B., Benyei, A., Brucher, E., & Aime, S. (2009). Equilibrium and kinetic properties of the lanthanoids (III) and various divalent metal complexes of the heptadentate ligand AAZTA. *Chemistry-A European Journal*, *15*(7), 1696-1705.

16. Di Gregorio, E., Gianolio, E., Stefania, R., Barutello, G., Digilio, G., & Aime, S. (2013). On the fate of MRI Gd-based contrast agents in cells. Evidence for extensive degradation of linear complexes upon endosomal internalization. *Analytical chemistry*, *85*(12), 5627-5631.

17. Kanda, T., Osawa, M., Oba, H., Toyoda, K., Kotoku, J. I., Haruyama, T., ... & Furui, S. (2015). High signal intensity in dentate nucleus on unenhanced T1-weighted MR images: association with linear versus macrocyclic gadolinium chelate administration. *Radiology*, *275*(3), 803-809.

18. Campa, C., Uggeri, F., Paoletti, S., & Flamigni, A. (2008). *U.S. Patent Application No. 12/528,685*.

19. Gugliotta, G., Botta, M., & Tei, L. (2010). AAZTA-based bifunctional chelating agents for the synthesis of multimeric/dendrimeric MRI contrast agents. *Organic & biomolecular chemistry*, *8*(20), 4569-4574.

20. Gianolio, E., Ramalingam, K., Song, B., Kalman, F., Aime, S., & Swenson, R. (2010). Improving the relaxivity by dimerizing Gd-AAZTA: Insights for enhancing the sensitivity of MRI contrast agents. *Inorganic Chemistry Communications*, *13*(5), 663-665.

21. Baskin, J. M., Prescher, J. A., Laughlin, S. T., Agard, N. J., Chang, P. V., Miller, I. A., ... & Bertozzi, C. R. (2007). Copper-free click chemistry for dynamic in vivo imaging. *Proceedings of the National Academy of Sciences*, *104*(43), 16793-16797.

22. Manzoni, L., Belvisi, L., Arosio, D., Bartolomeo, M. P., Bianchi, A., Brioschi, C., & De Matteo, M. (2012). Synthesis of Gd and 68Ga complexes in conjugation with a conformationally optimized RGD sequence as potential MRI and PET tumor-imaging probes. *ChemMedChem*, *7*(6), 1084-1093.

23. Barge, A., Cravotto, G., Gianolio, E., & Fedeli, F. (2006). How to determine free Gd and free ligand in solution of Gd chelates. A technical note. *Contrast media & molecular imaging*, *1*(5), 184-188.

24. Chaabane, L., Tei, L., Miragoli, L., Lattuada, L., von Wronski, M., Uggeri, F., ... & Aime, S. (2015). In vivo MR imaging of fibrin in a neuroblastoma tumor model by means of a targeting Gd-containing peptide. *Molecular Imaging and Biology: MIB*, *17*(6), 819.

25. Dubey, L. V., & Dubey, I. Y. (2005). Side reactions of onium coupling reagents BOP and HBTU in the synthesis of silica polymer supports. *Ukrainica bioorganica acta*, *1*, 13-19.

26. Costantini, V., & Zacharski, L. R. (1992). The role of fibrin in tumor metastasis. *Cancer and Metastasis Reviews*, *11*(3), 283-290.

27. Caine, G. J., Stonelake, P. S., Lip, G. Y., & Kehoe, S. T. (2002). The hypercoagulable state of malignancy: pathogenesis and current debate. *Neoplasia (New York, NY)*, *4*(6), 465.

28. Zhou, Z., Wu, X., Kresak, A., Griswold, M., & Lu, Z. R. (2013). Peptide targeted tripod macrocyclic Gd (III) chelates for cancer molecular MRI. *Biomaterials*, *34*(31), 7683-7693.

29. De Leon-Rodriguez, L. M., & Kovacs, Z. (2007). The synthesis and chelation chemistry of DOTA–peptide conjugates. *Bioconjugate chemistry*, *19*(2), 391-402.

30. Wu, X., Burden-Gulley, S. M., Yu, G. P., Tan, M., Lindner, D., Brady-Kalnay, S. M., & Lu, Z. R. (2012). Synthesis and evaluation of a peptide targeted small molecular Gd-DOTA monoamide conjugate for MR molecular imaging of prostate cancer. *Bioconjugate chemistry*, *23*(8), 1548-1556.

31. Gringeri, C. V., Menchise, V., Rizzitelli, S., Cittadino, E., Catanzaro, V., Dati, G., & Aime, S. (2012). Novel Gd (III)-based probes for MR molecular imaging of matrix metalloproteinases. *Contrast media & molecular imaging*, *7*(2), 175-184.

32. Lipari, G., & Szabo, A. (1982). Model-free approach to the interpretation of nuclear magnetic resonance relaxation in macromolecules. 1. Theory and range of validity. *Journal of the American Chemical Society*, *104*(17), 4546-4559.

33. Lipari, G., & Szabo, A. (1982). Model-free approach to the interpretation of nuclear magnetic resonance relaxation in macromolecules. 2. Analysis of experimental results. *Journal of the American Chemical Society*, *104*(17), 4559-4570.

34. Aime, S., Botta, M., Crich, S. G., Giovenzana, G., Pagliarin, R., Sisti, M., & Terreno, E. (1998). NMR relaxometric studies of Gd (III) complexes with heptadentate macrocyclic ligands. *Magn. Reson. Chem.*, *36*, S200-S208

35. Gugliotta, G., Botta, M., Giovenzana, G. B., & Tei, L. (2009). Fast and easy access to efficient bifunctional chelators for MRI applications. *Bioorganic & medicinal chemistry letters*, *19*(13), 3442-3444.

36. Aime, S., Botta, M., Geninatti Crich, S., Giovenzana, G. B., Jommi, G., Pagliarin, R., & Sisti, M. (1997). Synthesis and NMR studies of three pyridine-containing triaza macrocyclic triacetate ligands and their complexes with lanthanide ions. *Inorganic chemistry*, *36*(14), 2992-3000.

37. Aime, S., Gianolio, E., Corpillo, D., Cavallotti, C., Palmisano, G., Sisti, M., ... & Pagliarin, R. (2003). Designing Novel Contrast Agents for Magnetic Resonance Imaging. Synthesis and Relaxometric Characterization of three Gadolinium (III) Complexes Based on Functionalized Pyridine-Containing Macrocyclic Ligands. *Helvetica chimica acta*, *86*(3), 615-632.

38. Aime, S., Gianolio, E., Terreno, E., Giovenzana, G. B., Pagliarin, R., Sisti, M., ... & Parker, D. (2000). Ternary Gd (III) L-HSA adducts: evidence for the replacement of inner-sphere water molecules by coordinating groups of the protein. Implications for the design of contrast agents for MRI. *Journal of Biological Inorganic Chemistry*, *5*(4), 488-497.

39. Cohen, S. M., Xu, J., Radkov, E., Raymond, K. N., Botta, M., Barge, A., & Aime, S. (2000). Syntheses and relaxation properties of mixed gadolinium hydroxypyridinonate MRI contrast agents. *Inorganic chemistry*, *39*(25), 5747-5756.

40. Gianolio, E., Cabella, C., Colombo Serra, S., Valbusa, G., Arena, F., Maiocchi, A., & Bardini, P. (2014). B25716/1: a novel albumin-binding Gd-AAZTA MRI contrast agent with improved properties in tumor imaging. *Journal of biological inorganic chemistry*, *19*.

3.2- MRI visualization of Prostate Adenocarcinoma

Based on:
Pagoto A., Stefania R., Tripepi M., Lanzardo S., Longo D., Porpiglia F., Manfredi M., Aime S., Terreno E. *Highly efficient MRI agent to target fibrin/fibronectin complex in Prostate Adenocarcinoma*, In Preparation

Introduction

Prostate Cancer (PCa) is the most frequently diagnosed male tumor in the world and the second male cancer-related cause of death in Europe (**1,2**). Unfortunately, considering the continuous increase of population age, in the near future is expected a sensible increment of the pathology, especially in Western countries (**3**). Nowadays, the evaluation of the blood level of Prostate Specific Antigen (PSA) is considered a good and cheap prognostic marker for PCa (**4**). However, the PSA, which is normally produced by ductal and acinar cells of prostatic epithelium, is not a high reliable marker. This protein is excreted by both cancer cells and hyperplastic cells, in particular in benign prostatic hyperplasia (BPH). Therefore, PSA-related prognosis is not univocal and sometime can force the physician to perform an invasive prostate biopsy, wherein a sample of prostatic tissue is histologically analyzed to confirm the presence of malignant cells (**5**). Therefore, finding more accurate ways to early diagnose PCa is still of enormous relevance. Several specific and low invasive *in vivo* imaging techniques are routinely entered in the clinic to assess the presence of PCa. Ultrasound (US), Nuclear Medicine (in particular Positron Emission Tomography, PET) and Magnetic Resonance Imaging (MRI) are widely used techniques in the hospital to diagnose, locate and, eventually, evaluate recurrence of the tumor. US, in particular the transrectal US (TRUS), is one of the oldest and most exploited imaging modality to visualize PCa. It allows real-time imaging and is really inexpensive, but due to low specificity and sensitivity the resulting image has really limited contrast between cancerous and benign tissue (**6**). PET is more expensive in comparison with US and moreover, the most commonly used tracer FDG is not very accurate. As matter of fact, the coexistence of normal and tumor tissue, the high activity of the nearby bladder and low glycolysis rate of the tumor could interfere with the precise localization of malignant cells (**7**). MRI, in particular multiparametric MRI (mp-MRI) can provide important information. The combination among morphologic (*e.g.* T_2 weighted) and functional (*e.g.* diffusion weighted and dynamic contrast-enhanced) MR images offers a broad characterization of the disease. However, it is necessary to take in account that all these diagnostic tools are very expensive and the cost-benefit ratio is still under scrutiny (**8**). Though high resolution T_2 weighted images have an excellent soft tissue contrast, they are still not very precise for tumor identification. One of the main issue is the difficulty to discriminate between healthy, benign and malignant prostatic tissues. Furthermore, other conditions often associated with the disease (*e.g.* prostatitis, atrophy or hemorrahages) may affect the signal intensity, thus compromising the overall reliability of the diagnosis (**9**). A possible way to overcome these limitations could be to support the T_{2w} images with T_{1w} images acquired after the

injection of PCa-specific molecular MRI agents. Indeed, the use of highly efficient targeted probes that can specifically reach the tumor could directly and uniquely image the tumor tissue.

Among the PCa biomarkers that have been identified so far, we focused our attention to the fibrin/fibronectin complex. It has been demonstrated that the glycoprotein fibronectin (FN) is a hallmark of epithelial-mesenchymal switch that occurs in aggressive forms of PCa, and it is scarcely expressed in BPH (**10**). One of the peculiarity of fibronectin is the ability to form complexes with other proteins from both matrix (*e.g.* collagen) or plasma (*e.g.* fibrin). The presence of fibrin (FB) in the tumor stroma derives from the extravasation of the precursor fibrinogen, caused by leaky neo-formed vessels around the tumor, and its subsequent cleavage by prothrombinase (**11**). The FB/FN complex has been already preclinically validated as cancer biomarker for molecular imaging purposes. The typical strategy to target FB/FN complex (as well as the single components) is through the conjugation of a targeting peptide to the moiety generating the T_1 MRI contrast.

Ye and coworkers were the first to develop a Gd-based agent for targeting FB/FN complex (**12**). The probe consisted of a monoamide Gd-DTPA cage conjugated with the cyclic decapeptide CLT1 (**13**) Though *in vivo* competitive experiments demonstrated the effective targeting of the probe in a mouse model of colon cancer, the observed T_1 contrast in the tumour was only slightly higher than the result obtained with the clinically approved agent gadodiamide used as control. Certainly, the relatively low relaxivity of the targeting complex (4.2 $s^{-1}mM^{-1}$ at 3 T) was one of the reasons for the limited *in vivo* performance. To overcome this limitation, the same research team lately developed a nanoglobular dendrimeric agent containing more Gd-units (*ca.* 20) (**14-16**), with a consistent relaxivity enhancement (11.6 $s^{-1}mM^{-1}$ at 1.5 T) (**15**) and a consequent improvement in the *in vivo* detection upon the administration of a lower dose of agent (30 μmol_{Gd}/kg bw *vs* 100 μ mol_{Gd}/kg bw) in several mouse tumor models including orthotopic PCa. However, the low water solubility of CLT1 vector was an important limitation of its potential and prompted the search for more promising vectors for targeting FB/FN complex.

Zhou and colleagues conjugated the more soluble pentapeptidic vector CREKA (**17**) to a tripodal trimeric Gd-DOTA-monoamide-like structure (**18**). The relaxivity (per Gd ion) of such a probe (7.34 $s^{-1}mM^{-1}$ at 1.5 T) is the two CLT1-based agents described above, and the presence of three Gd centers per molecule allowed a good *in vivo* tumour MRI detection in a mouse model of breast cancer using a standard dose (100 μmol_{Gd}/kg bw). Following this rationale, the same research group in a successive work increased to four the number of paramagnetic center in the molecule (**19**). The consequent enhancement in the relaxivity per Gd (8.3 $s^{-1}mM^{-1}$ at 3 T and 37°C), further amplified by

the increased number of metal ions in the molecule, allowed the PCa visualization in a mouse model after the injection of a low dosage of the agent (30 μmol_{Gd}/kg bw).

On this basis, we conjectured that a further significant improvement in the contrast detection threshold could be reached by replacing the Gd DOTAMA tetrameric structure with a more efficient GdAAZTA-like unit. It is a coordination cage able to form a Gd complex with higher relaxivity and good thermodynamic stability and kinetic inertness (*i.e.* the *in vivo* safety) of the metal complex. A very suitable candidate is the heptadentate ligand AAZTA (6-amino-6-methylperhydro-1,4-diazepinetetraacetic acid), whose Gd(III) complex has a high relaxivity value (7.1 $mM^{-1}s^{-1}$ at 0.5 T and 25°C) due to the presence of two fast exchanging water molecules in the inner coordination sphere of the metal (**20**).

Then, we designed an AAZTA-based FB/FN-targeted agent using the same synthetic strategy followed in Chapter 3.1, in which four Gd-complexes were conjugated to the CREKA peptide lysine as branching moiety. This chapter reports the synthesis of the agent (CREKA-dl-(Gd-AAZTA)$_4$, and its preclinical validation on a orthotopic mouse model of prostate cancer using an analogous probe conjugated with the scrambled peptide KAREC (KAREC-dl-(Gd-AAZTA)$_4$) as untargeted control (**19**). Besides the specific application in PCa diagnosis, this agent represents the first example that illustrates the advantages associated with the use of an AAZTA-based Gd-agent in targeted molecular imaging MRI.

Experimental Procedures

Synthesis of CREKA and KAREC peptides

CREKA and KAREC peptides were synthesized by Fmoc Solid Phase Peptide Synthesis (SPPS) using 2-chlorotrityl chloride resin (0.19 mmol). The resin was loaded into a reaction vessel, swollen with DCM for about 10 minutes and then washed with DMF. A mixture of Fmoc-Ala-OH (0.76 mmol) and DIPEA (1.52 mmol) in DMF (10 mL) was added in the reactor and the suspension was shaken for 2.5 h. Three further washing steps with DCM and MeOH followed. Afterwards, a mixture of MeOH/DIPEA (6:1,v/v) was added, and after shaking for 30 minutes, the product was washed with DCM, MeOH and Et_2O. The next amino acids were sequentially added, after piperidine mediate (20% v/v in DMF) Fmoc protecting group removal, following this order: Fmoc-Lys(Boc)-OH (0.475 mmol; 223 mg), Fmoc-Glu(OtBu)-OH (0.475 mmol; 202 mg), Fmoc-Arg(Pbf)-OH (0.475 mmol; 308 mg) and Fmoc-Cys(trt)-OH (0.475 mmol; 278 mg), for the CREKA targeting peptide. Each reaction cycle was followed by extensive washing with DMF.

The resin was finally washed with DMF/DCM and was dried with Et_2O. The cleavage from the dried resin was pursued with a cleavage cocktail solution of TFA (trifluoroacetic acid)/Water/Phenol/TIS (tryisopropylsilane) (95:1:2:2, v/v) for 2 hours at room temperature. The filtered solution was dropped to cold Et_2O and the solid product was collected by centrifugation after five washing with Et_2O.

ESI-MS (m/z) for CREKA: $[M+H]^+$ 606.45 (obsd.), 606.30 (calcd. for $C_{23}H_{43}N_9O_8S$); $[M+2H]^{2+}$ 303.71 (obsd.), 303.65 (calcd.).

ESI-MS (m/z) for KAREC: $[M+H]^+$ 606.51 (obsd.), 606.30 (calcd. for $C_{23}H_{43}N_9O_8S$); $[M+2H]^{2+}$ 303.80 (obsd.), 303.65 (calcd.).

The crude products were dissolved in H_2O and purified by preparative HPLC using a Waters XBridge BEH300 prep C18 10 µm 10x100 mm column. The product was fractioned, collected, freeze-dried overnight, and then characterized by analytical HPLC using a Waters XBridge BEH300 C18 3.5 µm 4.6x150 mm column.

Synthesis of CREKA-dL-(Gd-AAZTA)$_4$ and KAREC-dL-(Gd- AAZTA)$_4$

The peptide (CREKA or KAREC, 5 µmol) was dissolved in acetate buffer 0.1 M (0.3 mL) and then added to 5 mL of a solution of Mal-dL-(Gd-AAZTA)$_4$ synthesized according to the procedure described elsewhere (**21**). The reaction occurred in 45 minutes under inert atmosphere (checked by mass spectrometry) and the final solution was desalted using PD-10 column Sephadex G-25.

ESI-MS (m/z) for CREKA-dL-(Gd-AAZTA)$_4$: $[M-3H]^{3-}$ 1192.51 (obsd.), 1192.36 (calcd. for $C_{124}H_{192}Gd_4N_{30}O_{51}S$); $[M-4H]^{4-}$ 894.08 (obsd.), 894.02 (calcd.).

ESI-MS (m/z) for KAREC-dL-(Gd-AAZTA)$_4$: $[M-3H]^{3-}$ 1193.04 (obsd.), 1192.36 (calcd. for $C_{124}H_{192}Gd_4N_{30}O_{51}S$); $[M-4H]^{4-}$ 893.94 (obsd.), 894.02 (calcd.).

Relaxometric characterization of CREKA-dL-(Gd-AAZTA)$_4$ and KAREC-dL-(Gd- AAZTA)$_4$

The longitudinal water protons relaxation rate was measured by using a Stelar Spinmaster spectrometer (Stelar, Mede, Pavia, Italy) operating at 0.5 T (21.5 MHz Proton Larmor Frequency), by mean of the standard inversion-recovery technique. The temperature was controlled with a Stelar VTC-91 air-flow heater equipped with a copper constantan thermocouple.

The proton $1/T_1$ NMRD (Nuclear Magnetic Relaxation Dispersion) profiles were measured at 25°C on a fast field-cycling Stelar relaxometer over a continuum of magnetic field strengths from 0.00024 to 0.47 T (corresponding to 0.01-20 MHz proton Larmor Frequency). The relaxometer operates under computer control with an absolute uncertainty in $1/T_1$ of ± 1%. Additional data points in the range

21.5-70 MHz were obtained on a manually tunable Stelar Spinmaster spectrometer. Data were fitted to the conventional Solomon-Bloembergen-Morgan theory.

***In vitro* binding studies with fibrin clots**

Artificial fibrin clots were prepared and used to test the targeting property of the MRI agents *in vitro*. Clots were prepared starting from FFP (Fresh Frozen Plasma) using a 96-well plate. FFP (90 µL), $CaCl_2$ (5 µL - 0.4 M), and thrombin (5 µL - 0.1 U/ ml) were added to each well and then the plate was incubated at 37 °C for 90 min. Subsequently, solutions containing CREKA-dL-(Gd-AAZTA)$_4$, KAREC-dL-(Gd-AAZTA)$_4$, or peptide-free dL-(Gd-AAZTA)$_4$ (from 1 to 100 µM of Gd^{3+}) were added to each well, and incubated at 37 °C for 60 min. After incubation, the clots were then washed five times using PBS buffer (0.01 M pH7.4), collected, and digested in nitric acid (1 mL) for ICP-MS analysis.

PC3 cell line

Human PC3 cells were cultured in DMEM F-12 medium (Euroclone, Italy) supplemented with 10% fetal calf serum (FBS) (Lonza, Belgium), 1% penicillin/streptomycin antibiotics (100 U/mL penicillin, 0.1 mg/mL streptomycin; Lonza, Belgium) and 2 mM of glutamine (Lonza, Belgium). Cells were grown in T175 culture flasks (Termofisher, Denmark) at 37°C in a humidified atmosphere containing 5% CO_2. Cells were passaged using a trypsin-ethylenediaminetetraacetic acid (EDTA) solution (Lonza, Belgium), 170000 UI/L trypsin/versene and 200 mg/L EDTA. Cells were grown to near confluence and were than harvested and counted. Cells were suspended in phosphate-buffered saline (PBS) prior the *in vivo* orthotopic injection.

Orthotopic mouse model of prostate cancer

6-8 weeks old athymic nude male mice with a weight between 20 and 25 g were enrolled in the study. Tumor induction protocol required the subcutaneous administration of an analgesic (Rymadil®, 5 mg/kg) one hour before the procedure. The animals were anesthetized in the induction chamber, then transferred to the floor, and arranged adequately for orthotopic implantation. Lidocaine was applied in the intervention area as local anaesthetic. The inoculation procedure started with the disinfection of the lower abdomen with Betadine®, followed by incision of about 12-15 mm along the central line, 3-4 cm above the urinary orifice. The prostate was exposed and the adjacent adipose tissue momentarily removed. A suspension containing 1.5 x 10^6 cells (suspended in 30 µL) of the prostate tumour cells PC-3 were injected with a microsyringe into one of the two ventral lobes of the prostate. Muscle and skin layer are sewn with sterile absorbable wire

and the wound cleaned with Betadine®. Upon awakening, the animals were placed and allowed to recover. Rymadil® was again administered at least once, 24 hours after surgery.

Immunohistochemical characterization of the tumor model

Double indirect staining for detection of fibrin and fibronectin were performed. Frozen sections (5 µm thick) of the PC3 tumors (4 weeks post cells injection) were cut with a cryostat (Leica CM 1950) and then fixed with acetone at room temperature. Three washing cycles with PBS were carried out. Then, sections were incubated for 1 h with 10% BSA (Bovine Serum Albumin) in PBS. Subsequently, the two primary Ab anti-fibrin (ab34269, Abcam) and anti-fibronectin (sc-6952, Santa Cruz) were incubated at 4 °C (diluted respectively 1:200 and 1:100 in PBS containing 10% BSA) overnight. After three washings with PBS, sections were then incubated for 60 min with rhodamine-tagged goat antirabbit IgG (R6394, Invitrogen) (1:1000 dilution in PBS) and FITC-tagged bovine antigoat IgG (sc-2348, Santa Cruz) at room temperature. After washings with PBS, sections were stained with Hoechst (33342, Sigma) (1:10000 dilution in PBS) for nuclear staining. After quick (5 min) washing in bidistilled water, the sections were mounted with ProLong (ThermoFisher) antifade mountant. Microscopic observation and image acquisition were performed with APOTOME (Zeiss)

***In vivo* MRI experiments and data analysis**

The MRI study was performed on a Bruker Biospec 7 T scanner (Bruker Biospin, Germany) with a volume radio frequency (RF) coil. Mice were anesthetized by intramuscular injection of a mixture of tiletamine/zolazepam (Zoletil 100, Virbac, Italy) 20 mg/kg and xylazine (Rompun; Bayer, Italy) 5 mg/kg. The tail vein of the mouse was catheterized with a 30-G needle connected with a 1.5 m long tubing filled with heparinized saline. A group of 5 mice bearing orthotopic PC-3 prostate cancer was used for each experiment. T_2-weighted images were acquired to localize the tumour region and then T_1-weighted pre-injection MRI images were performed. Afterwards, the targeted agent or control agents were injected at a dose of 20 µmol Gd/kg. T_1-weighted 2D axial images were acquired at different time points up to 45 minutes after administration of the contrast agent. The targeting agent (20 µmol Gd/kg of CREKA-dL-(Gd-AAZTA)$_4$) was also administered to a group of healthy mice (n = 5) .

The following parameters were used for the acquisition of the T_1-weighted images (Multi-Slice Multi-Echo sequence): TR/TE = 2000/3.5 ms, FOV = 3.5 cm, slice thickness = 1 mm, slice number = 11; average = 6; matrix = 128x128.

The following parameters were used for the acquisition of the T_2-weighted images (Rapid Acquisition with Relaxation Enhancement, RARE sequence): TR/TE = 4000/36 ms, FOV = 3.5 cm, slice thickness = 1 mm, slice number = 11; average = 6; matrix = 128x128.

The T_1 contrast parametric images were obtained using a customized script in Matlab (Mathworks). In brief, the T_1contrast enhancement $\left(T_{1\ (t)}^{enh}\right)$ was calculated voxel-by-voxel for each slices and for all chosen time points as follows:

$$T_{1\ (t)}^{enh} = \frac{S_{(t)}^{POST} - S^{PRE}}{S^{PRE}}$$

Where S^{PRE} and $S_{(t)}^{POST}$ represent the average signal intensity before and after (respectively) the injection of the contrast agent, both normalized for the reference tube containing 0.5 mM of the clinically approved MRI agent gadoteridol. *p* values were calculated using Student's t-test, assuming statistical significance at $p < 0.05$.

Image analysis was performed using the open-source ImageJ software. Regions of interest (ROIs) were firstly manually drawn over the tumour in the axial T_2 anatomical images. The same ROIs were then used to define the tumour on T_1 contrast parametric images obtained with Matlab script. Extrapolating the average signal intensity from each ROI, was finally possible to calculate the signal belonging to the tumour for each time point.

Evaluation of the plasmatic half-life of CREKA-dL-(Gd-AAZTA)$_4$

The plasmatic half-life of the targeting agent was evaluated in healthy mice. A dose of 20 µmol of Gd/kg bw was injected in the tail vein and then blood was collected in heparin at different times post-injection (5 min, 15 min, 30 min, 60 min, 120 min, 240 min, 360 min and 1440 min). Blood samples were then mixed with ultra-pure nitric acid (1 mL) and liquefied for 1 week. The Gd(III) concentration in the solution was measured by ICP-MS. The Gd(III) content was calculated as µg of Gd(III) per gram of blood (µg Gd/g).

***Ex vivo* biodistribution of the MRI agents**

The targeting CREKA-dL-(Gd-AAZTA)$_4$ probe and the two control probes KAREC-dL-(Gd-AAZTA)$_4$ and dL-(Gd-AAZTA)$_4$ were injected in tumour bearing mice (n = 3 for each probe) and sacrificed 12 min and 24 h post-injection. Organs and tissue samples including liver, spleen, kidneys, muscle, bladder and tumour were collected and weighed. The tissue samples were mixed with ultra-pure nitric acid (3 mL for the liver and 1 mL for the other samples) and liquefied for 1 week. The Gd(III) concentration

in the solution was measured by ICP-MS. The Gd(III) content was calculated as μg of Gd(III) per gram of tissue (μg Gd/g).

Results

Synthesis and Characterization of tetrameric probes

The pentapeptide CREKA and its scrambled version KAREC, already used as control peptide for imaging purposes (**18,19,22**), was synthetized by solid phase synthesis with high yield (85%) and purity (83%). Both peptides were designed to expose a terminal cysteine residue in order to use the free thiol group for the conjugation to the reactive maleimide moiety of Mal-dL-(Gd-AAZTA)$_4$ (Scheme 1). CREKA-dL-(Gd-AAZTA)$_4$ and its control KAREC-dL-(Gd-AAZTA)$_4$ were obtained under inert conditions with a yield of higher than 90%. The reaction was monitored by LC-MS and the product was purified by preparative HPLC. The relaxivity of the tetrameric compound is 14.0 $mM_{Gd}^{-1}s^{-1}$ at 37°C and 1.5 T, a value c.a. 70 % higher than the tetrameric analogue containing four Gd-DOTA units (**19**). The NMRD profiles (at 25°C) of the targeting agent, the unconjugated complex dL-(Gd-AAZTA)$_4$*, and the monomer Gd-AAZTA are reported in* Figure 1A. The profiles of both the tetrameric agents are characterized by a relaxivity hump at Larmor frequencies higher than 10 MHz as a consequence of the slower molecular tumbling of the complex. The data were analyzed according to the classical Solomon-Bloembergen-Morgan relaxation model that considers the relaxivity as the sum of the contribution arising from: i) protons of the water molecules coordinated to the Gd(III) ion (two water molecules in this case), and ii) outer sphere water protons diffusing around the chelate (**23**).

Table 1 reports the relevant relaxation parameters obtained from the analysis of the NMRD profiles as well as the corresponding value published for the monomer Gd-AAZTA (**20**). The results obtained clearly indicate that the reorientational correlation time τ_R is the only parameter affected by the tetramerization of Gd-AAZTA, whereas the dynamic parameters related to the electronic relaxation time (Δ^2 and τ_V) and the water exchange lifetime τ_M are almost unchanged with respect to the monomer Gd-AAZTA.

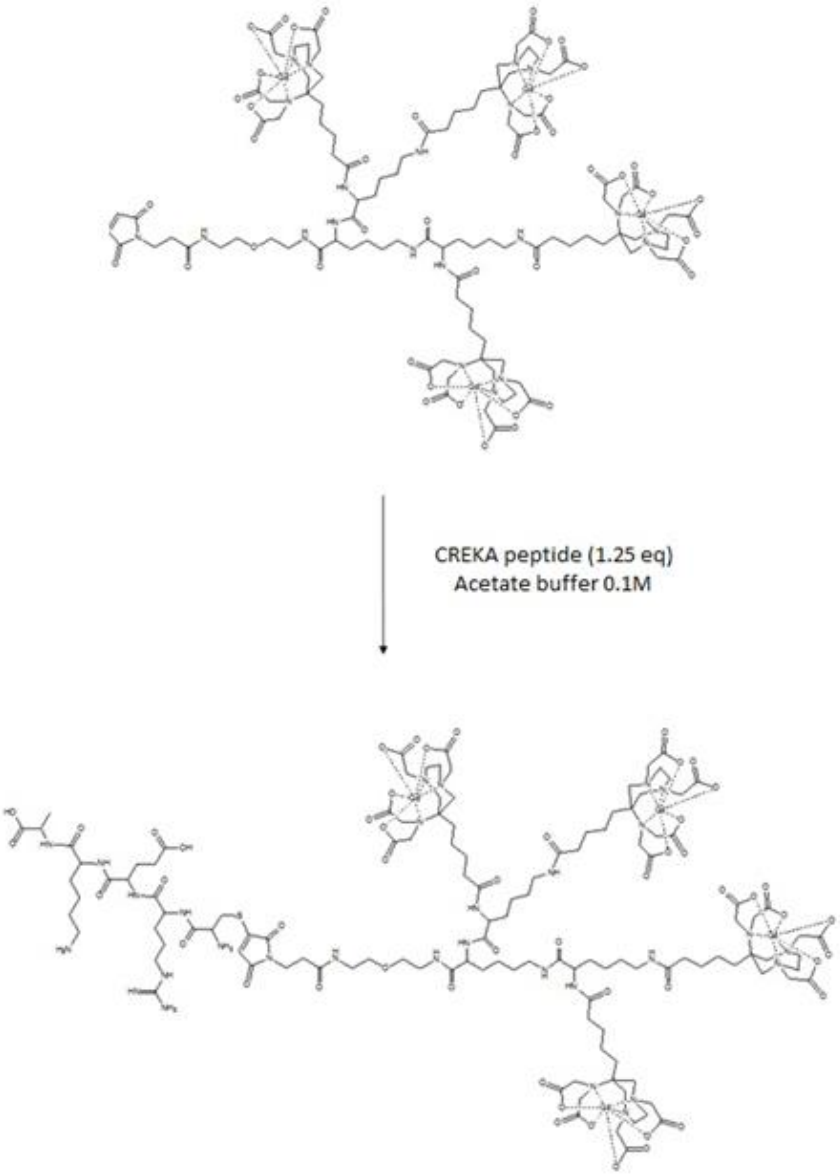

Scheme 1. Synthetic scheme to CREKA-dL- (Gd-AAZTA)$_4$ and KAREC-dL- (Gd-AAZTA)$_4$

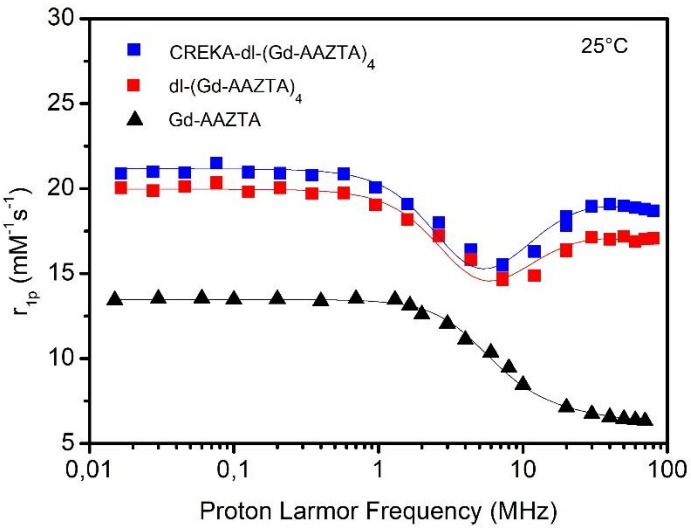

Figure 1. NMRD profiles of CREKA-dL-(Gd-AAZTA)$_4$, dL-(Gd-AAZTA)$_4$ and peptide free Gd-AAZTA at 25°C acquired from 0.01 MHz to 100 MHz

System	r_1 ($mM^{-1}s^1$)[a]	Δ^2 (s^{-2})[b]	τ_V (ps)[c]	τ_l (ps)[d]	τ_g (ps)[e]	S^2	τ_r (ps)[f]	n_{ss}
Gd-AAZTA	7.1	1.87×10^{19}	33.6	-	-	-	69.1	2
dL-(Gd-AAZTA)$_4$	17.3	1.89×10^{19}	36.4	308	740	0.27	-	2
CREKA-dL-(Gd-AAZTA)$_4$	18.2	1.78×10^{19}	36.5	327	872	0.29	-	2

Table 1. Main relaxometric parameters derived from fitting of NMRD profiles reported in figure 1.
On carrying out the fitting procedure, some parameters were fixed to reasonable values: r_{Gd-H} (distance between Gd and protons of the inner sphere water molecule) = 3.1 Å; a (distance of minimum approach of solvent water molecules to Gd^{3+} ion) = 3.8 Å; D (solvent diffusion coefficient) = $2.2\cdot10^{-5}$ cm^2 s^{-1}. [a] Measurement achieved at 25°C and 0.5 T. [b] Squared mean transient zero-field splitting (ZFS) energy. [c] Correlation time for the collision-related modulation of the ZFS Hamiltonian. [d] Local reorientational correlation time. [e] Global reorientational correlation time. [f] Reorientational correlation time

In vitro evaluation of CREKA targeting on fibrin clots

The affinity of CREKA-dL-(Gd-AAZTA)$_4$ towards its natural target was evaluated *in vitro* on fibrin clots. The experiment was performed by measuring the amount of Gd(III)-complexes (with or without the peptidic vector) bound to the clot as a function of the added complex. The quantitative results showed a stronger interaction of the targeting probe with respect to the control ones, though an aspecific binding was partially observed. Nevertheless, considering the maximum incubated Gd(III) concentration (100 µM), the amount of targeted agent bound to the clot was two-fold higher than the control (Figure 2).

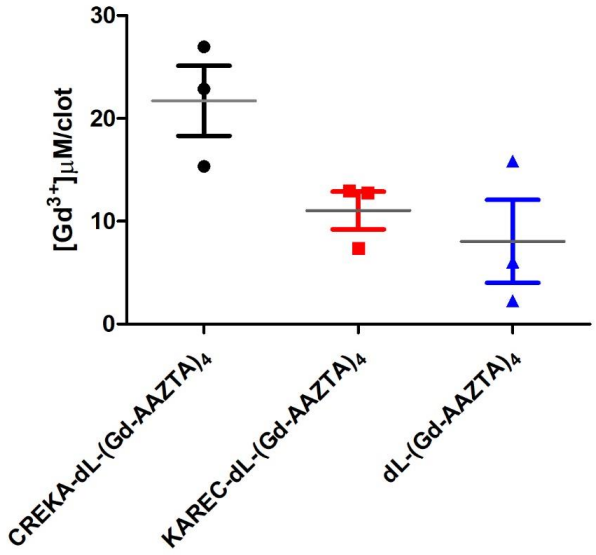

Figure 2. Interaction on fibrin clot of CREKA-dL-(Gd-AAZTA)$_4$ in comparison with controls at the concentration of 100 µM [Gd^{3+}]

Immunofluorescence for the fibrin-fibronectin complex

The association between cancer and coagulation system is well known (**24,25**), as well as the deposition of fibrin in prostate cancer (**26**) and the formation of complex between fibrin and resident fibronectin (**27**). To confirm the presence of the targets in the orthotopic model of PCa, immunofluorescence for fibrin and fibronectin was performed on frozen tissue. In the tumour extracellular matrix is possible to identify the molecules, with a visible partial colocalization, which confirms the presence of the target (Figure 3).

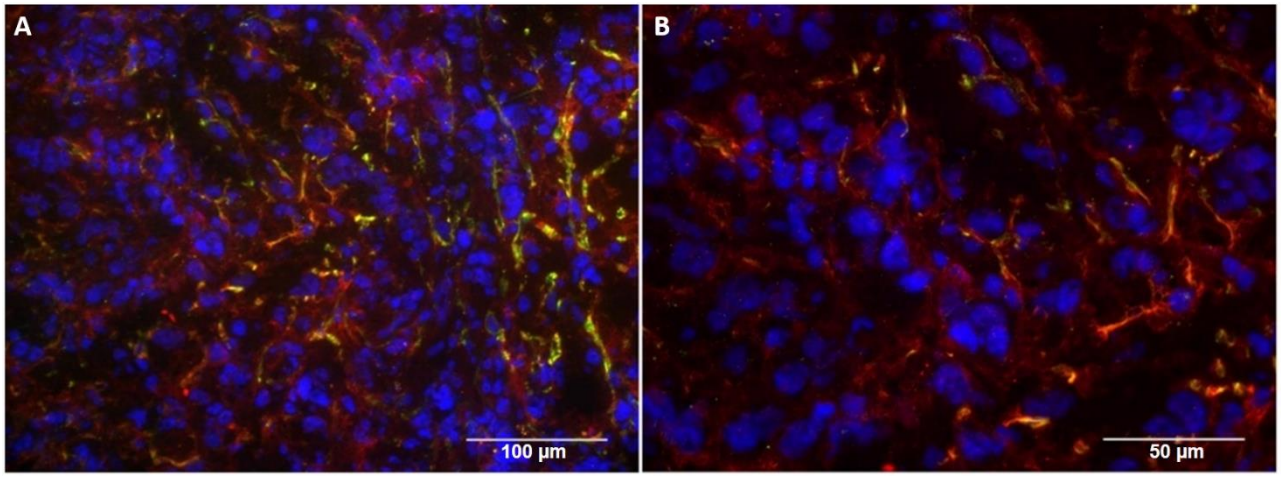

Figure 3. *Immunofluorescence 20X (A)and 40X (B) of fibrin (green) –fibronectin (red) in orthotopic PC3 model*

In vivo MRI experiments in mice bearing PC3 orthotopic tumors

The MRI performance of CREKA-dL-(Gd-AAZTA)$_4$ was tested on the orthotopic PC-3 tumor mouse model at 7 T. Figure 4 shows representative T_2-weighted (Figure 4A) and T_1-weighted axial MR images of mice bearing PC-3 prostate cancer before (Figure 4B) and after (Figure 4C) the injection of CREKA-dL-(Gd-AAZTA)$_4$ at a dose of 20 µmol$_{Gd}$/kg. The images obtained within 45 min post-injection of the probes were processed by a custom Matlab script, giving the parametric maps of the T_1 contrast distribution in the mice. Region of Interests (ROIs) were drawn in the tumour region and the contrast enhancement was calculated in comparison with the T_{1w} pre-contrast image. The contrast distribution was analysed also for the controls: KAREC-dL-(Gd-AAZTA)$_4$ (scrambled peptide) and dL-(Gd-AAZTA)$_4$ tetramers. The overall results are shown in Figure 5: statistically significant differences between CREKA and controls were visible within 10 min post-injection in the tumor core, where the contrast enhancement reached a 40% value. The specific accumulation of CREKA-dL-(Gd-AAZTA)$_4$ is also clearly visible by comparing the T_1-contrast observed in diseased and healthy prostate (Figure 5).

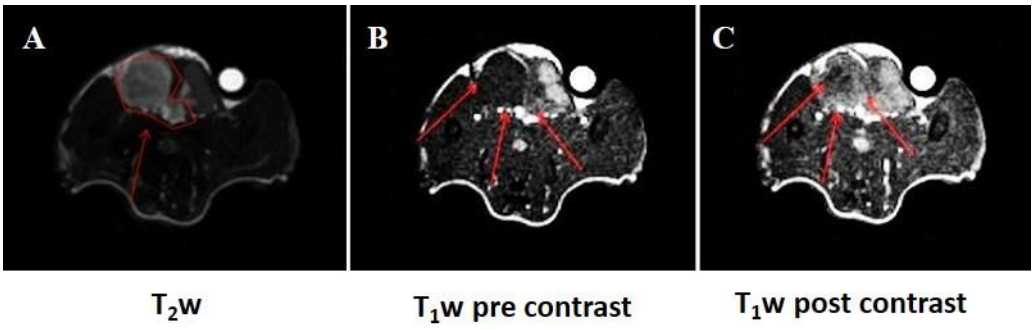

Figure 4. *7T MRI images of prostate cancer in mouse. A) T_2-weighted image achieved to localize the tumor region (circled in red); B) T_1-weighted image before injection of the CREKA-dL-(Gd-AAZTA)$_4$; C) T_1-weighted image at 12 minutes showing the maximum contrast enhancement in the tumor region (red arrows).*

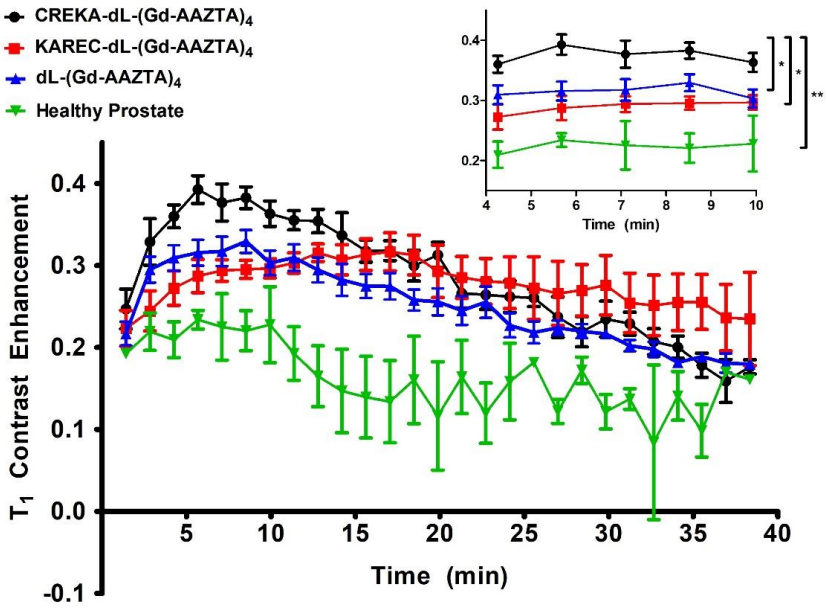

Figure 5. *T_1 contrast enhancement followed in time after injection of CREKA-dL-(Gd-AAZTA)$_4$ (black) , KAREC-dL-(Gd-AAZTA)$_4$ (red) and dL-(Gd-AAZTA)$_4$ (blue) in mice bearing orthotopic PC-3 prostate cancer and in healthy mice after injection of CREKA-dL-(Gd-AAZTA)$_4$ (green). ** p <0.01 - * p < 0.05*

The MRI contrast measured in the tumor rim is strongly influenced by the accumulation of the probes in the bladder, which can be partially invaded by the lesion. Furthermore, as the agent is excreted by kidneys, the bladder accumulation of the probe generated a very bright signal that can make difficult the accurate detection of the tumour contrast. The distribution of the T_1 contrast in the parametric map allowed the clear visualization of the bladder swelling, starting 45min post injection of the CREKA-dL-(Gd-AAZTA)$_4$ (Figure 6D and 6E).

To evaluate the probe distribution in the principal excretory organs, the amount of Gd(III) was determined by ICP-MS on selected explanted organs 10 min and 24 h post injection. The agent is mainly excreted by kidneys (Figure 7), and it was almost completely eliminated 24h after injection. The very fast washout of the targeting agent from the body is confirmed by the very short blood half-life value (20min) (Figure 8).

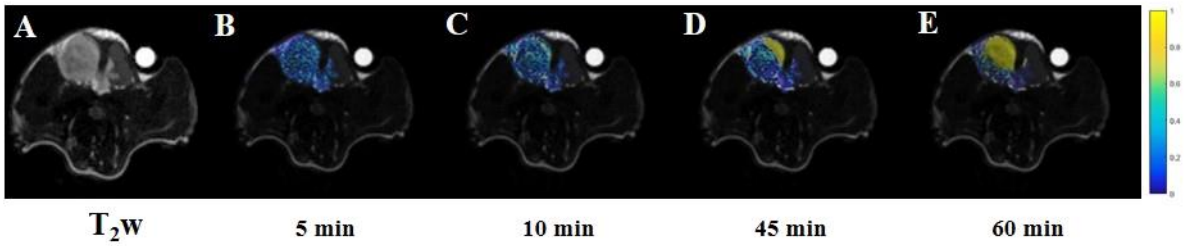

Figure 6. *In vivo* T1 map of contrast distribution in orthotopic PC3 model after injection of CREKA-dL-(Gd-AAZTA)$_4$

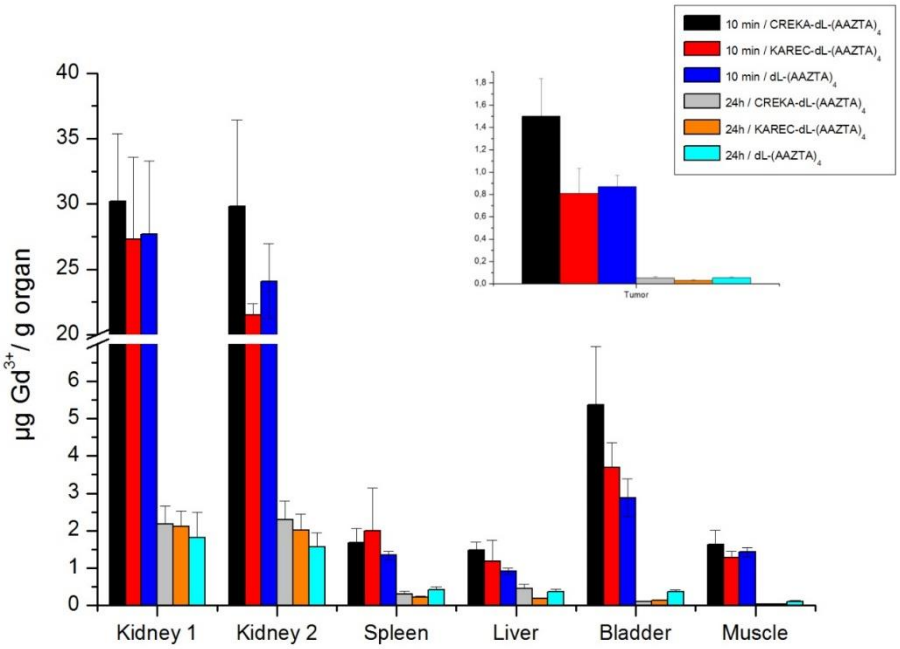

Figure 7. Ex vivo Gd(III) quantification in tissues, 10 min and 24h post injection of CREKA-dL-(Gd-AAZTA)$_4$ and control probes

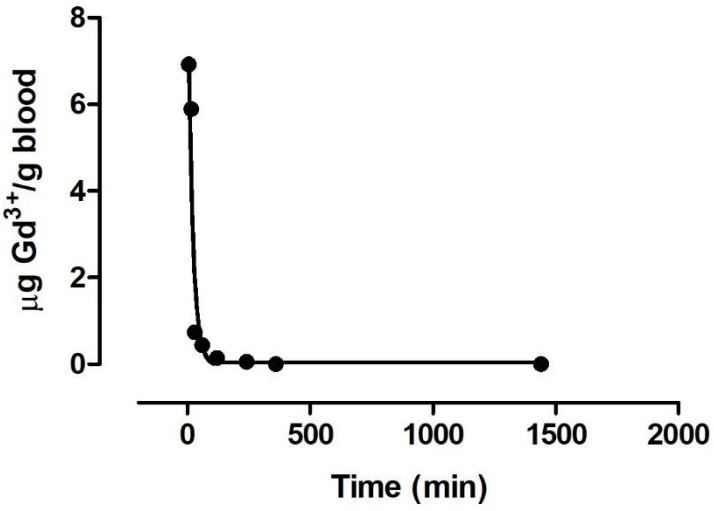

Figure 8. Ex vivo blood half-life of *CREKA-dl-(Gd-AAZTA)$_4$*

Discussion

In this work, a new and highly efficient Gd-based MRI probe that actively recognize fibrin/fibronectin complex, an extracellular marker of prostate cancer, was developed. The presence of a newly formed extracellular matrix and leaky vessels is associated with prostate cancer progression (**28**), and this feature can be useful for molecular MRI purposes. The combination of an efficient MRI contrastophore associated with a possibly highly abundant molecular target, is a way to overcome the relatively poor sensitivity of MRI. The herein proposed CREKA-dL-(Gd-AAZTA)$_4$, based on the targeting peptide CREKA, already reported as vector for molecular imaging purposes, is a versatile molecule with no evident toxicity, high water-solubility, and fast renal excretion. Moreover, the complex has a very high molecular relaxivity (72.8 $mM^{-1}s^{-1}$ per molecule at 25°C and 0.5 T) as the result of the conjugation of four Gd-AAZTA chelating agents. Considering that the relaxivity of a single Gd-AAZTA unit is 7.1 $mM^{-1}s^{-1}$, each unit of the tetramer displays a relaxivity enhancement more than two- fold higher (18.2 $mM^{-1}s^{-1}$, 25°C, 0.5 T). This is an important improvement, mostly due to the elongation of the reorientational correlation time of the system, consequent to the increased molecular weight of the multimeric probe. In comparison with similar probes based on DOTA or DTPA, the overall relaxivity reached a significant increment, bringing to a drastic reduction of the injected dose (0.02 $mmol_{Gd}$/kg), with respect to the commercial agents used in clinics (0.1 $mmol_{Gd}$/kg) (**29**), thus further minimizing the possible side effects associated with the use of Gd(III)-based contrast agents (**30**).

The targeting performance of CREKA-dL-(Gd-AAZTA)$_4$ was initially tested in vitro on artificial fibrin clots, despite the interaction of the peptide with extracellular targets is well established. (**18,19,22,31,32**). The targeted complex was then tested *in vivo* on an orthotopic PC3 tumor mice, an experimental model that is known to express the fibrin/fibronectin complex. The tumor T_1 contrast after the injection of the targeted agent was significantly higher than the untargeted scrambled, but only within the first 10 min post injection. The tumor accumulation of the agent, in agreement with the literature data reported for similar probes (**18,19**), were also confirmed by the determination of the concentration of Gd ion in the prostate. Furthermore, the active accumulation of the CREKA-dL-(Gd-AAZTA)$_4$ in the tumor was indirectly confirmed by its low accumulation in the healthy tissue.

The very rapid tumor washout of the targeting probe could be the consequence of the relatively weak binding of the agent to the extracellular target. For this reason, this phenomenon can be referred as a sort of “delayed diffusion”. The agent was quickly excreted by kidneys and therefore, it accumulated in bladder, as it was already reported for small molecule with similar negatively

charge of our targeting probe (**33**). The reduced persistence of the probe in the body could be an advantage because it would limit possible collateral phenomena associated with the long-term accumulation of Gd-based agents. On the other side, this rapid bladder excretion could be also considered a drawback for an accurate tumor delineation. In fact, the two organs are spatially linked and the probe accumulation in the bladder, with consequent swelling, could interfere with the MRI detection of the tumor margins.

In conclusion, this chapter reports the synthesis and the development of a new and highly efficient Gd-based T_1-MRI probe to detect prostate cancer. The probe, CREKA-dL-(Gd-AAZTA)$_4$, is inserted in a very wide literature contest, continually in progress, of targeting agents that specifically bind extracellular molecules resident in the tumor stroma. The agent shows an higher relaxivity than similarly sized molecules already reported in literature, and this could mean a higher *in vivo* contrast possibly using a very low dose (20µmol$_{Gd}$/kg *vs* 100µmol$_{Gd}$/kg generically used for clinic purposes). This characteristic, nowadays relevant with the recent discovery of possible side effects associated with long-term accumulation of Gd(III) in humans, will be even more predominant in future. Our research pave the way for new form of clinic MRI diagnosis, based on the precise localization of prostate tumor exploiting highly specific and efficient targeted T_1 agents.

References

1. Sarkar, S.; Das, S., A Review of Imaging Methods for Prostate Cancer Detection. *Biomed Eng Comput Biol* 2016, *7* (Suppl 1), 1-15.

2. Pentyala, S.; Whyard, T.; Pentyala, S.; Muller, J.; Pfail, J.; Parmar, S.; Helguero, C. G.; Khan, S., Prostate cancer markers: An update. *Biomedical reports* 2016, *4* (3), 263-268.

3. Sharma, S.; Zapatero-Rodriguez, J.; O'Kennedy, R., Prostate cancer diagnostics: Clinical challenges and the ongoing need for disruptive and effective diagnostic tools. *Biotechnology advances* 2016.

4. Hayes, J. H.; Barry, M. J.; Kantoff, P. W.; Stahl, J. E., Prostate-specific antigen screening for prostate cancer: a decision-analytical perspective. *BJU international* 2007, *100* (3), 486-8.

5. Hayes, J. H.; Barry, M. J., Screening for prostate cancer with the prostate-specific antigen test: a review of current evidence. *Jama* 2014, *311* (11), 1143-9.

6. McClure, P.; Elnakib, A.; Abou El-Ghar, M.; Khalifa, F.; Soliman, A.; El-Diasty, T.; Suri, J. S.; Elmaghraby, A.; El-Baz, A., In-vitro and in-vivo diagnostic techniques for prostate cancer: a review. *Journal of biomedical nanotechnology* 2014, *10* (10), 2747-77.

7. Jadvar, H., Is There Use for FDG-PET in Prostate Cancer? *Seminars in nuclear medicine* 2016, *46* (6), 502-506.

8. (UK), N. C. C. f. C., Prostate Cancer: Diagnosis and Treatment. *NICE Clinical Guidelines* 2014, *175*.

9. Mertan, F. V.; Berman, R.; Szajek, K.; Pinto, P. A.; Choyke, P. L.; Turkbey, B., Evaluating the Role of mpMRI in Prostate Cancer Assessment. *Expert review of medical devices* 2016, *13* (2), 129-41.

10. Tuxhorn, J. A.; Ayala, G. E.; Rowley, D. R., Reactive stroma in prostate cancer progression. *The Journal of urology* 2001, *166* (6), 2472-83.

11. Dvorak, H. F., Tumors: wounds that do not heal-redux. *Cancer immunology research* 2015, *3* (1), 1-11.

12. Ye, F.; Wu, X.; Jeong, E. K.; Jia, Z.; Yang, T.; Parker, D.; Lu, Z. R., A peptide targeted contrast agent specific to fibrin-fibronectin complexes for cancer molecular imaging with MRI. *Bioconjugate chemistry* 2008, *19* (12), 2300-3.

13. Pilch, J.; Brown, D. M.; Komatsu, M.; Jarvinen, T. A.; Yang, M.; Peters, D.; Hoffman, R. M.; Ruoslahti, E., Peptides selected for binding to clotted plasma accumulate in tumor stroma and wounds. *Proceedings of the National Academy of Sciences of the United States of America* 2006, *103* (8), 2800-4.

14. Tan, M.; Wu, X.; Jeong, E. K.; Chen, Q.; Lu, Z. R., Peptide-targeted Nanoglobular Gd-DOTA monoamide conjugates for magnetic resonance cancer molecular imaging. *Biomacromolecules* 2010, *11* (3), 754-61.

15. Tan, M.; Burden-Gulley, S. M.; Li, W.; Wu, X.; Lindner, D.; Brady-Kalnay, S. M.; Gulani, V.; Lu, Z. R., MR molecular imaging of prostate cancer with a peptide-targeted contrast agent in a mouse orthotopic prostate cancer model. *Pharmaceutical research* 2012, *29* (4), 953-60.

16. Tan, M.; Ye, Z.; Lindner, D.; Brady-Kalnay, S. M.; Lu, Z. R., Synthesis and evaluation of a targeted nanoglobular dual-modal imaging agent for MR imaging and image-guided surgery of prostate cancer. *Pharmaceutical research* 2014, *31* (6), 1469-76.

17. Simberg, D.; Duza, T.; Park, J. H.; Essler, M.; Pilch, J.; Zhang, L.; Derfus, A. M.; Yang, M.; Hoffman, R. M.; Bhatia, S.; Sailor, M. J.; Ruoslahti, E., Biomimetic amplification of nanoparticle homing to tumors. *Proceedings of the National Academy of Sciences of the United States of America* 2007, *104* (3), 932-6.

18. Zhou, Z.; Wu, X.; Kresak, A.; Griswold, M.; Lu, Z. R., Peptide targeted tripod macrocyclic Gd(III) chelates for cancer molecular MRI. *Biomaterials* 2013, *34* (31), 7683-93.

19. Wu, X.; Yu, G.; Lindner, D.; Brady-Kalnay, S. M.; Zhang, Q.; Lu, Z. R., Peptide targeted high-resolution molecular imaging of prostate cancer with MRI. *American journal of nuclear medicine and molecular imaging* 2014, *4* (6), 525-36.

20. Aime, S.; Calabi, L.; Cavallotti, C.; Gianolio, E.; Giovenzana, G. B.; Losi, P.; Maiocchi, A.; Palmisano, G.; Sisti, M., [Gd-AAZTA]-: a new structural entry for an improved generation of MRI contrast agents. *Inorganic chemistry* 2004, *43* (24), 7588-90.

21. Tripepi M., C. F., Gianolio E., Kock F.V., Pagoto A., Stefania R., Digilio G., Aime S., Synthesis of high relaxivity gadolinium AAZTA tetramers as building blocks for bioconjugation. *Bioconjugate chemistry* Under Revision.

22. Chung, E. J.; Cheng, Y.; Morshed, R.; Nord, K.; Han, Y.; Wegscheid, M. L.; Auffinger, B.; Wainwright, D. A.; Lesniak, M. S.; Tirrell, M. V., Fibrin-binding, peptide amphiphile micelles for targeting glioblastoma. *Biomaterials* 2014, *35* (4), 1249-56.

23. Solomon, I., Relaxation Processes in a System of Two Spins. *Physical Review* 1955, *99* (2), 559-565.

24. Dvorak, H. F.; Senger, D. R.; Dvorak, A. M., Fibrin as a component of the tumor stroma: origins and biological significance. *Cancer metastasis reviews* 1983, *2* (1), 41-73.

25. Nagy, J. A.; Brown, L. F.; Senger, D. R.; Lanir, N.; Van de Water, L.; Dvorak, A. M.; Dvorak, H. F., Pathogenesis of tumor stroma generation: a critical role for leaky blood vessels and fibrin deposition. *Biochimica et biophysica acta* 1989, *948* (3), 305-26.

26. Wojtukiewicz, M. Z.; Zacharski, L. R.; Memoli, V. A.; Kisiel, W.; Kudryk, B. J.; Moritz, T. E.; Rousseau, S. M.; Stump, D. C., Fibrin formation on vessel walls in hyperplastic and malignant

prostate tissue. *Cancer* 1991, *67* (5), 1377-83.

27. Ruoslahti, E.; Pierschbacher, M.; Engvall, E.; Oldberg, A.; Hayman, E. G., Molecular and biological interactions of fibronectin. *The Journal of investigative dermatology* 1982, *79 Suppl 1*, 65s-68s.

28. Rowley, D. R., What might a stromal response mean to prostate cancer progression? *Cancer metastasis reviews* 1998, *17* (4), 411-9.

29. Aime, S.; Caravan, P., Biodistribution of gadolinium-based contrast agents, including gadolinium deposition. *Journal of magnetic resonance imaging : JMRI* 2009, *30* (6), 1259-67.

30. Fraum, T. J.; Ludwig, D. R.; Bashir, M. R.; Fowler, K. J., Gadolinium-based contrast agents: A comprehensive risk assessment. *Journal of magnetic resonance imaging : JMRI* 2017.

31. Song, Y.; Huang, Z.; Xu, J.; Ren, D.; Wang, Y.; Zheng, X.; Shen, Y.; Wang, L.; Gao, H.; Hou, J.; Pang, Z.; Qian, J.; Ge, J., Multimodal SPION-CREKA peptide based agents for molecular imaging of microthrombus in a rat myocardial ischemia-reperfusion model. *Biomaterials* 2014, *35* (9), 2961-70.

32. Zhao, J.; Zhang, B.; Shen, S.; Chen, J.; Zhang, Q.; Jiang, X.; Pang, Z., CREKA peptide-conjugated dendrimer nanoparticles for glioblastoma multiforme delivery. *Journal of colloid and interface science* 2015, *450*, 396-403.

33. Longmire, M.; Choyke, P. L.; Kobayashi, H., Clearance properties of nano-sized particles and molecules as imaging agents: considerations and caveats. *Nanomedicine* 2008, *3* (5), 703-17.

3.3- IGS of Prostate Adenocarcinoma

Based on:
Pagoto A., Marini G., Tripepi M., Garello F., Stefania R., Bardini P, Arena F, Lanzardo S., Valbusa G., Aime S., Terreno E. *NIRF-guided surgery of Prostate Cancer targeting Gastrin-Releasing Peptide Receptor,* In Preparation

Introduction

Prostate cancer (PCa) is one of the most spread non-cutaneous cancer, with high incidence in western countries. It represents, just in USA, the third-leading cause of cancer-related death, with approximatively 160000 new cases expected in 2017 (**1**). Different treatments have been proposed for this type of tumor, being surgical intervention and radiation therapy the most reliable (**2,3**). While the latter is the most effective on advanced tumor, it was demonstrated that surgery has more pronounced long term benefits in localized cancer (**4**). Nowadays, the robotic assisted radical prostatectomy is becoming the most accurate way to completely eradicate the prostate cancer, with shorter convalescence and better outcomes (**5,6**). Unfortunately, despite the enormous technological improvement, the surgery on prostate still remains a great challenge: given to its position into the pelvis and the thin tissues surrounding it (1-2 mm), it is not always possible to properly delineate the tumor margins (**7**). Consequently, it could be possible the formation of positive surgical margins (PSM), which are often related to the disease progression and subsequent spread (**8**). Moreover, especially for young patients, the surgeons could be skeptic in the complete removal of the prostate and surrounding tissues trying, as much as possible, to preserve the natural prostate functions. For example, it is known that the removal of posterolateral prostate, which contains the neurovascular bundle, can lead to the loss of erectile function and urinary control. (**9,10**). Since PCa cells acquire the ability to travel along the nerves (**11**), is even more fundamental to discriminate the presence of the tumor cells inside the prostate.

The advantages to precisely localize the resident tumor cells during surgery could give enormous benefits to the patients, as well as lead to the consequent costs reduction for the health care system. During the last decade, new techniques are emerging aimed at visually guiding the surgeon in the operation theater. The Image-Guided Surgery (IGS), which typically exploit fluorescence dyes to visualize intraoperatively the malignant cells, is an established technique (**12,13**) already applied in the clinic (**14,15**). The use of near infrared fluorescent (NIRF) probes, with good penetration and low absorption in the tissues, have had massive applications in the field (**16,17,18,19**). Indocyanine Green (ICG), mainly used to identify invaded lymph node, is one of the first FDA approved probe for intraoperative application (**20,21,22**). However, the lack of specificity, low water solubility and dye spillage are some of its main drawbacks. Recently, the spread of targeted optical molecular probes has improved the tumor detection specificity, with promising results in different types of cancer, from colon (**23,24**) to head and neck (**25,26**). Concerning the prostate cancer, many efforts have been done to find probes to precisely detect the malignant tissue, both with untargeted dyes (**27**) and high molecular weight vectors (**28,29**).

Herein, a NIRF molecular probe based on a peptide analog of the natural ligand Bombesin (BBN), widely used as vector for nuclear medicine tracers (**30,31,32**), is proposed.

The use of small molecules, such as peptides, with a relative fast clearance, low immunogenicity, and easy tissue diffusion make them great candidates as targeting vector for tumor detection. The chosen vector is able to recognize the Gastrin Releasing Peptide Receptor (GRPR): a transmembrane protein widely overexpressed in primary prostate cancer (**33**), even in small tumor foci (**34**). In this work, a BBN analog was properly conjugated to a water soluble cyanine (sulfo Cy5.5), to form the highly water soluble probe BBN-Cy5.5. The agent was first characterized *in vitro* on a human prostate cell line (PC3), and then assessed *in vivo* on an orthotopic PC3 mouse model.

Experimental Procedures

BBN-like peptide synthesis and characterization

The BBN analog (C-Linker-QWAVGHLM-NH_2) was synthesized by automated Solid Phase Peptide Synthesis (Liberty CEM microwave) using standard FMOC (Fluorenylmethyloxycarbonyl) chloride chemistry. The Rink Amide resin (0.5 mmol/g) was loaded into the reaction vessels and the amino acids automatically coupled by using 5 equivalent excess of each Fmoc-reagent. The coupling reactions proceeded for 5 min (75 °C, 35 W) in presence of 5.0 eq. of PyBOP (benzotriazol-1-yl26oxytripyrrolidinophosphonium hexafluorophosphate) and 10 eq. of DIPEA (Diisopropylethylamine) in DMF (Dimethylformamide). The FMOC-deprotection steps were completed within 3 min (75 °C) using 20% of piperidine in DMF. When the synthesis was completed, the resin was transferred into a glass reaction vessel and the cleavage mixture of TFA (trifluoroacetic acid)/ TIPS(triisopropylsilane)/Purified Water/ Phenol (95:1:2:2, v:v) was added. The mixture was shaken for 2 h at room temperature and the resin filtered out. The final solution was dropped to cold diethyl ether to obtain the final solid product. After three washing cycle by centrifugation (2000 rpm, 3 minutes) in diethyl ether, the solid product was dissolved in purified water and lyophilized (yield 45%).

Analytical HPLC-MS were carried out on a Waters Fraction Lynx autopurification system equipped with micromass ZQ (ESCI ionization mode and dual- detectors), column Waters XBridge BEH 300 C18 3.5 µm, 4.6 mm ×150 mm and UV detection at 220 nm. The following linear gradient (Table 1) was used:

Time	%A	%B
0.00	85	15
10.00	15	700
30.00	0	100

Table 1. Gradient for BBN peptide HPLC-MS analysis. eluents A, H2O(0,1 % TFA); B, CH3CN (0,1% TFA)

ESI-MS: $[M+H]^+$ 1187,56 (obsd.) 1188 (calcd for $C_{52}H_{81}N_{15}O_{13}S_2$).

Malemide activation of sulfo-Cy5.5-COOH

Sulfo-Cyanine5.5 carboxylic acid (Lumiprobe) (4.7 mg, 4.6 mmol) was dissolved in 1 mL of DMF and solid HATU (4.37 mg, 1,2 µmol), DIPEA (8 µL, 4,6 µmol) and solid 1-(2-aminoethyl)maleimide hydrochloride (2.03 mg, 0.012) were added. The reaction was stirred overnight at room temperature, in the dark. The product was precipitated in DCM and it was centrifuged and washed thrice with the same solvent (5000 rpm, 20 minutes).

The product was then characterized in HPLC-UV (Waters Alliance Separation system equipped with photodiode array detector) (yield 90%) using the following gradient (Table 2)

Time	%A	%B
0.00	85	15
10.00	80	20
20.00	50	50
30.00	0	100

Table 2. Gradient for Sulfo-Cyanine5.5 maleimide HPLC-UV analysis eluents A, H_2O(0,1 % TFA); B, CH_3CN (0,1% TFA) RT: 12.8 min

Synthesis of the targeting product BBN-Cy5.5

Sulfo-Cyanine5.5 maleimide (1.44 mg, 1,3 µmol) was dissolved in 1.5 mL of a solution of H_2O and sodium acetate buffer (CH_3COONa 0.1M, pH 6) in a ratio 1:1. BBN peptide (1 eq) was dissolved in 0.5 mL of sodium acetate buffer and added to the solution containing sulfo-Cyanine5.5 maleimide. The reaction was stirred for 4 h under inert atmosphere using a flow of argon, in the dark.

The solution was desalted using PD-10 column Sephadex G-25, collecting 10 fractions of 1 mL each, for every run (1 mL injection); The final product was finally purified by HPLC-MS, freeze-dried overnight and the purity (90%) assessed by HPLC-UV (RT: 15 min)

ESI-MS: $[M+2H]^{2+}$ 1105.64 (obsd.) 1105.38 (calcd. for $C_{98}H_{129}N_{19}O_{28}S_6$); $[M+3H]^{3+}$ 736.81 (obsd.) 736.60 (calcd.)

Spectrophotometric and Fluorimetric Optical Characterization of dyes

The targeting probe BBN-Cy5.5 was dissolved in PBS (Phosphate Buffer) (NaCl 137 mM, KCl 2.7 mM, Na_2HPO_4 10mM, KH_2PO_4 1.8mM - pH7.4) and the solutions (1 µM and 0.2 µM) was used for spectrophotometric and spectrofluorimetric characterization, respectively.

For the spectrophotometric characterization, the solution was transferred in a standard 10 mm polystyrene cuvette and the absorbance was measured at 673 nm. The fluorimetric spectrum was obtained using a standard 10 mm polystyrene cuvette, setting 673 nm as excitation wavelength (maximum) and 691 nm as emission (maximum) wavelength. The protocol was repeated for the untargeted sulfo-Cy5.5(COOH).

Relative Quantum Yield evaluation

The relative quantum yield of the probe was evaluated comparing the emission spectra at different concentrations of the probe itself with indocyanine green (ICG). Briefly, 5 dilutions (absorbance range from 0.02 to 0.1 verified on spectrophotometer) were prepared for BBN-Cy5.5 and ICG (in PBS and DMSO, respectively) and the emission were integrated for each dilution point. Plotting the integrated value against the absorbance, it was possible to obtain two curves, each one characterized by a specific slope.

To calculate the relative quantum yield the following formula was applied:

$$\phi_X = \phi_{ICG} \left(\frac{Sl_X}{Sl_{ICG}}\right)\left(\frac{\mu_x^2}{\mu_{ICG}^2}\right)$$

Where the subscripts X denote the sample, Φ is the fluorescence quantum yield, *Sl* the slope obtained from the above described plot, and η is the refractive index of the solvent.

In vitro PC3 interaction experiments

Human PC3 cell line was cultured until confluence using DMEM F-12 medium supplemented with glutamine (2 mM), 10% fetal bovine serum (FBS) and penicillin/streptomycin antibiotics (10,000 IU/ml penicillin, 10,000 IU/ml streptomycin). After 2 times PBS flushing, the cell dissociation solution non-enzymatic solution (Sigma) was added and the flask left in the humidified incubator (37°C) for

20 min. The cells were then collected after gentle centrifugation (1100 rpm, 5 min), counted and divided (1 x 10^6 cells per falcon) for each different condition. The BBN-Cy5.5 and control (Sulfo-Cy5.5(COOH)) solutions (100 µL, 2 µM) were incubated with PC3 cells, both at 4°C (30 min) and 37°C (15 min). Triplicate independent samples were prepared. After centrifugation (1100 rpm, 5 min) and 2 times washing with PBS, the samples were finally suspended in PBS (100 µL) and sonicated for 30 sec (power 30%). For each sample, first the protein assay dye reagent (Biorad) were performed and then fluorimetric spectra acquired (λ_{exc} 673 nm).

The concentration of the dye bound on cell membranes or cell internalized was calculated, in comparison with the initial incubation quantities, analyzing the fluorescence signal and using a calibration curve of the sulfo-Cy5.5. The statistical analysis was performed using t-student test (* $p < 0.05$)

Western Blot evaluation of GRPR

Cells (PC3) and tissues (tumor and kidney) were homogenized (Precellys homogenizer - Bertin Instruments) in lysis buffer (NaCl 150 mM, Tris-HCl-pH 8- 50 mM, Triton x100 1%, EDTA 1 mM, NaF 100 mM, $MgCl_2$ 1 mM, Glicerol 10%) supplemented with 1 mM PMSF (Phenylmethanesulfonil fluoride) and Proteases inhibitors diluted 100x. Lysates were centrifuged (14000 rpm, 15 min) at 4°C. Protein concentration was determined by Pierce™ BCA Protein Assay Kit (Termofisher) using BSA (Bovine Serum Albumin) as standard. After preparation of 8% polyacrylamide gel, the samples were mixed with sample buffer (added with β-Mercaptoethanol). After protein heating (8 min – 70 °C), samples were loaded in the gel (20 µg per lane) and the run performed (1.5 h, 100 V). Following the membrane protein transfer, the staining with anti-GRPR antibody (PA527073, Termofisher) (PBS-Tween 0.1% + 5% of BSA (w/v)) was performed overnight ad 4 °C. The same protocol was used for loading the control with anti-vinculin antibody (ab129002, Abcam) (PBS-Tween 0.1% + 3% of milk (w/v). Subsequently, the secondary antibody staining (1h, room temperature) was performed and the signal acquired (Chemi Doc Touch Imaging system, Biorad) and analyzed to evaluate the relative concentration of the protein in the tissues.

PC3 Orthotopic Mouse Model

The surgical procedure was performed on Athymic nude mice of 6-8 weeks with weight between 19-21 g. Tumor induction protocol was carried out under the subcutaneous administration of an analgesic (Rymadil) at a dose of 5 mg / kg one hour before the procedure. The animals were anesthetized in the induction chamber, then transferred to the floor and arranged adequately for

orthotopic implantation. Local anesthetic (lidocaine), was also applied in the intervention area. The inoculation procedure was started with the disinfection with Betadine® of the lower abdomen, followed by the incision of about 12-15 mm along the central line 3-4 cm above the urinary orifice. The mice prostate was exposed and the adipose tissue adjacent momentarily removed. PC-3 cells were then injected ($1x10^6$ cells, 20 µL) with a microsyringe with a 27G needle, into one of the two ventral lobes of the prostate. Muscle and skin layer were sewn with sterile non-absorbable wire (3-0 black silk, Distrex Spa) and the wound cleaned with Betadine®. Upon awakening, the animals were placed and allowed to recover. Rymadil was again administered once, 24 hours after surgery. After 28 days, the animals were enrolled in the experiments.

Ex-vivo biodistribution of the dyes

Biodistribution studies on the PC3 tumor model and healthy mice were performed administering i.v. 3 nmol/mouse of a PBS buffered aqueous solution of BBN-Cy5.5. Mice (n=3 for each point) were euthanized at different time points p.i. (30 min, 2 h, 5 h and 24 h) and immediately exposed under the IVIS optical imager (Perkin Elmer Inc., Waltham, Massachusetts, USA).

Afterwards, organs and tissues (liver, kidneys, spleen, bladder, muscle, prostate-tumor; seminal vesicles, pancreas, lungs) were collected and fluorescence signal quantified. The blood collected at the same time points was used to assess the blood half-life of the injected dye.

Biodistribution of the untargeted Sulfo Cy5.5(COOH) dye was analyzed 24 h p.i. in both tumor and healthy mice. All the measurements were triplicate and statistically analyzed by one-way ANOVA test ($p < 0.05$ and $p < 0.001$)

Image-Guided surgery simulation

IGS simulation was performed on mice bearing PC3 orthotopic tumor (n=3). To this purpose, 10 nmol of BBN-Cy5.5 were administered intravenously. 24 hours p.i. the mice were sacrificed and the peritoneal membrane was cut in correspondence of the pelvis area to expose the urogenital apparatus. To evaluate the tumor accumulation of the targeting probe, the mice were imaged under an AxioZoom.v16 planar microscope, equipped with a HXP 200C illuminator (Mercury short arc lamp) and excitation/emission filters (ex:615/665 nm em: 695/770 nm). Finally, to quantify the fluorescence signal in the prostate as well as in other organs (liver, kidneys, spleen, pancreas, lungs, bladder, seminal vesicles and muscle), the organs were excised, laid down in a plate and imaged using IVIS spectrum.

Results

In vitro results

The BBN-like peptide sequence (**35**) was suitably modified to the N-terminus, adding a short PEG and a cysteine, to make it ready for the bioconjugation with the fluorescent dye (Figure 1A). The peptidic vector, properly analyzed by LC-MS (Figure 1B and 1C), was conjugated via Michael addition with the activated Sulfo Cy5.5 Maleimide (Scheme 1). The reaction was monitored by HPLC-UV (Figure 2A), and the final product BBN-Cy5.5 was obtained. The product showed a high solubility in water and aqueous buffers, mainly owing to the sulphonate moieties and the short PEG chain. The absorption spectra of the peptide were acquired to confirm the expected absorption peak at 673 nm. Afterwards, a spectrofluorimetric characterization was also performed for the targeted and the untargeted (Sulfo Cy5.5(COOH)) dyes, with no observable influence in both excitation (λ_{exc} 673 nm) and emission (λ_{em} 691 nm) wavelengths due to the peptidic vector (Figure 2B). Moreover, the relative quantum yield (QY) of the compound was evaluated, and a value of 0.33, using the ICG (QY 0.12) as standard, was determined.

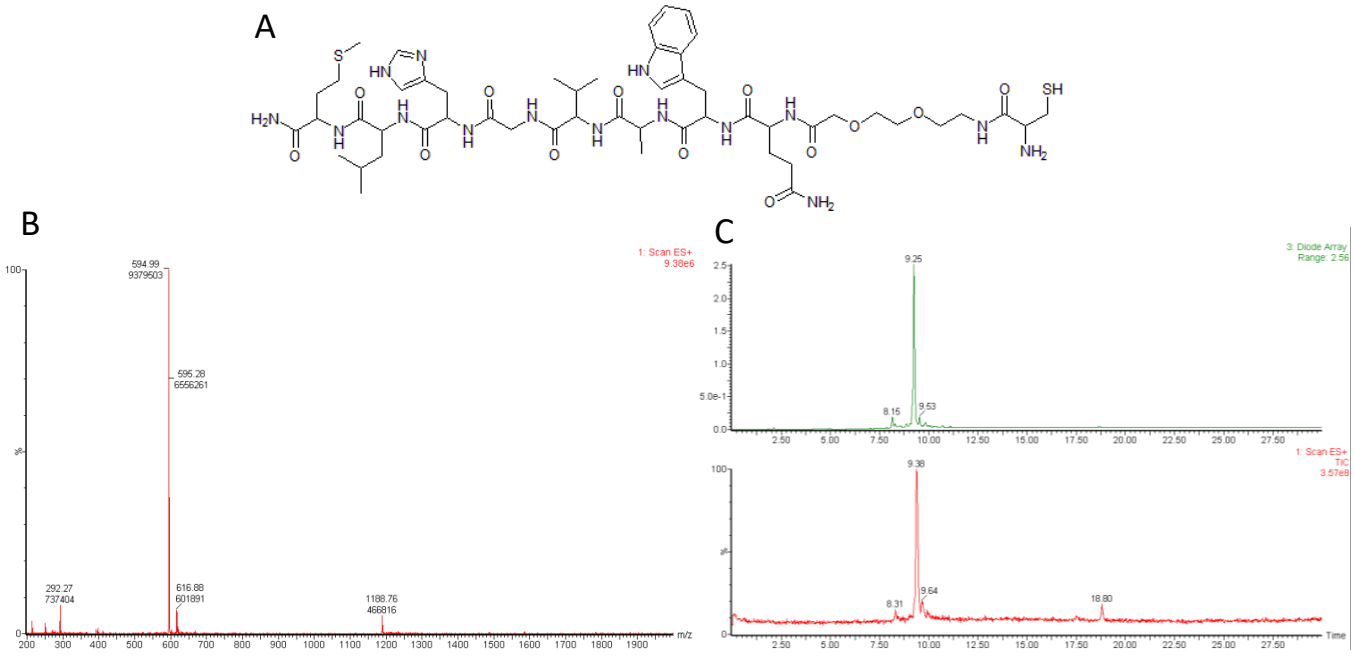

Figure 1. A) Peptide BBN-like peptide opportunely modified to the N-terminus B) ESI mass spectrum of the BBN-like peptide C) UV (top) and mass chromatogram (bottom) of the BBN-like peptide

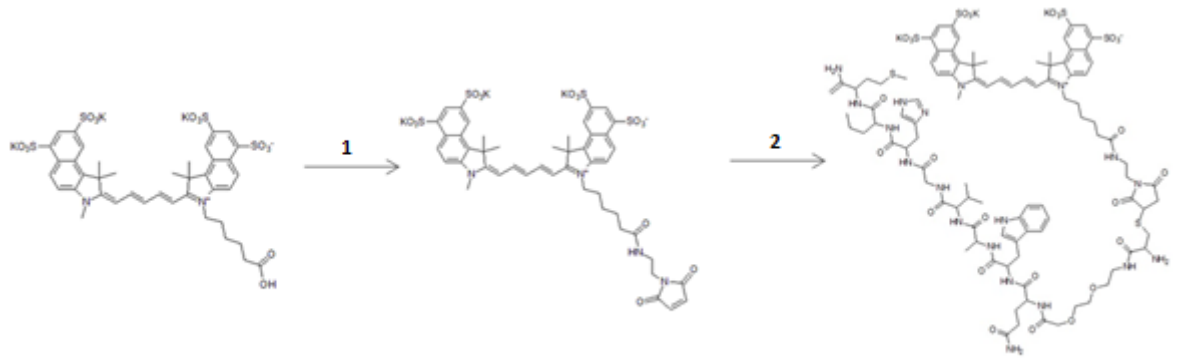

Scheme 1. Synthetic scheme to BBN-Cy5.5. 1) reaction in DMF overnight, solid HATU (1,2 µmol), DIPEA (4,6 µmol) and solid 1-(2-aminoethyl)maleimide hydrochloride (1,2 µmol). 2) reaction in H_2O and sodium acetate buffer in a ratio 1:1 4h in inert atmosphere. BBN-like peptide (1 eq) was added to the solution containing sulfo-Cyanine5.5 maleimide.

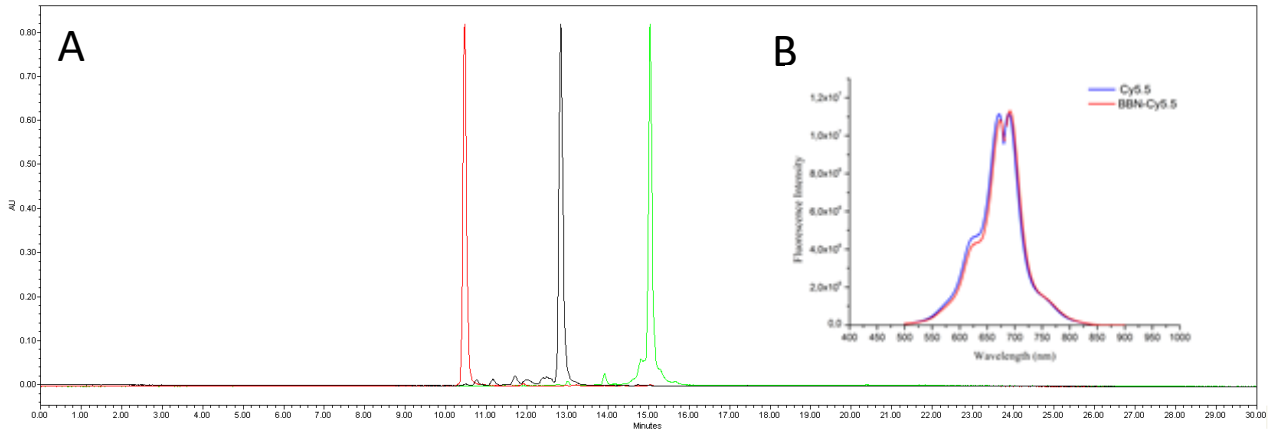

Figure 2. A) HPLC-UV chromatogram of the Sulfo Cy5.5(COOH) (red- RT: 10.4min), Sulfo Cy5.5-Maleimide (black- RT: 12.8min) and BBN -Cy5.5 (black- RT: 15 min) B) Excitation and emission spectra of the BBN-Cy5.5 and Sulfo Cy5.5(COOH) (ex_{max}=673nm; em_{max}=691nm)

In vitro experiments on cells

The incubation of BBN-Cy5.5 or Sulfo Cy5.5(COOH) with PC3 cells at 4°C or 37°C allowed the estimation of cell binding and uptake, respectively. As shown in Figure 3, in both the conditions, the fluorescence signal from BBN-Cy5.5 was higher than the untargeted dye after incubation with the tumor cells, especially considering 4°C ($p < 0.05$). The difference in the signal intensity between the experiments carried out at 4°C and 37°C can be justified by considering that in the latter condition the incubated agent is internalized into cells.

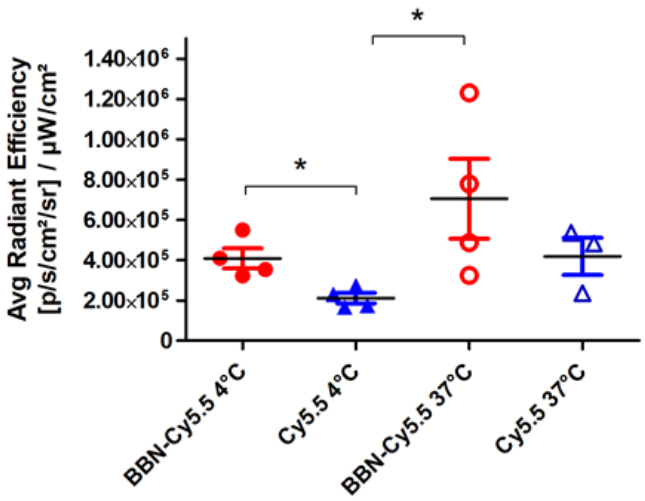

Figure 3. In vitro experiments incubating targeting and control probes on PC3 cell line. a) Differences between BBN-Cy5.5 and Sulfo-Cy5.5(COOH) at 4°C and 37°C.

Biodistribution studies

Firstly, the western blot evaluation of the GRPR (43kDa) expression in the tumor tissue were performed. Two preliminary tests on different prostate tumors, showed a clear difference in comparison with the chosen negative control (Figure 4)

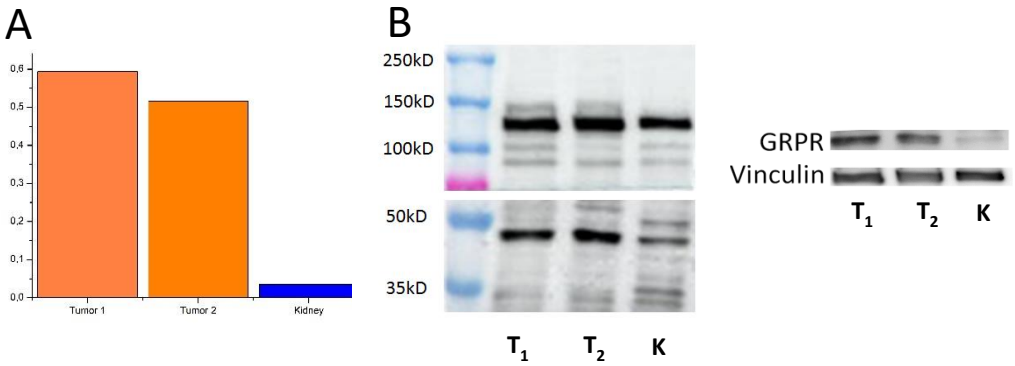

Figure 4. Western blot relative quantification (A) and acquired images (B) of GRPR in Tumors (T1 and T2) and Kidney (K). Vinculin (124kDa) was used as loading control.

Once the presence of GRPR was confirmed in the tumor, the biodistribution of the targeted dye was assessed by measuring the fluorescence signal (on IVIS optical imager) on selected organs and tissues (including blood). They were explanted at different time points after the systemic injection of BBN-Cy5.5 (3 nmol/mouse) on tumor or healthy mice (Figure 5A). Interestingly, the decrease of the fluorescence signal arising from the targeted dye in the blood was two-fold quicker in healthy mice, with an estimated half-life time of 0.9 h (Figure 5B). Likely, this finding could be the result of some alterations in the functionalities of the excretory organs (kidneys and liver) in the diseased animals, which prolonged the blood circulation time of the dye.

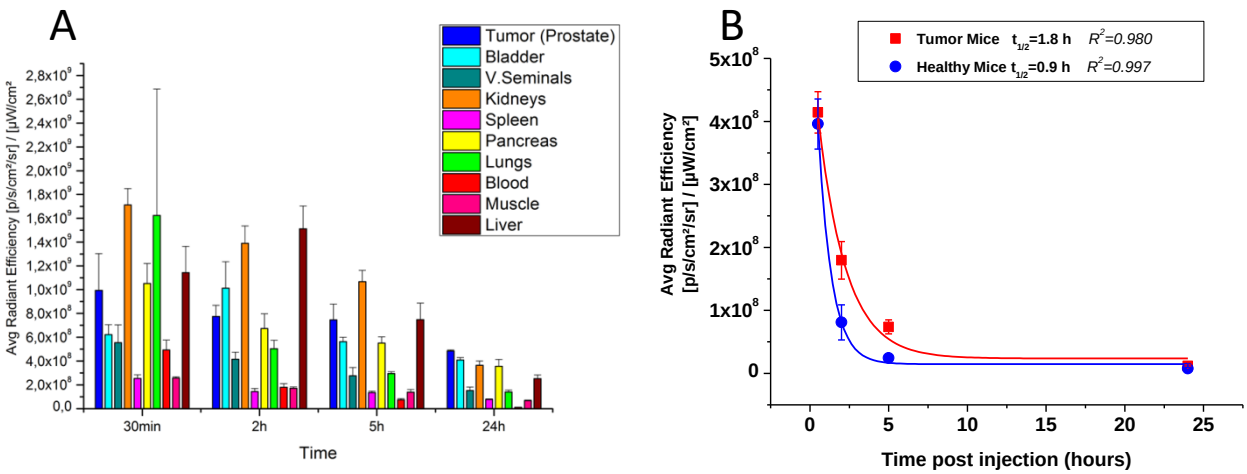

Figure 5. (A) IVIS ex vivo optical signal biodistribution for BBN-Cy5.5 and (B) blood half-life in tumor and healthy mice

Accumulation of the targeting probe in the tumor occurred 24 h post injection (Figure 6A). The amount of BBN-Cy5.5 in the tumor was more than 5-times higher than in the healthy organ (Figure 6B). Two additional mice groups (tumor + healthy) were injected with the untargeted Sulfo Cy5.5(COOH) dye and the organs were explanted after 24 h. The data reported in Figure 6B highlighted the significant difference ($p < 0.001$) between the fluorescence signal found in the tumor with respect to the healthy prostate. This applies for both targeted and untargeted agents. However, the fluorescence from the tumor of the animals injected with the targeted probe was higher ($p < 0.05$) than the corresponding value measured for the untargeted dye. Figure 7 reports some representative images, taken on IVIS imager, of the explanted organs in this experiment.

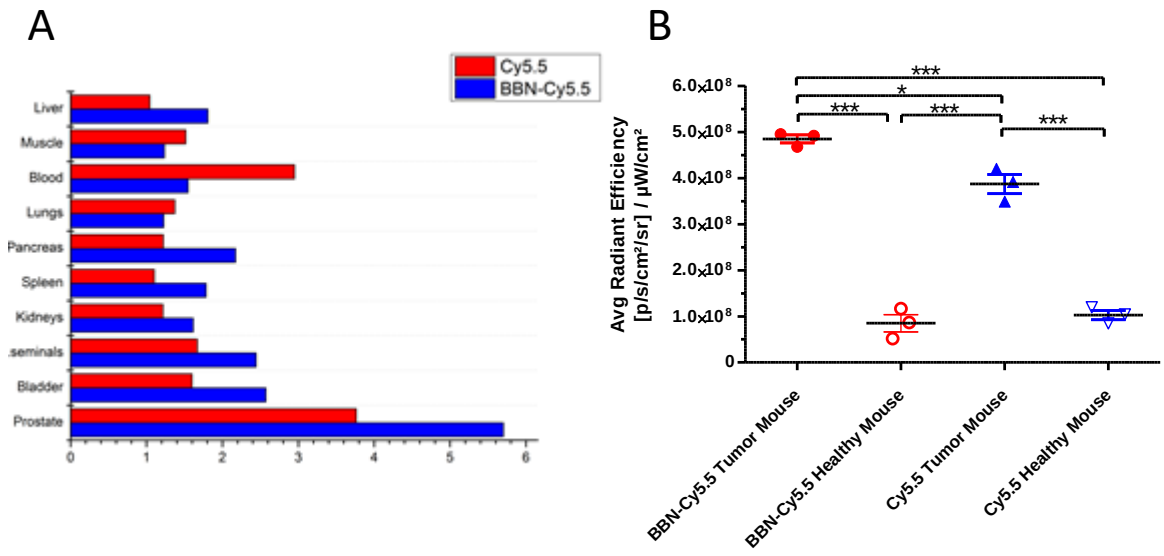

Figure 6. (A) Ratio between Tumor and Healthy tissue 24 p.i. for targeting and control dye. (B) 24 post injection ex vivo evaluation of dyes fluorescence signal in the prostate (healthy and tumor)

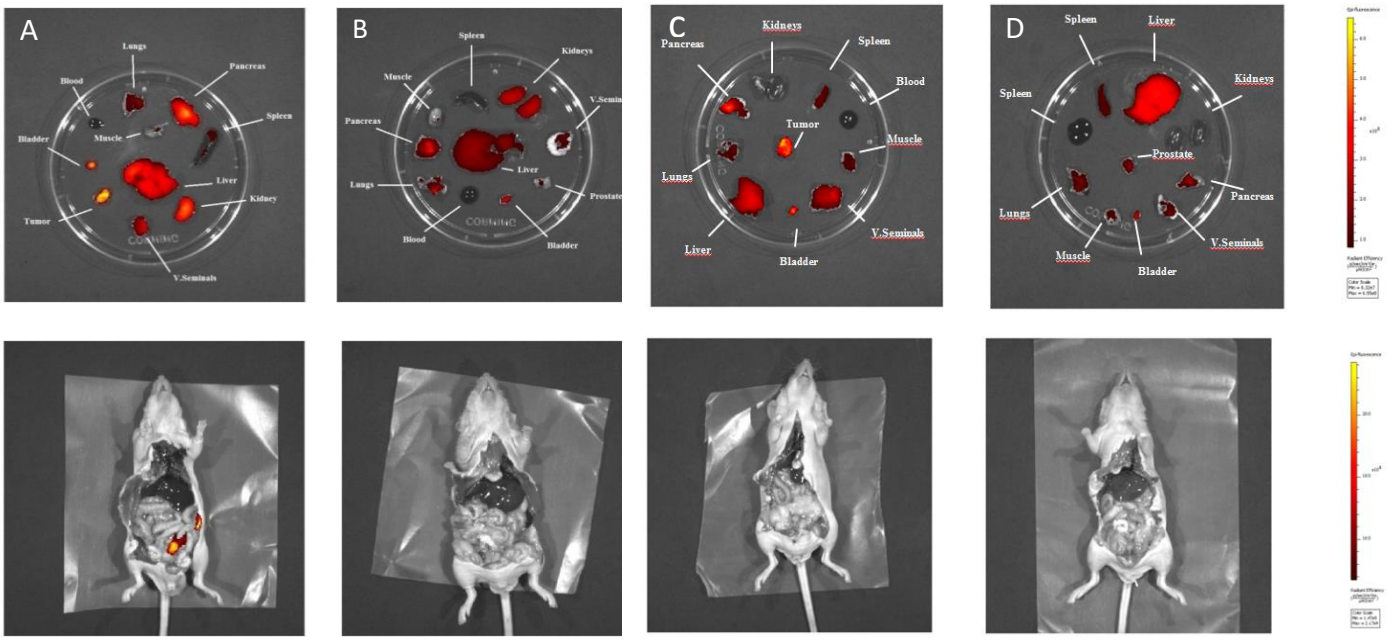

Figure 7. (top) Organs *ex vivo* fluorescence signal quantification 24 p.i. of BBN-Cy5.5 in tumor (A) and healthy (B) mice. The same experiment was performed with the Cy5.5 in tumor (C) and healthy (D) controls. The correspondent animals before the organs removal are shown in the bottom line

Preliminary Image-Guided Surgery experiments

After preliminary image-guided surgery on the mouse tumor model, it was possible to clearly identify the fluorescent signal arising from the targeting probe in the tumor (24 hours p.i.). The localized fluorescent signal allowed to remove the main tumor (Figure 8B) (which has almost entirely invaded the prostate) and, even more important, also some small tumor foci (Figure 8C and D) left in the pelvis area after the first surgical removal procedure were visualized and removed. Even if the signal results specifically tumor localized, aspecific fluorescence were found in the terminal intestine part. This signal, probably due to the partial hepatobiliary excretion of the probe and further accumulation in the excrements, did not substantially interfere with the tumor localization.

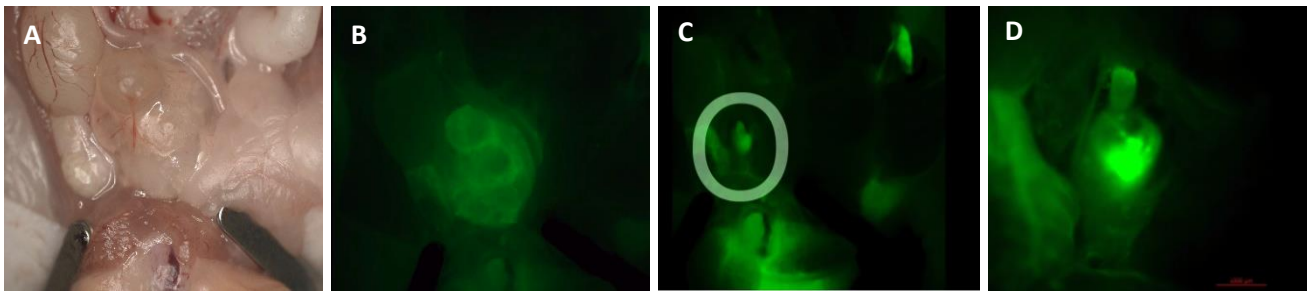

Figure 8. IGS simulation after injection of BBN-Cy5.5 (10nmol) on tumor bearing mouse (24 p.i.).
(A) Natural light view of the exposed urogenital area (B) Main prostate tumor (C) Small cancer foci left after removal of main tumor (D) Magnification of the Figure C

Discussion

The identification of small cancer foci in the prostate, which could be easily missed by visual inspection during the surgery, is becoming fundamental to lead to a better prognosis for the patient. Moreover, especially for young patients, who nowadays represent almost the 10% of overall cases (**36**), the preservation of erectile-urinary controls could drastically improve their life quality. Actually, there are no optical probes clinically approved for the specialized treatment of cancer foci in the prostate during surgery, and for this reason the last years have witnessed a boost in this direction. Several target molecules have been proposed for imaging prostate cancer, and one the most exploited has been the PSMA (Prostate Specific Membrane Antigen). This is a low molecular weight protein, overexpressed on the cellular membrane of 90-95% of overall prostate cancer. Even if its expression was linked to androgen response (**37**), PSMA was found overexpressed also in androgen-independent highly metastatic tumors (**38**). The advantages to use this target for imaging purposes are undoubted even if, recently, false-positive cases have been reported for PSMA agents (**39,40**). Also for this reason, the research of other potential biological targets is still needed. During the years, several imaging probes targeted to the Gastrin Releasing Peptide Receptor (GRPR) was proposed. GRPR is a G-protein coupled receptor, part of the bombesin family, which is widely expressed on localized prostate cancer (**33**). It has been often associated with androgen-independent tumors and metastatization (**41**), but the link with tumor stages and grade is under debate (**34**,**42**) Conversely, it was well established the higher expression of the receptor in primary tumors in comparison with healthy prostatic tissue (**43**). In this work, the human androgen-independent prostatic cells PC-3 were orthotopically injected in the prostate of nude mice to better mimic the conditions of a primary prostatic tumor, and a specific peptidic vector was designed to interact with GRPR. The use of a peptide as targeting vector showed many advantages for molecular imaging purposes. The standardized solid phase chemistry allows an easy, controlled and cheap synthesis, which leads to the formation of a low molecular weight product that could be functionalized for imaging purposes. These products, bioactive at nanomolar concentrations, are normally characterized by a fast body excretion. Moreover, the previously mentioned characteristics combined with high receptor affinity, allow a high cellular uptake and penetration in the targeting site (**44**). The Gastrin Releasing Peptide (GRP) is an agonist peptide that represent the natural ligand of GRPR in mammals (**45,46**). Interestingly, the sequence of the mammal peptide showed high percentage of sequence similarity with the amphibians analogue bombesin (BBN) peptide: the C-terminus region shares similar affinity and specificity with the natural ligand GRP (**47**). This peptide, with the preserved homology sequence, was exploited as vector for different

molecular imaging applications, especially for nuclear medicine purposes (**30,31,32**). Herein, a version of BBN (**35**) properly modified to the N-terminus to allow the conjugation to an optical imaging agent, was designed. Cy5.5 was chosen as NIRF dye for its advantages for *in vivo* applications. First of all, its emission spectrum, close to the near infrared window, minimizes the absorption by tissue components and increases light penetration. Furthermore, the presence of four sulfonate moieties offers the important opportunity to increase the water solubility of the dye. The linkage between the dye, suitably conjugated with a maleimide reactive group, and the peptide was carried out via a Michael addition on the N-terminus of the vector. The photophysical properties of the targeted dye was not affected by the presence of the peptide. The dye was then tested on the GRPR-expressing PC3 cell line (**48**), confirming a specific interaction of the targeting probe on the surface of tumor cells (4°C), followed by a cell internalization (37°C). These findings are in line with the previously reported active GRPR internalization (**49**). Subsequently, the biodistribution of the dye was assessed *ex vivo* on an orthotopic prostate cancer model on mice, whose GRPR expression has been confirmed. The fluorescent signal measured in the examined organs and blood highlighted the renal excretion and a quite rapid blood clearance of the dye (half-life time of 0.9 h and 1.8 h for healthy and diseased mice, respectively). An accumulation of the targeting probe was found 24 h p.i. in the prostate carcinoma (with respect to the healthy gland) and in the surrounding pelvic organs, probably invaded by the tumor cells. The comparison between targeted and untargeted probes 24 h p.i. confirmed a statistically significant difference in the tumor fluorescence signal, though the passive accumulation of the untargeted dye in the tumor tissue was appreciable. This observation is in line with recent literature reports that demonstrate the ability of cyanine dyes to accumulate into the necrotic core of tumors (**50**), with similar grade of internal necrosis reported for PC3 model (**51,52**). Moreover, the simulation of an IGS procedure performed on the orthotopic mouse model is a further demonstration of the potential effectiveness of BBN-Cy5.5 in the intraoperative theatre. As matter of fact, it was possible to identify the tumor boundary and even small malignant foci, that could be potentially associate with recurrence (**53,54**).

This is the first study, to the best of our knowledge, where a peptidic NIRF dye was specifically designed for supporting surgical treatment in prostate cancer. The probe, BBN-Cy5.5 is formed by a water soluble Cy5.5 dye conjugated to a peptidic vector able to specifically recognize GRPRs, overexpressed in the malignant tumor cells in comparison with normal prostate tissue. Our study paves the way for the application of novel targeted optical probes for the prostate cancer visualization during the surgery.

References

1. Siegel R. L.; Miller, K. D.; Jemal, A., Cancer Statistics, 2017. *CA Cancer J Clin* 2017, *67* (1), 7-30.

2. Litwin, M. S.; Tan, H. J., The Diagnosis and Treatment of Prostate Cancer: A Review. *JAMA* 2017, *317* (24), 2532-2542.

3. Trewartha, D.; Carter, K., Advances in prostate cancer treatment. *Nat Rev Drug Discov* 2013, *12* (11), 823-4.

4. Mandel, P.; Steuber, T.; Graefen, M., Radical prostatectomy in oligometastatic prostate cancer. *Curr Opin Urol* 2017.

5. Stitzenberg, K. B.; Wong, Y. N.; Nielsen, M. E.; Egleston, B. L.; Uzzo, R. G., Trends in radical prostatectomy: centralization, robotics, and access to urologic cancer care. *Cancer* 2012, *118* (1), 54-62.

6. Patel, V. R.; Shah, K.; Palmer, K. J.; Thaly, R.; Coughlin, G., Robotic-assisted laparoscopic radical prostatectomy: a report of the current state. *Expert Rev Anticancer Ther* 2007, *7* (9), 1269-78.

7. Eastham, J. A.; Kuroiwa, K.; Ohori, M.; Serio, A. M.; Gorbonos, A.; Maru, N.; Vickers, A. J.; Slawin, K. M.; Wheeler, T. M.; Reuter, V. E.; Scardino, P. T., Prognostic significance of location of positive margins in radical prostatectomy specimens. *Urology* 2007, *70* (5), 965-9.

8. Swindle, P.; Eastham, J. A.; Ohori, M.; Kattan, M. W.; Wheeler, T.; Maru, N.; Slawin, K.; Scardino, P. T., Do margins matter? The prognostic significance of positive surgical margins in radical prostatectomy specimens. *J Urol* 2005, *174* (3), 903-7.

9. Park, Y. H.; Jeong, C. W.; Lee, S. E., A comprehensive review of neuroanatomy of the prostate. *Prostate Int* 2013, *1* (4), 139-45.

10. Kung, T. A.; Waljee, J. F.; Curtin, C. M.; Wei, J. T.; Montie, J. E.; Cederna, P. S., Interpositional Nerve Grafting of the Prostatic Plexus after Radical Prostatectomy. *Plast Reconstr Surg Glob Open* 2015, *3* (7), e452.

11. Amit, M.; Na'ara, S.; Gil, Z., Mechanisms of cancer dissemination along nerves. *Nat Rev Cancer* 2016, *16* (6), 399-408.

12. Keereweer, S.; Kerrebijn, J. D.; van Driel, P. B.; Xie, B.; Kaijzel, E. L.; Snoeks, T. J.; Que, I.; Hutteman, M.; van der Vorst, J. R.; Mieog, J. S.; Vahrmeijer, A. L.; van de Velde, C. J.; Baatenburg de Jong, R. J.; Lowik, C. W., Optical image-guided surgery--where do we stand? *Mol Imaging Biol* 2011, *13* (2), 199-207.

13. Ntziachristos, V.; Yoo, J. S.; van Dam, G. M., Current concepts and future perspectives on surgical optical imaging in cancer. *J Biomed Opt* 2010, *15* (6), 066024.

14. Stummer, W.; Pichlmeier, U.; Meinel, T.; Wiestler, O. D.; Zanella, F.; Reulen, H. J.; Group, A. L.-

G. S., Fluorescence-guided surgery with 5-aminolevulinic acid for resection of malignant glioma: a randomised controlled multicentre phase III trial. *Lancet Oncol* 2006, *7* (5), 392-401.

15. van Dam, G. M.; Themelis, G.; Crane, L. M.; Harlaar, N. J.; Pleijhuis, R. G.; Kelder, W.; Sarantopoulos, A.; de Jong, J. S.; Arts, H. J.; van der Zee, A. G.; Bart, J.; Low, P. S.; Ntziachristos, V., Intraoperative tumor-specific fluorescence imaging in ovarian cancer by folate receptor-alpha targeting: first in-human results. *Nat Med* 2011, *17* (10), 1315-9.

16. Vahrmeijer, A. L.; Hutteman, M.; van der Vorst, J. R.; van de Velde, C. J.; Frangioni, J. V., Image-guided cancer surgery using near-infrared fluorescence. *Nat Rev Clin Oncol* 2013, *10* (9), 507-18.

17. Verbeek, F. P.; van der Vorst, J. R.; Tummers, Q. R.; Boonstra, M. C.; de Rooij, K. E.; Lowik, C. W.; Valentijn, A. R.; van de Velde, C. J.; Choi, H. S.; Frangioni, J. V.; Vahrmeijer, A. L., Near-infrared fluorescence imaging of both colorectal cancer and ureters using a low-dose integrin targeted probe. *Ann Surg Oncol* 2014, *21 Suppl 4*, S528-37.

18. Handgraaf, H. J. M.; Boonstra, M. C.; Prevoo, H.; Kuil, J.; Bordo, M. W.; Boogerd, L. S. F.; Sibinga Mulder, B. G.; Sier, C. F. M.; Vinkenburg-van Slooten, M. L.; Valentijn, A.; Burggraaf, J.; van de Velde, C. J. H.; Frangioni, J. V.; Vahrmeijer, A. L., Real-time near-infrared fluorescence imaging using cRGD-ZW800-1 for intraoperative visualization of multiple cancer types. *Oncotarget* 2017, *8* (13), 21054-21066.

19. Lee, J. Y. K.; Pierce, J. T.; Zeh, R.; Cho, S.; Salinas, R.; Nie, S.; Singhal, S., Intraoperative Near-Infrared Optical Contrast Can Localize Brain Metastases. *World Neurosurg* 2017.

20. Schaafsma, B. E.; Verbeek, F. P.; Elzevier, H. W.; Tummers, Q. R.; van der Vorst, J. R.; Frangioni, J. V.; van de Velde, C. J.; Pelger, R. C.; Vahrmeijer, A. L., Optimization of sentinel lymph node mapping in bladder cancer using near-infrared fluorescence imaging. *J Surg Oncol* 2014, *110* (7), 845-50.

21. Hachey, K. J.; Gilmore, D. M.; Armstrong, K. W.; Harris, S. E.; Hornick, J. L.; Colson, Y. L.; Wee, J. O., Safety and feasibility of near-infrared image-guided lymphatic mapping of regional lymph nodes in esophageal cancer. *J Thorac Cardiovasc Surg* 2016, *152* (2), 546-54.

22. Liu, J.; Huang, L.; Wang, N.; Chen, P., Indocyanine green detects sentinel lymph nodes in early breast cancer. *J Int Med Res* 2017, *45* (2), 514-524.

23. Tjalma, J. J.; Garcia-Allende, P. B.; Hartmans, E.; Terwisscha van Scheltinga, A. G.; Boersma-van Ek, W.; Glatz, J.; Koch, M.; van Herwaarden, Y. J.; Bisseling, T. M.; Nagtegaal, I. D.; Timmer-Bosscha, H.; Koornstra, J. J.; Karrenbeld, A.; Kleibeuker, J. H.; van Dam, G. M.; Ntziachristos, V.; Nagengast, W. B., Molecular Fluorescence Endoscopy Targeting Vascular Endothelial Growth Factor A for Improved Colorectal Polyp Detection. *J Nucl Med* 2016, *57* (3), 480-5.

24. Gong, L.; Ding, H.; Long, N. E.; Sullivan, B. J.; Martin, E. W., Jr.; Magliery, T. J.; Tweedle, M. F., A

3E8.scFv.Cys-IR800 Conjugate Targeting TAG-72 in an Orthotopic Colorectal Cancer Model. *Mol Imaging Biol* 2017.

25. van Driel, P. B.; Boonstra, M. C.; Prevoo, H. A.; van de Giessen, M.; Snoeks, T. J.; Tummers, Q. R.; Keereweer, S.; Cordfunke, R. A.; Fish, A.; van Eendenburg, J. D.; Lelieveldt, B. P.; Dijkstra, J.; van de Velde, C. J.; Kuppen, P. J.; Vahrmeijer, A. L.; Lowik, C. W.; Sier, C. F., EpCAM as multi-tumour target for near-infrared fluorescence guided surgery. *BMC Cancer* 2016, *16* (1), 884.

26. Christensen, A.; Juhl, K.; Persson, M.; Charabi, B. W.; Mortensen, J.; Kiss, K.; Lelkaitis, G.; Rubek, N.; von Buchwald, C.; Kjaer, A., uPAR-targeted optical near-infrared (NIR) fluorescence imaging and PET for image-guided surgery in head and neck cancer: proof-of-concept in orthotopic xenograft model. *Oncotarget* 2017, *8* (9), 15407-15419.

27. Yuan, J.; Yi, X.; Yan, F.; Wang, F.; Qin, W.; Wu, G.; Yang, X.; Shao, C.; Chung, L. W., Nearinfrared fluorescence imaging of prostate cancer using heptamethine carbocyanine dyes. *Mol Med Rep* 2015, *11* (2), 821-8.

28. Lutje, S.; Rijpkema, M.; Franssen, G. M.; Fracasso, G.; Helfrich, W.; Eek, A.; Oyen, W. J.; Colombatti, M.; Boerman, O. C., Dual-Modality Image-Guided Surgery of Prostate Cancer with a Radiolabeled Fluorescent Anti-PSMA Monoclonal Antibody. *J Nucl Med* 2014, *55* (6), 995-1001.

29. Sonn, G. A.; Behesnilian, A. S.; Jiang, Z. K.; Zettlitz, K. A.; Lepin, E. J.; Bentolila, L. A.; Knowles, S. M.; Lawrence, D.; Wu, A. M.; Reiter, R. E., Fluorescent Image-Guided Surgery with an Anti-Prostate Stem Cell Antigen (PSCA) Diabody Enables Targeted Resection of Mouse Prostate Cancer Xenografts in Real Time. *Clin Cancer Res* 2016, *22* (6), 1403-12.

30. Schroeder, R. P.; van Weerden, W. M.; Krenning, E. P.; Bangma, C. H.; Berndsen, S.; Grievink-de Ligt, C. H.; Groen, H. C.; Reneman, S.; de Blois, E.; Breeman, W. A.; de Jong, M., Gastrin-releasing peptide receptor-based targeting using bombesin analogues is superior to metabolism-based targeting using choline for in vivo imaging of human prostate cancer xenografts. *Eur J Nucl Med Mol Imaging* 2011, *38* (7), 1257-66.

31. Prignon, A.; Nataf, V.; Provost, C.; Cagnolini, A.; Montravers, F.; Gruaz-Guyon, A.; Lantry, L. E.; Talbot, J. N.; Nunn, A. D., (68)Ga-AMBA and (18)F-FDG for preclinical PET imaging of breast cancer: effect of tamoxifen treatment on tracer uptake by tumor. *Nucl Med Biol* 2015, *42* (2), 92-8.

32. Dam, J. H.; Olsen, B. B.; Baun, C.; Hoilund-Carlsen, P. F.; Thisgaard, H., In Vivo Evaluation of a Bombesin Analogue Labeled with Ga-68 and Co-55/57. *Mol Imaging Biol* 2016, *18* (3), 368-76.

33. Rybalov, M.; Ananias, H. J.; Hoving, H. D.; van der Poel, H. G.; Rosati, S.; de Jong, I. J., PSMA, EpCAM, VEGF and GRPR as imaging targets in locally recurrent prostate cancer after radiotherapy. *Int J Mol Sci* 2014, *15* (4), 6046-61.

34. Beer, M.; Montani, M.; Gerhardt, J.; Wild, P. J.; Hany, T. F.; Hermanns, T.; Muntener, M.; Kristiansen, G., Profiling gastrin-releasing peptide receptor in prostate tissues: clinical implications and molecular correlates. *Prostate* 2012, *72* (3), 318-25.

35. Lantry, L. E.; Cappelletti, E.; Maddalena, M. E.; Fox, J. S.; Feng, W.; Chen, J.; Thomas, R.; Eaton, S. M.; Bogdan, N. J.; Arunachalam, T.; Reubi, J. C.; Raju, N.; Metcalfe, E. C.; Lattuada, L.; Linder, K. E.; Swenson, R. E.; Tweedle, M. F.; Nunn, A. D., 177Lu-AMBA: Synthesis and characterization of a selective 177Lu-labeled GRP-R agonist for systemic radiotherapy of prostate cancer. *J Nucl Med* 2006, *47* (7), 1144-52.

36. Salinas, C. A.; Tsodikov, A.; Ishak-Howard, M.; Cooney, K. A., Prostate cancer in young men: an important clinical entity. *Nat Rev Urol* 2014, *11* (6), 317-23.

37. Laidler, P.; Dulinska, J.; Lekka, M.; Lekki, J., Expression of prostate specific membrane antigen in androgen-independent prostate cancer cell line PC-3. *Arch Biochem Biophys* 2005, *435* (1), 1-14.

38. Bouchelouche, K.; Choyke, P. L.; Capala, J., Prostate specific membrane antigen- a target for imaging and therapy with radionuclides. *Discov Med* 2010, *9* (44), 55-61.

39. Hermann, R. M.; Djannatian, M.; Czech, N.; Nitsche, M., Prostate-Specific Membrane Antigen PET/CT: False-Positive Results due to Sarcoidosis? *Case Rep Oncol* 2016, *9* (2), 457-463.

40. Sasikumar, A.; Joy, A.; Nanabala, R.; Pillai, M. R.; T, A. H., 68Ga-PSMA PET/CT False-Positive Tracer Uptake in Paget Disease. *Clin Nucl Med* 2016, *41* (10), e454-5.

41. Levine, L.; Lucci, J. A., 3rd; Pazdrak, B.; Cheng, J. Z.; Guo, Y. S.; Townsend, C. M., Jr.; Hellmich, M. R., Bombesin stimulates nuclear factor kappa B activation and expression of proangiogenic factors in prostate cancer cells. *Cancer Res* 2003, *63* (13), 3495-502.

42. Nagasaki, S.; Nakamura, Y.; Maekawa, T.; Akahira, J.; Miki, Y.; Suzuki, T.; Ishidoya, S.; Arai, Y.; Sasano, H., Immunohistochemical analysis of gastrin-releasing peptide receptor (GRPR) and possible regulation by estrogen receptor betacx in human prostate carcinoma. *Neoplasma* 2012, *59* (2), 224-32.

43. Markwalder, R.; Reubi, J. C., Gastrin-releasing peptide receptors in the human prostate: relation to neoplastic transformation. *Cancer Res* 1999, *59* (5), 1152-9.

44. Lee, S.; Xie, J.; Chen, X., Peptide-based probes for targeted molecular imaging. *Biochemistry* 2010, *49* (7), 1364-76.

45. Katsuno, T.; Pradhan, T. K.; Ryan, R. R.; Mantey, S. A.; Hou, W.; Donohue, P. J.; Akeson, M. A.; Spindel, E. R.; Battey, J. F.; Coy, D. H.; Jensen, R. T., Pharmacology and cell biology of the bombesin receptor subtype 4 (BB4-R). *Biochemistry* 1999, *38* (22), 7307-20.

46. Oliveira-Freitas, V. L.; Thomaz, L. D.; Simoneti, L. E.; Malfitano, C.; De Angelis, K.; Ulbrich, J. M.;

Schwartsmann, G.; Andrade, C. F., RC-3095, a selective gastrin-releasing peptide receptor antagonist, does not protect the lungs in an experimental model of lung ischemia-reperfusion injury. *Biomed Res Int* 2015, *2015*, 496378.

47. Ohki-Hamazaki, H.; Iwabuchi, M.; Maekawa, F., Development and function of bombesin-like peptides and their receptors. *Int J Dev Biol* 2005, *49* (2-3), 293-300.

48. Pu, F.; Qiao, J.; Xue, S.; Yang, H.; Patel, A.; Wei, L.; Hekmatyar, K.; Salarian, M.; Grossniklaus, H. E.; Liu, Z. R.; Yang, J. J., GRPR-targeted Protein Contrast Agents for Molecular Imaging of Receptor Expression in Cancers by MRI. *Sci Rep* 2015, *5*, 16214.

49. Slice, L. W.; Yee, H. F., Jr.; Walsh, J. H., Visualization of internalization and recycling of the gastrin releasing peptide receptor-green fluorescent protein chimera expressed in epithelial cells. *Receptors Channels* 1998, *6* (3), 201-12.

50. Xie, B.; Stammes, M. A.; van Driel, P. B.; Cruz, L. J.; Knol-Blankevoort, V. T.; Lowik, M. A.; Mezzanotte, L.; Que, I.; Chan, A.; van den Wijngaard, J. P.; Siebes, M.; Gottschalk, S.; Razansky, D.; Ntziachristos, V.; Keereweer, S.; Horobin, R. W.; Hoehn, M.; Kaijzel, E. L.; van Beek, E. R.; Snoeks, T. J.; Lowik, C. W., Necrosis avid near infrared fluorescent cyanines for imaging cell death and their use to monitor therapeutic efficacy in mouse tumor models. *Oncotarget* 2015, *6* (36), 39036-49.

51. Bastian, A.; Thorpe, J. E.; Disch, B. C.; Bailey-Downs, L. C.; Gangjee, A.; Devambatla, R. K.; Henthorn, J.; Humphries, K. M.; Vadvalkar, S. S.; Ihnat, M. A., A small molecule with anticancer and antimetastatic activities induces rapid mitochondrial-associated necrosis in breast cancer. *J Pharmacol Exp Ther* 2015, *353* (2), 392-404.

52. Jung, D. C.; Lee, H. J.; Seo, J. W.; Park, S. Y.; Lee, S. J.; Lee, J. H.; Kim, I. H., Diffusion-weighted imaging of a prostate cancer xenograft model seen on a 7 Tesla animal MR scanner: comparison of ADC values and pathologic findings. *Korean J Radiol* 2012, *13* (1), 82-9.

53. Sofer, M.; Hamilton-Nelson, K. L.; Civantos, F.; Soloway, M. S., Positive surgical margins after radical retropubic prostatectomy: the influence of site and number on progression. *J Urol* 2002, *167* (6), 2453-6.

54. Eastham, J. A.; Kuroiwa, K.; Ohori, M.; Serio, A. M.; Gorbonos, A.; Maru, N.; Vickers, A. J.; Slawin, K. M.; Wheeler, T. M.; Reuter, V. E.; Scardino, P. T., Prognostic significance of location of positive margins in radical prostatectomy specimens. *Urology* 2007, *70* (5), 965-9.

Chapter 4

Concluding Remarks

The development of new diagnostic tools able to actively detect different pathological conditions is nowadays a crucial need. Considering the population aging, some diseases are becoming rooted in the society and, too often, they are diagnosed in a late stage. Following the steps of the wise Hippocrates, who *ca.* 2500 years ago proposed the famous sentences "Prevention is better than cure", during my PhD project I mainly focused on the development of novel imaging probes for early diagnosis of diffuse disorders.

In **Paragraph 2.1** a Gd(III)-based paramagnetic micellar nanosystem, decorated with anti-VCAM1 peptide, was designed for MRI detection of inflammation. The system was demonstrated to be highly stable and biocompatible, due to the PEG molecules that surround the hydrophobic core. These characteristics, besides the high relaxivity, make it a valid candidate for the *in vivo* test on inflammation models. The NMRD analysis has shown, as expected for this type of aggregates, a relaxivity hump at around 30 MHz. This finding pushed to test the system on 1 T (42.5 MHz) MRI scanner, to exploit its maximum relaxometric performance. The *in vivo* results confirmed the MRI visualization of the LPS-induced inflammation, with a quite good signal enhancement (*ca.* 40%) in the diseased region with respect to the contralateral healthy tissue. Furthermore, the specificity of the micelles was demonstrated comparing them with similar micelles decorated with an untargeted scrambled peptide. Afterwards, as described in **Paragraph 2.2**, the micelles were tested on a model of acute neuroinflammation. As mentioned in this paragraph, quite often neuroinflammation acts as an alarm bell that anticipates/carries a neurodegenerative disease. For this reason, the VCAM-1 targeted system was properly designed for the early detection of neuroinflammation. In literature, some VCAM-1 targeted particles bearing negative MRI contrast were reported, bringing to possible not univocal identification of this condition. Positive contrast could precisely localize the neuroinflammation in the brain and, considering the quite long blood half-life of the micelles, the system is more available to complete its task. To assess the active targeting, micelles were firstly tested on brain endothelial cells (Bend3), with TNF-α induced expression of the VCAM-1 receptors. Evaluation of the Gd(III) internalized into the cells and acquired T_{1w} images, confirmed a specific accumulation of the micelles in VCAM-1 expressing cells. Moreover, the contrast enhancement is locally visible *in vivo* in the inflamed brain region: 24h p.i. the inflamed striatum showed *ca.* 40 % of T_1 signal enhancement with respect to the contralateral healthy tissue. Furthermore, promising differences were observed comparing the targeting system with the scrambled control and the clinically approved Gd-agent Multihance (Bracco). Even if the destiny of the system inside the brain was not completely clarified, the *ex vivo* staining suggested a possible extravasation of the micelles

after monocytes/macrophages ingestion. The herein proposed paramagnetic micelles were demonstrated to be high efficient MRI system for the early detection of neuroinflammation.

Paragraph 3.1 reports an alternative method to design efficient MRI probes, exploiting Gd(III) tetranuclear probes based on Gd-AAZTA. The relaxivity of these probes were 2.4-fold higher than the monomeric parent, thus confirming the good potential of this agent. The novel synthesized molecule, that could bear different functional groups, represents a versatile platform for bioconjugation. As previously discussed, the synthesis of these novel ligands brought, among others, to the maleimide – activated moiety, which was used for the bioconjugation with the targeting peptide, as discussed in **Paragraph 3.2.** Herein, the tetrameric Gd-AAZTA-based moiety was conjugated to the small CREKA peptide for targeting the reactive extracellular matrix surrounding the tumor. In particular, the fibrin-fibronectin complex was demonstrated to be a valid and specific marker for prostate cancer. CREKA-dL-$(Gd^{-}AAZTA)_4$ complex showed a relaxivity 70% higher than similar tetrameric probes based on Gd-DOTA, and was tested on orthotopic model of prostate cancer. The promising results have shown the quick active accumulation in the tumor, suggesting an effect of “delayed diffusion” induced by the targeting peptide. The promising results have also demonstrated a clear difference between the tumor and the healthy tissue, supporting the good potential of this probe for the specific MRI visualization of the disease.

Following the diagnosis of the malignancy, it is necessary to eradicate it from the body. The surgery, during the years, was affirmed as leading treatment for localized prostate tumor. Even if the radical prostatectomy is widely diffuse for this type of disease, precisely localize the tumor in the gland could represent a huge improvement in the field. In **Paragraph 3.3**, a NIRF optical dye called BBN-Cy5.5 is proposed as molecule for specific imaging guided surgery of prostate tumors. The probe could prospectively limit the quantity of healthy exported tissue during the operation theatre and, consequently, reduce the side effects. The probe, which emits in the near-infrared and has a high water solubility, was characterized and preliminarily tested on prostate cancer cell line. The study confirmed an active interaction, induced by the peptide, with the tumor cell line. Afterwards, the optical imaging-based biodistribution of the molecule indicated a principal renal excretion pathway and a specific tumor accumulation 24 h p.i. At the same time point, a significant difference with respect to both the control (Sulfo Cy5.5(COOH)) dye and the healthy prostatic tissue was evaluated. Furthermore, during the simulation of the operation theatre, it was confirmed the ability of the probe to discriminate between the tumor cells and the surrounding healthy tissue. This probe represents, on our knowledge, the first Image-Guided Surgery application of peptide-based molecule in prostate cancer. The results obtained paves the way for the development of a new

category of molecules for the surgical treatment of prostate cancer, aimed at limiting the side effect induced by radical prostatectomy, and allowing the active removal of positive surgical margins that are often associated with tumor recurrence.

Acknowledgements

Col passare degli anni, così come molte altre cose, anche I ringraziamenti tendono ad allungarsi. Per un'esperienza così corposa come quella di un dottorato è anche logico che i ringraziamenti tendono a diventare piuttosto sostanziosi. Considerando, inoltre, che questa sarà la parte della mia tesi di dottorato che verrà (in assoluto) letta da più gente, mi sento una certa responsabilità nello scrivere dei ringraziamenti degni. Cercherò di fare del mio meglio.

Quando ripenso al mio dottorato, oltre ad una buona dose di sfinimento mentale e fisico, mi vengono in mente un numero incredibilmente alto di persone. Grazie al loro sostegno, alle loro idee o semplicemente grazie alla loro presenza è stato possibile rendere il mio dottorato un'esperienza decisamente positiva. Purtroppo non potrò citare tutti coloro che ho in mente altrimenti dovrei scrivere un'altra tesi di ringraziamenti. Cercherò di focalizzarmi.

Comincierò dalle persone che hanno dato il via all'esperienza, ovvero **Enzo** ed il **Prof.Aime**.

Enzo è stato una guida di una disponibilità infinita. Grazie a lui ho imparato quello che, a posteriori, riconosco essere il vero spirito del dottorato: l'imparare a crescere dai propri errori. Enzo, sin dall'inizio, ha dato sempre appoggio alle mie iniziative, permettendomi di confrontarmi con esse (nel bene e nel male). Penso sinceramente che Enzo sia stata la guida giusta per me.

Il prof. Aime sarà sicuramente tra i più citati nei ringraziamenti delle tesi (e non solo) a tutti I livelli. Non faccio fatica a crederlo: difficilmente si incontrano delle persone del genere nella vita. E' oggettivamente una persona con una visione prospettica incredibile, di un'intelligenza finissima e, cosa per me più importante, di una positività e stabilità realmente rara. Sempre più propenso alla soluzione che al problema, la sua carriera di successo rispecchia bene la sua persona. Sono veramente stato fortunato a poter affrontare il dottorato sotto la sua ala.

Tra le persone che mi hanno permesso di cominciare l'avventura ci sono anche due colleghe che, ben presto, si sono trasformate in care amiche: **Rachele** e **OHO Francesca Garello**.

Buona parte di quello che ho imparato in laboratorio lo devo a loro due. Rachele, eclettica ed inarrestabile, mi ha introdotto nel magico mondo della sintesi chimica e, grazie a lei, praticamente ogni giorno è stato sempre un'avvenimento degno di nota. Tra le solubilità impossibili e le esplosioni controllate all'HPLC, la noia non è mai stata di casa.

Francesca Garello. Chi mi conosce sa che questo è un nome che mi piace ripetere molto spesso, quasi come un mantra. Le motivazioni le rivelerò in anteprima mondiale e sono fondamentalmente due: il primo è che ogni volta che lo ripeto rifletto la stima infinita che ho per lei. Il secondo motivo,

non meno importante, è che così non me lo dimentico. In realtà, sebbene molta gente (compresa lei stessa) sostenga che su Francesca aleggi un alone di malasorte, io penso, al contrario, che porti molta fortuna. Un mantra positivo. Sarà perchè si destreggia agilemente tra le più svariate problematiche, tirando fuori sempre una soluzione. Sarà perchè affronta propositiva e con passione ogni sfida che le si propone. Io la reputo la mia saggia consigliera, e non potrei essere più felice di averla avuta come tale.

Viaggiando ad un'altra latitudine passo a ringraziare **Paola** e **Francesca Arena**. Di una gentilezza e disponibilità incessante, senza di loro non avrei potuto concludere buona parte della mia tesi. Sono la mano ferma che non ho (e non avrò mai), dispensatrici di consigli di cui ho fatto tesoro negli anni.

Le ultime arrivate, ma non meno importanti, sono **Martina T.** e **Giada**. Martina riesce a sintetizzare qualunque cosa, per me è la Walter White de Roma. E come dimenticare le vittoriose giornate sintetiche passate con Giada, succedute da analisi incessanti di immagini all'IVIS di Ivrea. Lavorando con loro è stato come essere Shiva, facilitato da due braccia aggiuntive (molto più efficienti delle mie, tralaltro).

A special mention goes to Prof. Lowik and Laura Mezzanotte, which gave me the possibility to spend an incredible period, from the human to the scientific point of view, in the Netherland. Un caloroso ringraziamento va anche a Giorgia, Natasa, Laura e Rocio, Alexandra che mi hanno fatto sentire a Rotterdam come a casa.

Non posso certo dimenticare tutti I compagni di laboratorio con cui ho condiviso questi anni. Cominicierò con le più noiose, ovvero **Mary** ed **Annasofia**. Loro sono più che colleghe per me, sono anche più che amiche, praticamente sono allo stesso livello astrale di San Catello. Le ho sempre considerate come delle sorelle e quindi le ho sempre trattate come tali. Cionostante loro non sembrano avere gradito, bullizzandomi continuamente.

La mia compagna di dottorato (sbl)**Eleonora,** con la quale, dal primo viaggio sul pullman per Tubingen, (da veri clandestini) c'è stata subito complicità.

Ivan, **Diego**, **Giuseppe, Federico, Sergio,** (ebbene sì, non ci sono solo donne nel nostro gruppo), **Enza**, **Valeria B., Deyssy, Martina B., Carla** ed ancora **Eliana**, **Simonetta, Alessandra, Chiara B., Alessia, Mauro, Daniela, Valeria, Giuseppe, Francesca R.**

I compagni del caffè, nonché amici antichi: **Marnetto, Jean e Ruiu**. Aiutate a digerire, come l'effervescente Brioschi.

Dulcis in fundo la mia famiglia.. **Mamma**, **Papà** e **Fabiana:** sin da quando sono piccolo mi avete appoggiato nelle mie passioni, accompagnandomi, con delicatezza, fino a questo traguardo. Grazie per stare sempre al mio fianco.

Infine **Lorena**… non potevo avere compagna migliore in questi anni. Sempre a supportarmi (Mary direbbe sopportarmi, anche se faccio fatica a capirne il motivo) in tutto e per tutto, ad aiutarmi e sostenermi. Consigliera fidata ed amica, affrontare con te al fianco tutto il percorso mi ha solo confermato che le scelte che ho fatto non potevano essere le più giuste.

Chi mi conosce sa che io adoro lo sport di squadra e che quando la squadra "gira" il gioco diventa divertimento. Questa è stata una squadra veramente fantastica. GRAZIE!

List of pubblications

Full papers

1. **Pagoto A.**, Stefania R., Garello F., Arena F., Digilio G., Aime S., Terreno E. *Paramagnetic Phospholipid-Based Micelles Targeting VCAM-1 Receptors for MRI Visualization of Inflammation*, Bioconjugate Chemistry – 2016

2. Garello F., **Pagoto A.**, Arena F., Buffo A., Blasi F., Alberti D, Terreno E. *MRI visualization of neuroinflammation using VCAM-1 targeted paramagnetic micelles,* Nanomedicine: NMB – 2017

3. Tripepi M., Capuana F., Gianolio E., Kock F.V., **Pagoto A.**, Stefania R., Digilio G., Aime S. *Synthesis of high relaxivity gadolinium AAZTA tetramers as building blocks for bioconjugation*, Bioconjugate Chemistry – 2018

4. **Pagoto A.**, Stefania R., Tripepi M., Lanzardo S., Longo D., Porpiglia F., Manfredi M., Aime S., Terreno E. *Highly efficient MRI agent to target fibrin/fibronectin complex in Prostate Adenocarcinoma*, In Preparation

5. **Pagoto A.**, Marini G., Tripepi M., Garello F., Stefania R., Bardini P, Arena F, Lanzardo S. Valbusa G., Aime S., Terreno E. *NIRF-guided surgery of Prostate Cancer targeting Gastrin-Releasing Peptide Receptor,* In Preparation

6. Cohen G., Hadas R., Stefania R., **Pagoto A.** , Ben-Dor S. ,Longo D. , Elbaz M. , Gershon E. , Aime S., Neeman M., *Visualization of tissue transglutaminase and factor XIII activities during embryo implantation and their impact on decidual blood vessel's function*, In preparation

Abstract Submission

1. European Molecular Imaging Meeting (20-23 March 2018, San Sebastian, Spain)

Title: "NIRF-guided surgery of Prostate Adenocarcinoma targeting Gastrin-Releasing Peptide Receptor"

2. CancerTO (7-9 March 2018, Torino, Italy)

Title:" Peptide-based MRI imaging agent for fibrin/fibronectin targeting of Prostate Cancer"

3. CancerTO (7-9 March 2018, Torino, Italy)

Title:" Novel Gastrin-Releasing Peptide Receptor targeted NIRF dye for image-guided surgery of Prostate Cancer "

4. World Molecular Imaging Congress (13-16 September 2017, Philadephia, USA)

Title:" Peptide-based MRI imaging agent for extracellular targeting of Prostate Cancer"

5. World Molecular Imaging Congress (13-16 September 2017, Philadephia, USA)

Title:" NIRF-guided surgery of Prostate Adenocarcinoma targeting Gastrin-Releasing Peptide Receptor"

6. European Molecular Imaging Meeting (5-7 April 2017, Cologne, Germany),

Title: “Highly efficient MRI agent to target fibrin-fibronectin complex in Prostate Adenocarcinoma“

7. School for Advanced Imaging in Biological Research (14-15 March 2017, Weizmann, Israel)

Title “Bio-active substrate analogs for visualization of transglutaminase isoenzymes activities during embryo implantation in mice “

8. European Molecular Imaging Meeting (8-10 March 2016, Utrecht, The Netherlands)

Title: “MRI visualization of neuroinflammation using VCAM-1 targeted paramagnetic micelles “

9. Imaging Meeting (EMIM) congress (8-10 March 2016, Utrecht, Netherlands)

Title:“Fibrin/Fibronectin complex as extracellular imaging biomarker of Prostate Adenocarcinoma“

10. International Society for Magnetic Resonance In Medicine (30 May-5 June 2015, Toronto, Canada)

Title:“Paramagnetic micelles targeting VCAM-1 receptors for imaging inflamed endothelium by MRI“

11. European Molecular Imaging Meeting (EMIM) (17-20 March 2015, Tubingen, Germany),

Title: “MRI detectable micelles targeting VCAM-1 receptors for imaging inflamed endothelium “

12. XLIII National Congress of Magnetic Resonance (22-24 September 2014, Bari, Italy), wit

Title: “Lipid-based nanosystems targeting the activated endothelium for the in vivo visualization by MRI of localized inflammation”